BIOINSPIRED DESIGN AND FABRICATION OF SUSTAINABLE CONSTRUCTION MATERIALS WITH ENHANCED MECHANICAL PERFORMANCE AND SELF-HEALING PROPERTIES

by

Vanessa Restrepo Perez

A Dissertation

Submitted to the Faculty of Purdue University

In Partial Fulfillment of the Requirements for the degree of

Doctor of Philosophy

School of Mechanical Engineering

West Lafayette, Indiana

August 2021

THE PURDUE UNIVERSITY GRADUATE SCHOOL
STATEMENT OF COMMITTEE APPROVAL

Dr. Eckhard A. Groll, Co-Chair
School of Mechanical Engineering

Dr. Ramses V. Martinez, Co-Chair
School of Industrial Engineering

Dr. Andres Arrieta
School of Mechanical Engineering

Dr. Adrian Buganza Tepole
School of Mechanical Engineering

Dr. Davide Ziviani
School of Mechanical Engineering

Approved by:
Dr. Eckhard A. Groll

Para mi madre, mi gran inspiración y mayor motivación

ACKNOWLEDGMENTS

I would like to express my sincere gratitude to my supervisors Dr. Eckhard A. Groll and Dr. Ramses V. Martinez for their unwavering support, invaluable advice, and belief in me. Their immense knowledge and plentiful experience have encouraged me in all the time of my academic research and daily life. I would also like to thank the members of the committee Dr. Andres Arrieta, Dr. Adrian Buganza Tepole, and Dr. Davide Ziviani for providing valuable comments and help during the development of this work. My gratitude extends also to Dr. Mirian Velay Lizancos for providing treasured support which was really influential in shaping my experiment methods. My appreciation also goes out to my family and friends, without their tremendous understanding and encouragement, this would have not been possible.

TABLE OF CONTENTS

LIST OF TABLES

LIST OF FIGURES

LIST OF ABBREVIATIONS

CZM	Cohesive Zone Model
DCB	Double Cantilever Beam
DPZ	Detachment Process Zone
FE	Finite Element
PBC	Periodic Boundary Conditions
PP	Polypropylene
PPR	Potential-Based Cohesive Model
RHLE	Representative Hook-and-Loop Element
SECMAS	Self-Healing Elastomeric/Cementitious/Mechanical Adhesive Structures
SEM	Scanning Electron Microscope

ABSTRACT

The design and fabrication of easy-to-assemble structural materials with enhanced mechanical performance and the capability to self-repair autonomously will pave the way toward future sustainable constructions. The development of hybrid structures—material composites comprising two or more materials with synergistic and complementary properties—will enlarge the range of mechanical properties accessible by conventional homogeneous materials. Unfortunately, the cohesion bonds among the components of hybrid structures often impede the removal and re-addition of components, limiting the simple reconfiguration of hybrid structures into different designs. Hook-and-loop fasteners, on the other hand, provides a strong and reversible connection based on mechanical interlocking that allows the attachment and detachment of two surfaces expanding their use in engineering applications.

The effective mechanical response of the hook-and-loop fasteners strongly depends on the ability of the hooks to engage with the loops at the sub-millimeter level. New computational models will help in the design and manufacturing of hook-and-loop fastening products by providing a quick turnaround time with minimal prototyping and testing. The development of such computational models will enable the analysis of these fasteners at both micro- and macro-scales. The two-scale model strategy have demonstrated to predict the mechanical behavior of hook-and-loop fastener and, as a design predictive tool, capture the main deformation and dissipative mechanisms at the relevant length scales.

This Ph.D. dissertation focuses on the bioinspired design and fabrication of structural materials with enhanced mechanical performance and the capability to self-repair autonomously. The resulting scalable and modular structural materials are easy-to-assemble and easy-to-disassemble at room temperature, serving as an attractive strategy for the development of resilient, deployable, convertible, and temporary constructions capable to meet the rapidly increasing modern demands.

1 INTRODUCTION

1.1 Motivation

Nature, through years of evolution, has developed intricate multiscale structures and materials that overcome severe limitations commonly faced by human-made systems. Improvements to artificial systems are often bounded by the difficulty of simultaneously enhance two mutually exclusive mechanical properties, such as strength and toughness. These difficulties are often addressed by natural systems through their architectural microstructure, which allows them to display remarkable mechanical performance under extreme conditions.[1,2] By looking and learning how and why biological materials attain these advantageous mechanical functionalities, we can pave the way to the design and creation of new bioinspired synthetic materials that display unique and attractive combinations of mechanical properties. These new materials and structures would be able to remain functional under extreme conditions (loading, size, temperature, pressure, etc.) and could be employed to improve a wide range of fields, such as medicine, transportation, and construction.

The expansion of modern construction technologies demands materials with improved structural performance and the capability to be easily reconfigured into a variety of structural designs.[3,4] This need has led to the development of a variety of hybrid structures that enlarge the range of mechanical properties accessible by conventional homogeneous materials.[5–8] The fabrication of hybrid structures has often benefited from the notion of mimicking the design and composition of structures occurring in nature.[9–11] This bioinspired design approach has produced hybrid structures with unique combinations of stiffness,[12] strength,[13,14] and toughness[7,15–17] through the judicious arrangement of hard and soft materials. Unfortunately, heuristic and bioinspired approaches to design hybrid structures often fail to adequately replicate the complex hierarchical architecture that imbues natural composites with enhanced mechanical properties.[18] Additionally, the cohesion bonds among the components of hybrid structures often impede the removal and re-addition of components, limiting the simple reconfiguration of hybrid structures into different designs.[19–21]

1.2 Structure of the Dissertation

The following document is organized in five main parts: Chapter 1 introduces the idea of using bioinspired designs towards the fabrication of construction material with enhanced mechanical properties. This chapter also reviews in detail current state-of-the-art of the different nature-inspired approaches relevant to my graduate research. Chapter 2 propose a two-scale computational model for hook-and-loop fasteners based on a real geometry and material properties. This chapter aims to develop a predictive two-scale finite element model (i.e., both at the micro- and macro-scales) that capture the mechanical behavior of the hook-and-loop fastener. Chapters 3 and 4 describe the experimental methods, analytical formulation, and the results obtained during the manufacturing of bioinspired structural systems inspired by nacre. Finally, Chapter 5 summarizes the conclusions and provides details of the future work developed in this dissertation.

1.3 Background and Literature Review

1.3.1 Hook-like Connections in Nature

Natural organisms have design features that grant them ability to adhere to surfaces for locomotion such as geckos, lizards, and spiders.[22] Geckos, for example, have the exceptional ability to climb vertical surfaces due to the presence of a hundred thousand keratinous hairs or setae.[23] Similarly, the ventral segments of the spiders' legs are covered by microtrichia with spatula-like tips that increase friction considerably friction when climbing steep surfaces.[24] Although the presence of hook-like surface in the structure of some species can facilitate movements in high steep surfaces by enhancing adhesion and friction, other species such as *Stylasterias forreri* (also called "Velcro" sea stars) and *Azteca Andreae* ants[25] are well-known to use hook-like teeth and hook-shaped claws to capture prey.

Birds feather structures are another example in nature with hook-like connections. The architecture of the feather contains barbs branching out from the main shaft. These barbs also contain small barbules with microhooks that facilitate the connection between barbs. This type of connection provides a self-repair mechanism through the re-attachment of un-hooked junctions.[26] Hui et al.[27] studied the crack trapping effect enabled by the architecture of the base plate of *Balanus amphitrite* which allows them to attach strongly to submerged surfaces in tidal waters. Recently,

Morano et al.[28] used computational modeling and additive manufacturing to explain the mechanisms that contribute to such strong adhesion.

1.3.2 Hook-like Connections in Engineering

The first mechanical adhesives, based on hook-and-loop fasteners, were bio-inspired by the burrs of burdocks.[29] Burdocks are small plants covered by several spines with hook-like shaped ends. When the burrs come in contact with fibrous surfaces (such as cloths or hair), they are hard to remove. This observation resulted in the development of hook-and-loop fasteners. Hook-and-loop fasteners consist of two components: i) hooks tape and ii) loops with fibrous surfaces. Once contact occurs (i.e., by pressing two tape surfaces together), loops in the fibrous surface engage and entangled with the hooks providing a strong connection based on mechanical interlocking. Separation can be attained by either pulling-out or peeling-off the two surfaces.[30]

Mechanical fasteners have been widely employed in engineering applications and in medicine. For instance, Restrepo and Martinez[31] developed a reconfigurable elastomeric cementitious structure—comprised of cementitious bricks joined by hook and loop mechanical adhesive interfaces and organized in nacre inspired brick and mortar structures—with the capability to concentrate the formation and propagation of cracks along the mechanical adhesive interfaces, which efficiently distribute loading forces and accommodate deformation. Similarly, Hebeler et al.[32] proposed and interface between geomembrane and geotextile containing hook-and-loops fasteners to improve the connection and increase shear strength. On the other hand, Meislin[33] demonstrated how surgical muscle repair can be accomplished by connecting separated tendons and muscles using hook-and-loops fasteners. Although these examples illustrate the benefits of using hook-and-loop fasteners and the demands for such fasteners keeps increasing with new applications, there are not many computational models and tools that can be employed to study and understand their mechanical behavior.[34–37] The development of such computational models would enable the prediction of the analysis of these fasteners and help shorten the design and production process. Such models will assist designers in making decisions and provide a virtual test bed to evaluate the performance of a new fastener.

1.3.3 Multi-scale Computational Models

Previous works have demonstrated the ability of multiscale homogenization technique as an effective way to predict the behavior of the large homogenized systems by considering the details and heterogeneities at lower scales. Nguyen et al.[38] successfully predicted the macroscopic failure behavior of the concrete by considering micro-scale details using a multistep model. In these models, the time-dependent mechanical properties of the cement paste as a purely brittle material is considered at the microscale. Following a continuous-discontinuous multiscale method, using cohesive models, they then predict the quasi-brittle mechanical properties of concrete at the macroscale. Using this approach, the first scale considered the mesoscale geometry of the mortar, (e.g., Cement paste with fine aggregates) and the second scale consisted of the homogenized mortar (obtained from the mesoscale simulations) and coarse aggregates. Cracks were allowed to initiate, propagate, and interact on the cement paste fine/coarse aggregates, mortar and in their respective interfaces [39]. In general, these multiscale approaches allows us to couple both micro and macro scales and predict the homogenized behavior of the macroscale model even when fracture leads to localizations making the homogenization process more difficult in these cases [40–42].

1.3.4 Hybrid Structures

Construction hybrid structures comprising brittle elements, such as most cementitious composites, are susceptible to microcracking after enduring multiple stress loading and thermal expansion cycles.[43] The coalescence of these microcracks results in larger damages that rapidly degrade the structural performance of the composite.[44] Several approaches, inspired by self-healing natural materials such as bone or insect cuticle, have been developed to enlarge the service life of cementitious composites by conferring them with the ability to self-repair small cracks before the damage causes catastrophic failure.[45] The addition of mineral admixtures,[19,46–48] polymeric additives,[49,50] and expansive chemical compounds[51,52] as healing agents in cementitious composites served to demonstrate the autonomic healing of microcracks in these composites. Unfortunately, adding healing agents into the cementitious matrix without appropriate encapsulation causes their immediate reaction, reducing the efficiency of the self-healing when a crack originates and introducing undesirable side-effects on the mechanical properties of the composite.[53]

The addition of unprotected expansive chemical compounds into the cementitious composites leads to uncontrolled reactions with water across the cementitious matrix, which trigger the expansion the compounds not only on the cracked zone, but inside the matrix, originating more cracks.[54] To improve this limited self-healing performance, the incorporation of microcapsules and hollow fibers filled with healing agents into cementitious composites have been explored to ensure the activation of the self-healing behavior of the composite only at the location and time the crack forms.[45,55] Following this strategy, polyvinyl alcohol (PVA) has been used to coat powder mineral pellets and expansive agent granules, demonstrating crack self-healing on several cement-based materials after rainwater dissolves the PVA coating and releases the self-healing agents across the crack.[56] Unfortunately, for the self-healing to be successful, the location of the microcracks need to coincide with the random positioning of the discrete domains of healing agents dispersed inside the cementitious matrix.[57] Harnessing bacterial activity to fill up cement cracks with calcium carbonate has been explored by embedding bacterial spores into concrete composites. [58] While this approach demonstrated the complete sealing of 700 μm wide cracks, spore viability inside the composite was significantly reduced after 30 days due to the high pH (pH > 11) and low moisture inside the cementitious matrix.[59]

1.3.5 Transformable Structures for Sustainable Construction

While traditional construction technologies often conceive built structures as permanent, modern techniques aim to minimize waste by designing structures that can be disassembled and reconfigured to meet new requirements.[3] Additionally, structures designed and fabricated for their future disassembly and reconfiguration offer the possibility to easily exchange damage components for new ones, enlarging their service life. Unfortunately, disassembly processes are often labor-intensive, require qualified personnel, and have greater costs than demolition and disposal.[60] The design of new hybrid structures that can be easily disassembled and reconfigured in order to exchange broken components or meeting new structural demands would be desirable to improve sustainable construction and development.

1.3.6 Nacre-inspired Self-healing Composites

Natural self-healing composites are fabricated using a bottom-up approach using scalable arrangements of soft and stiff materials that propagate the self-healing behavior across scales. For example, nacre can be described as a multilayered brick-and-mortar structure comprising stiff nanometer-thick aragonite platelets (bricks) bonded by soft and elastic biopolymers (mortar).[61] This brick-and-mortar structure inhibits transverse crack propagation through nacre and provides this natural material with enhanced strength and toughness,[1,10] since the sacrificial bonds generated between the biopolymers and the aragonite platelets efficiently dissipate energy from external loads.[62] Additionally, after fracture, the elastic biopolymers can regenerate their sacrificial bonds with the aragonite platelets in presence of moisture, imparting self-healing properties to nacre.[63]

Large-scale bio-inspired materials mimicking nacre's brick-and-mortar structure have been developed by combining thin plates of alumina bonded with a stretchable polymeric mixture (PVA and polymethyl methacrylate, PMMA).[64] These multilayered hybrid structures exhibited a toughness one order of magnitude higher than bulk alumina due to the efficient energy dissipation at their interlocking soft/hard interfaces. Similarly, hybrid structures fabricated using hard interlocking components, such as ABS or cement bricks, and soft highly deformable adhesives, such as epoxy or silicone rubber, exhibited enhanced toughness and resistance to transverse forces.[20,65] Recently, structural brick-and-mortar composites comprising micrometer-thick glass bricks joined by thin layers of a supramolecular polymer (poly-borosiloxane, PBS) demonstrated that composites with a nacre-inspired microstructure can repeatedly achieve complete self-healing at room temperature.[19] Unfortunately, brick-and-mortar composites using supramolecular polymers as sacrificial bonds require several hours to complete the self-healing, impeding the avoidance of catastrophic failure of structures exposed to loads switching directions at moderate frequencies. Using stronger elastic bonding materials can improve the load-bearing capability of brick-and-mortar composites; however, triggering the self-healing behavior of these soft interfaces often requires the external application of heat,[66] water,[67] or UV light.[68]

1.3.7 Nacre-Inspired Self-Healing Interfaces

Studies of the mechanism behind the toughness of nacre have shown that the adhesive that holds the tablets together (protein named Lustrin A)[69] forms a structure that is highly modular.[70,71]

These highly modular proteins consist of long molecules with entangled or “hidden length” domains that unravel sequentially upon the application of external loads.[70–72] The extra lengths for the proteins to unfold generates large extensibility enhancing the dissipation of energy. Previous studies have borrowed the concept of modular unfolding proteins to improve the performance of adhesive materials. As an example, nanometer-thick polyelectrolyte multilayers (PEMs) mimics the proteins in organic materials by breaking and reforming their electrostatic bonds, imparting partial self-healing properties to the PEMs, and substantially increasing the energy required to fail under shear loads.[73] Similarly, reversible unfolding modular cross-linker design has been proposed to increase the stiffness and tensile strength of a poly(n-butyl acrylate) networks without sacrificing its extensibility.[74]

2 A TWO-SCALE STRATEGY FOR THE MODELING OF HOOK-AND-LOOP FASTENERS

Motivation and rationale: Hook-and-loop-like joints have been widely used in many engineering applications and even observed in nature. The demand for computational models to predict the behavior of fasteners is increasing as they will be key for reducing the design process time and manufacturing costs. Here, we develop a bottom-up two-scale modeling strategy, which enables us to capture the mechanical performance of a hook-and-loop fastener at both micro- and macro-scales. In particular, we study a two-scale homogenization approach that first starts with a micromechanical model of a hook-and-loop fastener, through a so-called Representative Hook-and-Loop Element (RHLE) computational domain, that considers the detailed geometry of the individual building blocks of the hook-and-loop fastener and their statistical geometrical variability. The model is capable of capturing the mechanical behavior of the hook-and-loop fastener during the engaging and detachment processes. The computational results are then validated with tensile tests done to the hook-and-loop fasteners. The second scale considers the homogenization of the micromechanical model into a Detachment Process Zone (DPZ) which reveals an emerging length scale. The resulting effective traction-separation law concept is then employed at the macroscale in a Double Cantilever Beam (DCB) test using a macroscale model, which is then validated with our experiments. The results suggest that the two-scale model strategy is able to predict the mechanical behavior of hook-and-loop fastener and, as a design predictive tool, capture the main deformation and dissipative mechanisms at the relevant length scales.

2.1 Introduction

This chapter presents a two-scale computational model for hook-and-loop fasteners based on a real geometry and material properties. This study aims to develop a predictive two-scale finite element model (i.e., both at the micro- and macroscales) that enables us to capture the mechanical behavior of the hook-and-loop fastener. In the first part of this study, we provide details of the micromechanical models of both hooks and loops, including both geometry of hooks and fibrous loops and material properties. Following a two-step homogenization technique, the results from the micromechanical models are used as an input in the macromechanical model to predict the

performance of Double Cantilever Beam (DCB) under mode-I loading. For both micromechanical and macromechanical models, the results from the numerical simulations are validated with the experiments. The remainder of the chapter is organized as follows. Section 2.2 presents the geometrical and physical length scales in the micro and macro-scale, respectively. Section 2.3 explains the two-scale modeling approach that is used in this study. The micromechanical results of the hook-and-loop fastener along with experimental validations are presented in Section 2.3.1. Section 2.3.2 discusses the numerical and experimental results of the DCB test (macro-scale model) using the two-scale modeling approach. Finally, the discussion and conclusions are presented in Section 2.4 and Section 2.5, respectively.

2.2 Geometrical and physical length scales in a hook-and-loop fastener

2.2.1 Geometrical length scale

The mechanical performance of the hook-and-loop fastener depends on the ability of the loops to engage within the hooks at the sub-millimeter level. Hook-and-loop fasteners are typically available in different shapes, forms, and sizes. However, for this present work, we focus on a double-arm-hook model geometry, in which each hook is composed of two individual and opposing arms, as shown in Figure 2.1a. The multiscale characteristics and dimensions of these hooks and loops are presented in Figure 2.1a and b, respectively. The loop and hook tapes consist of columns with several loops and hooks, as shown in Figure 2.1. In this section, we present the geometrical details of the hook-and-loop fastener (micromechanical scale). The orientation of the hooks is described in terms of their principal direction axis *123*. Hooks are arranged in a square pattern, spaced 1.4 mm and 0.5 mm in direction *1* and *2*, respectively. The loops have an initial arch-shape geometry and are arranged in columns, as shown in the Scanning Electron Microscope (SEM) image in Figure 2.1b. During the engagement process, before a pullout experiment, hook-and-loop tapes are typically oriented parallel to direction *2* and facing each other in direction *3* to proceed with the engagement. The loop length ranges between 3 and 7 mm, and a diameter of 22±2 microns.

2.2.2 Physical length scale

Figure 2.1a and b illustrates the presence of various geometrical length scales in the hook-and-loop fasteners at the micromechanical scale. Understanding the mechanical behavior of the system and the relationship between geometrical and material length scales is essential to get the correct behavior of the fasteners [42,75]. Various standard test methods (i.e., peel tests, DCB test) exist to measure the mechanical properties of the hook-and-loop fasteners on the macro scale. Figure 2.1c presents the schematic of a typical peel tests under mode-I loading conditions which illustrates an emerging region that denotes a new length scale associated to the dissipative and irreversible process of the detachment of the hooks and loos. In particular we call this region the Detachment Process Zone (DPZ) as shown in Figure 2.1d. The DPZ is defined as the area around the crack tip of the sample where the hooks and deformed loops are still in contact. Inside the DPZ model Δ, D represents the characteristic length scale for deformed hook-and-loop system and detachment process zone length, respectively (see Figure 2.1d). The effective traction σ_{eff} is defined by a total force divided by the hook tape area. By using the stress-displacement curve from the micromechanical model, one can calculate the maximum effective traction, σ_{max}, and the total energy dissipation per unit area, φ (the area below the stress-displacement curve, Figure 2.1d), of a hook-and-loop fastener. This information can be used as an input to develop a macromechanical models which are discussed later in the paper. Finally, one should consider that the process of fiber pullout is irreversible, and this mechanism is responsible for energy dissipation during detachment of the hook-and-loop fastener.

2.3 The two-scale model strategy of hook-and-loop fastener

Here, we propose a two-scale model strategy to study the behavior of hook-and-loop fasteners. Here two-scale means that simulations will be done at two distinction scales: using only basic information about the geometry and mechanical behavior of the basic building blocks, such strategy will allow to make predictions of larger structural joints that use hook-and-loop fasteners, connecting the output from the micromechanical to the macromechanical scale. The concept of connecting various scales through multiscale strategies like this has been gaining popularity in the last few years. For example, the multi-scale cohesive model was used to obtain the homogenized macroscopic properties of the adhesives by capturing the details of failure at the microscopic level.[76]

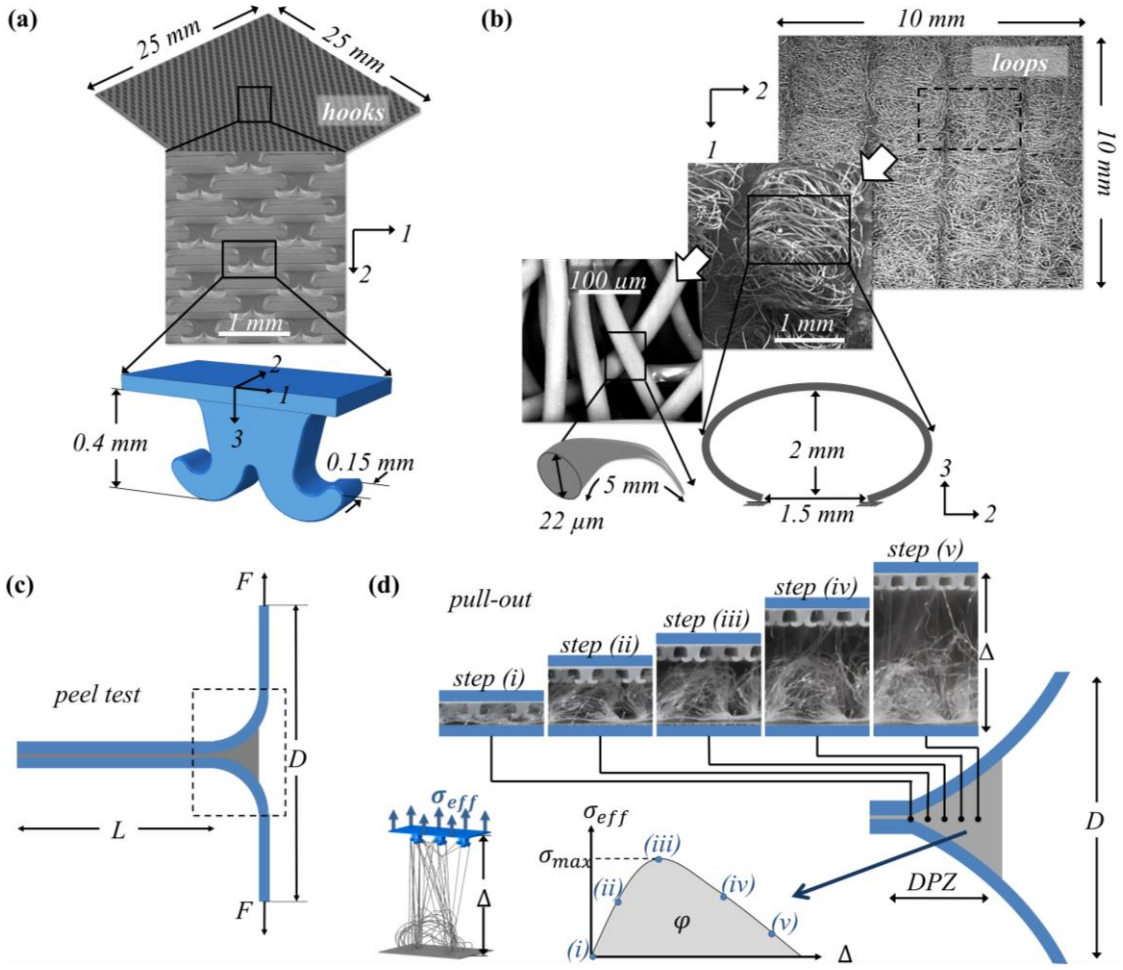

Figure 2.1. Geometrical length and physical length scales in the hook-and-loop tape.
SEM images and schematic representation of (a) hook tape (b) and loop tape. (c) Schematic representation of a peel test with applied forces and the total length of the sample. (d) Detailed representation of the DPZ connecting the results of micromechanical model as an input for the macromechanical model.

For the micromechanical model considered in this work, we consider both material properties and detailed geometry of the hook-and-loop fasteners. To this aim, we define a small Representative Hook and Loop Element (RHLE) domain to represent the mechanisms acting inside the DPZ at the microscopic level. In general, the RHLE should contain the most important details of individual building blocks (e.g., loops and hooks), and be large enough to statistically represent the collective behavior of the hooks and loops (including their material and geometrical variability); however, it should also be small enough to make the computational process more effective. Based on this multi-scale approach, the output from the RHLE domain is then used to predict the behavior of the fastener at the macro-scale (i.e., for instance to capture the mechanical behavior during a peel test, or a DCB test). The two-scale model strategy is valid if the two

following conditions are satisfied: i) the size of the RHLE domain should be selected much smaller with respect to DPZ in order to satisfy uniform conditions in the traction-displacement field and as a result, represent the mechanical behavior inside the DPZ. ii) the entire detachment steps (i.e., steps (i)-(v) in Figure 2.1d) can be represented by a unique traction-separation law. The DPZ describes the behavior of the interface when two interlocking surfaces (i.e., such as those of the hooks and loops), during the detachment process up to the point of separation. In the DCB geometry with hooks and loops, for instance, the DPZ is described by a traction-separation law, in which the main parameters are the peak stress, the displacement at failure, and the separation energy (or work of fracture/separation) which can be obtained directly from the micromechanical model. This simple concept constitute the main basis of our two-scales approach and therefore, it is necessary to keep all the material-related and geometry-related characteristic length scales in consideration. We postulate that, such connection between length scales can be attained employing a cohesive zone-type method, such as the cohesive zone model (CZM model) at the macroscopic scale (Figure 2.1d). Finally, such macro-scale model will be able to predict the mechanical response of a mechanical systems (i.e., the DCB geometry, a peel test or any other mechanical test that involve hooks and loops) as shown in Figure 2.1d.

2.3.1 Micromechanical model: Stage (I)

The material properties of a single hook and single loop fastener were characterized using experiments. A schematic of the hook-and-loop fastener at the microscopic level is shown in Figure 2.2a. For this particular system, the total displacement (Δ) is defined as the sum of hooks and loops deformation on the vertical direction (direction 3) as shown with (Δ_h) and (Δ_l), respectively, until total failure. The effective traction, σ_{eff}, is the force divided by the equivalent cross section area (i.e., is 0.125 mm^2 for the single hook tape shown in Figure 2.2a). The hooks are made of polypropylene (PP) and deformed elastically during the tests. The material property of the hook is defined by Young's modulus of E_h = 1.3 GPa and Poisson's ratio of ν =0.45 (see Figure 2.2a). The loops consist of non-woven fibers and their diameter have certain variability along the length of the fiber. The mechanical property of an individual fiber is determined experimentally by measuring the required force to fracture it under tension. Since the single fiber can be considered to be under uniaxial stress conditions, the experimental force-displacement response (gray line in Figure 2.2b) is then converted into stress and strain using Equations 1 and 2.

$$\sigma = F/(2A_o cos\theta) \tag{1}$$

$$\varepsilon = \frac{d}{L_o} \tag{2}$$

The mechanical behavior of an individual loop is assumed to be elastic-plastic and it is described in terms of stress and strain by Equation 3.

$$\sigma = \begin{cases} E_f \varepsilon & if\ \varepsilon \leq \sigma^y / E_f \\ K\varepsilon^n & if\ \varepsilon > \sigma^y / E_f \end{cases} \tag{3}$$

Where $K = \sigma^y (E_f/\sigma^y)^n$, E_f is the loop Young's Modulus ($E_f = 251.89$ MPa), σ^y is the yield stress ($\sigma^y = 68\ MPa$), and n is the strain-hardening exponent ($n = 0.2$). The fiber is then assumed to fail at a fracture stress ($\sigma^* = 135\ MPa$), as shown in Figure 2.2b).

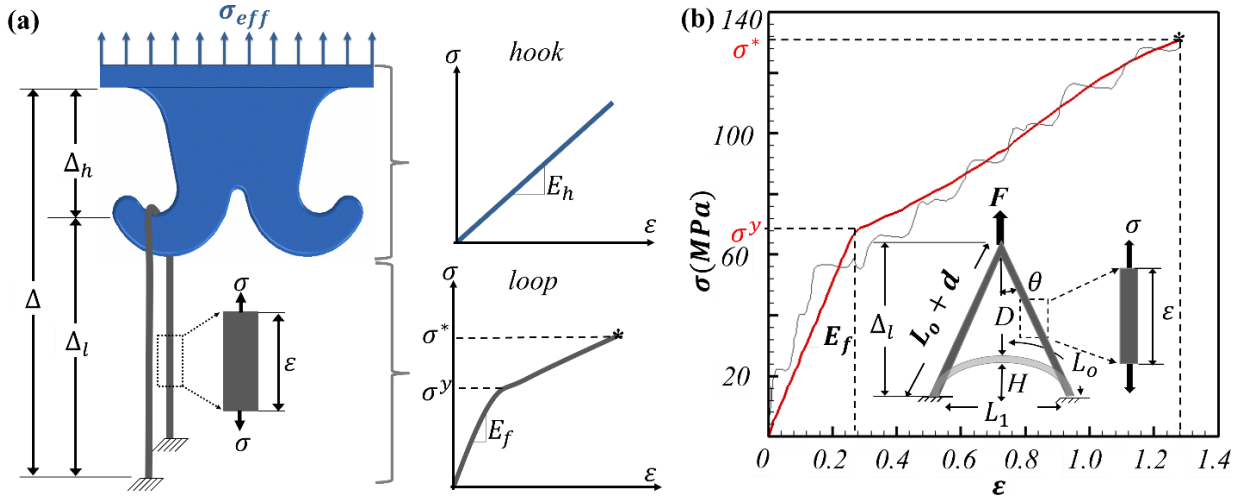

Figure 2.2. Description of the micromechanical model.
(a) Schematic representation of a hook-and-loop fastener with the mechanical behavior of individual hook and loop. Hooks only deform elastically, while loops are assumed to be elastic-plastic (b) stress vs strain curve for the fibers. The grey curve (experimental) depicts the averaged experimental data obtained through the pull-out test. The red curve (analytical) is the results of the mathematical formulation.

2.3.1.1 Experimental Approach

The loops in this study are mainly made from non-woven polypropylene fibers. Since the mechanical behavior and properties of the single polypropylene fiber are not available, we characterized single fibers by performing pull-out tests directly from the loop tape using a universal tensile testing machine (*MTS Insight 10)* as shown in Figure 2.3a and b. We used a single metal hook to perform the pull-out test, and a total of 8 tensile tests was performed by engaging various number of loops. Since the length and cross-section of the loops change throughout the

loop tape, we observe some variability in the force-displacement. Figure 2.3c shows the load-per-loop vs. displacement for all the tests. These values are obtained by dividing the total pull-out forces by the number of loops engaged with a metal hook during the experiment. The variability in the force-displacement curves can be explained due to several factors such as load distribution when multiple fibers of variable length engaged in the pullout process, the way fibers are connected to the film, the intrinsic material and diameter variability of the fibers. As a result of this variability, we use the averaged value of total tests (including multiple fibers) to gain more fundamental statistical distribution of the properties of an individual fiber [77]. Finally, these results reveal that the fibers behave as linear elastic-plastic materials which is typical of polymers (Figure **2.3**c).

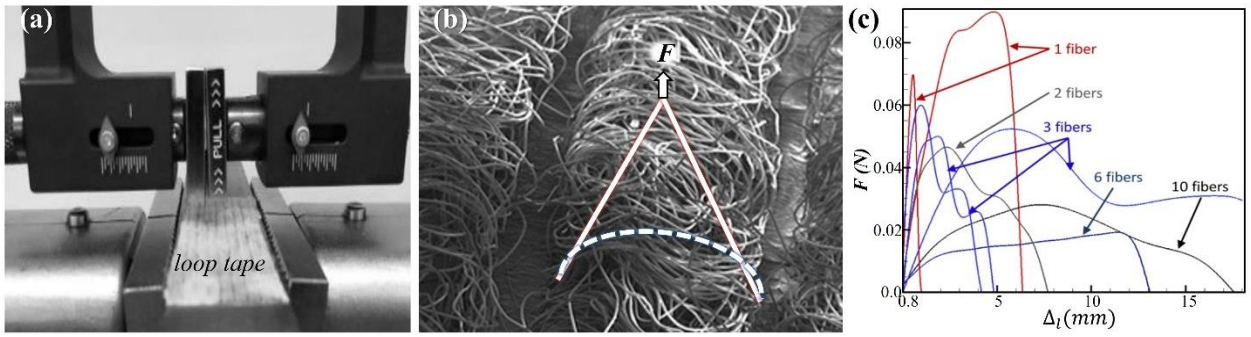

Figure 2.3. Material characterization of the loops.
(a) Experimental setup. (b) Schematics of the single fiber pullout experiment. (c) Experimental load-per-fiber vs. displacement curves for different tests done with varying number of fibers.

2.3.1.2 Numerical Approach

In this section, the analysis of the mechanical response of a single loop is presented. The load-displacement curves of a single loop under displacement-controlled conditions is shown in Figure 2.4a. Both ends of the fiber are fixed preventing translations and rotations. The load is applied at the middle point of the loop using a rigid pin (replicating the experimental setup described in Figure 2.3). For small values of the applied displacement, the loop begins to straighten with zero reaction force (from point (1) to (2) in Figure 2.4a). As the displacement increases, the loop begins to stretch elastically and deforms leading to a triangular shape (point 2 in Figure 2.4a). The deformation continues until it reaches the plastic yield stress of the material (point (3) in Figure 2.4a). After the yield point, the fiber deforms plastically until it reaches the maximum stress (failure stress) of the fiber (point (4) in Figure 2.4a), and it breaks at point (5).

An additional comparative study was performed to understand the role of fiber geometrical features such as cross-section and length in the mechanical performance of the fiber under tensile loading. To this aim, three fibers with various diameters (Φ = 20.746 μm, 21.11 μm, 22.93 μm) and lengths ($l = 4.487mm, 5.62mm, 6.137\ mm$) were considered. The comparison between the load-displacement curves of these three fibers shows a similar trend as the one shown Figure 2.4a. However, load required to yield the material plastically, the peak loads and failure strain are different as expected due to the variation in length and diameter (see Figure 2.4b). Moreover, Figure 2.4b confirms that as the diameter and length of the fibers increases, higher peak load and failure strain are obtained. Finally, a finite element model of the pull-out test for these three fibers is presented in Figure 2.4c. The numerical results confirm the trend observed in Figure 2.4a and b. However, the maximum peak load and failure strain are higher in comparison to the single fiber. Besides, at the failure point, three snap-through events can be observed. These events are related to the failure of each individual fiber. For instance, the first instability is associated with the fiber with smaller diameter and length while the last instability is related to the fiber with the largest geometrical features. Figure 2.2b presents the average stress-strain curve for an individual fibrous loop under tensile load. Initially the fiber, with a height (H) and length ($2L_0$), is stretched from the middle point a distance (D), creating a triangular shape. The two straight sides of the deformed loop form an angle θ which is equal to ($2(L_0 + d)$). The cross-section area (A_0) and distance between ends (L_1) are considered to be constant. The stress (σ) and strain (ε) included in Figure 2.2b are calculated using Equations 1-3.

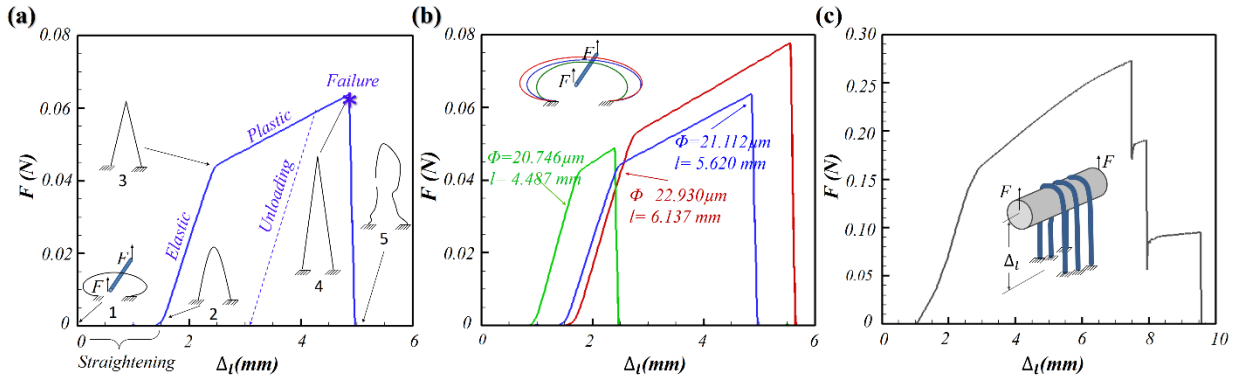

Figure 2.4. Force-displacement curve of a simple pull-out test of representative loops.
(a) Pull-out test of one loop, where (1) undeformed shape of the loop; (2) straightening; (3) elastic stretching; (4) plastic deformation at peak load until final failure (5), (b) Force-displacement curves of simple pull-out test for three individual loops with different length and cross-section areas. (c) Force-displacement curve of a simple pull-out test of three different loops. A rigid pin with a diameter $\emptyset \approx 0.1mm$ is used to pull the fibers.

2.3.1.3 Loop generator

To the best of our knowledge, there is no software currently available to generate finite element (FE) meshes using beam elements that mimics the geometries of the loop material considered in this research. For this reason, the loop mesh was generated by an algorithm written in C-language that creates each loop as a unique beam part with random changes in the shape, length, and cross-sectional area, following a normal distribution based in experimental observations as shown in Figure 2.5. Loops are manufactured by extrusion; this fabrication process generates a variability in the diameters along each loop (Figure 2.5a). However, for the purposes of the numerical model, it is possible to assign a single diameter value per loop while maintaining the normal distribution of diameters throughout the sample. That is, each loop in the sample is assigned a different but constant diameter following the experimental results. Similarly, the fabrication process of the loop tape generates uneven arches length that follows a normal distribution as well (Figure 2.5b). The implementation of those changes allows the computational model to be more realistic bringing the model closer to the real sample material behavior. The algorithm generates each loop and places it in specific locations across the tape until the desired dimension is achieved as shown in Figure 2.6.

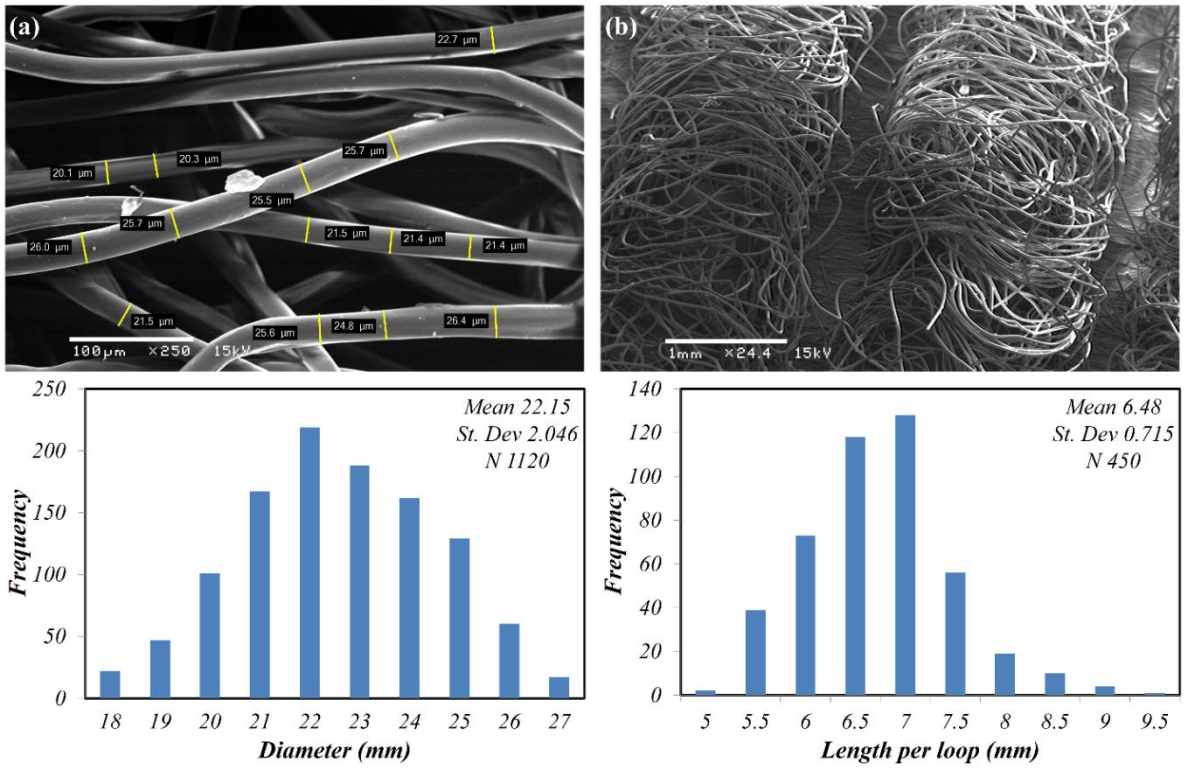

Figure 2.5. Variation of (a) diameters and (b) length along the loop tape following a normal distribution.

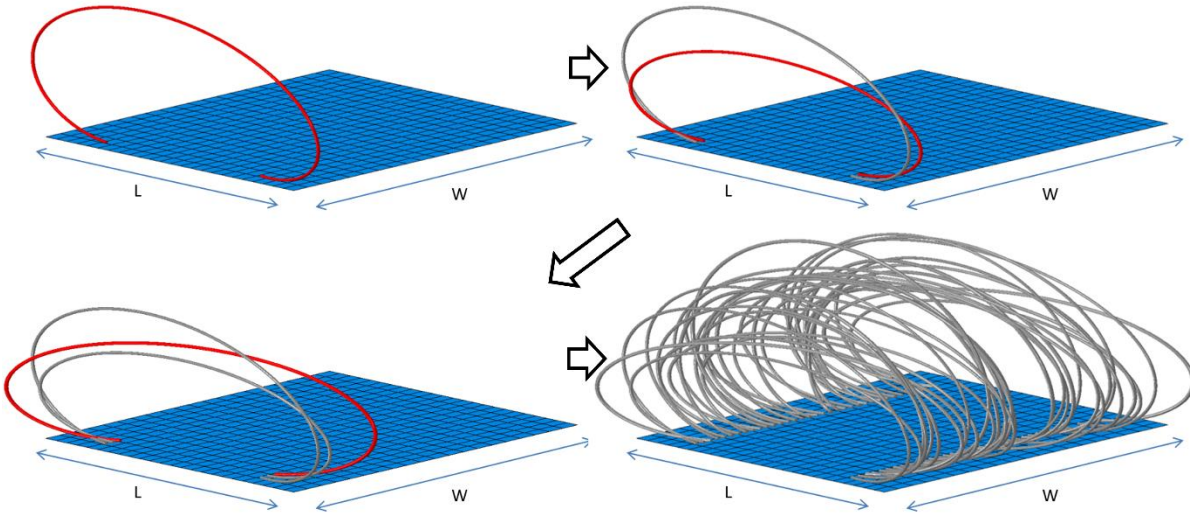

Figure 2.6. Loop Generator algorithm that creates the beam finite element mesh for the loop material. The code follows a dynamic and sequential packing algorithm where fibers are introduced one by one, checking for interference and contact with other fibers until the desired volume fraction is reached. Randomness in the position, shape, and angles, as well as stochastic distribution of defects, is considered in the code.

2.3.1.4 Mechanical behavior of the hooks

In this section, the role of an individual hook at the separation point is analyzed. In particular, we seek to determine the value of the maximum force required by a given number of fibers to bend the hook elastically in order to enable the fibers to be released from the hook. This analysis is independent from the fact that the loops may undergo plastic deformation and even fail before they can be released. Using a simplified analytical model,[78,79] the geometry of a single hook can be estimated by three geometric lengths; $L_h, L_w,$ and L_r ($L_h = 0.37mm, L_w = 0.30mm,$ and $L_r = 0.13mm$), as presented in Figure 2.7. Here, we describe a geometry of hook as a series of connected beams subjected to bending moments due to an applied force *F* as shown in Figure 2.7. In the analytical models, the dimensions of the beam are selected in such a way that all the beam dimensions satisfy the following equilibrium.

$$L_1 < L_h, L_2 < L_w, \; L_3 < L_r \tag{4}$$

Where the values of $L_1 = 0.30mm, L_2 = 0.20mm,$ and $L_3 = 0.05mm$ for this particular geometry. Similarly, both in-plane and out of plane thicknesses of all the beam cross-sections remain constant and are equal to *0.14 mm* and *0.15 mm*, respectively. These values are selected based on average values of thickness along with the hook geometry.

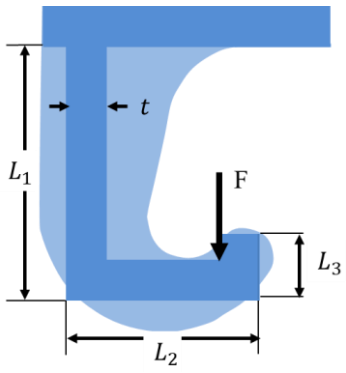

Figure 2.7. Schematic simplification of the hook with respective measurements.[78]

In this simplified analytical model, fiber pull-out occurs when the segment of L_3 becomes horizontal. Thus, these beams are needed to bend in such a way that the sum of the deflection angles is equal to 90 (Equation 5).

$$(\theta_1 + \theta_2 = \pi/2) \tag{5}$$

Using a beam theory,[78,79] the deflection for each beam can be calculated as follows:

$$\theta_1 = \frac{FL_2{}^2}{2EI} \text{ and } \theta_2 = \frac{FL_1L_2}{EI} \tag{6}$$

where F is peak force, E is the elastic modulus of the beam, I is a moment of inertia for the beam cross-section, and L_1 and L_2 are the lengths of the beam. For this particular problem, the values of E and I are equal to $1.3\ GPa$ and $3.43 \times 10^{-5}\ mm^4$, respectively. By substituting Equation 6 into Equation 5 we can find the values of peak load.

$$\theta_1 + \theta_2 = \frac{FL_2{}^2}{2EI} + \frac{FL_1L_2}{EI} = \frac{\pi}{2}$$

$$F\left(\frac{L_2{}^2 + 2L_2L_1}{2EI}\right) = \frac{\pi}{2}$$

$$F = 0.875N \tag{7}$$

Finally, the result of the numerical simulation of the pull-out test, including a single hook and loop, is compared with the peak force obtained from the analytical calculation, as shown in Figure 2.8. The comparison between the analytical model and numerical simulation confirms a good agreement in the values of peak load. As such, one could use an analytical model to predict the required force in order to pull-out occurs, the analytical model cannot predict the entire

behavior of hook-and-loop fastener for the history of detachment process (i.e., interaction between the hook and the loop).

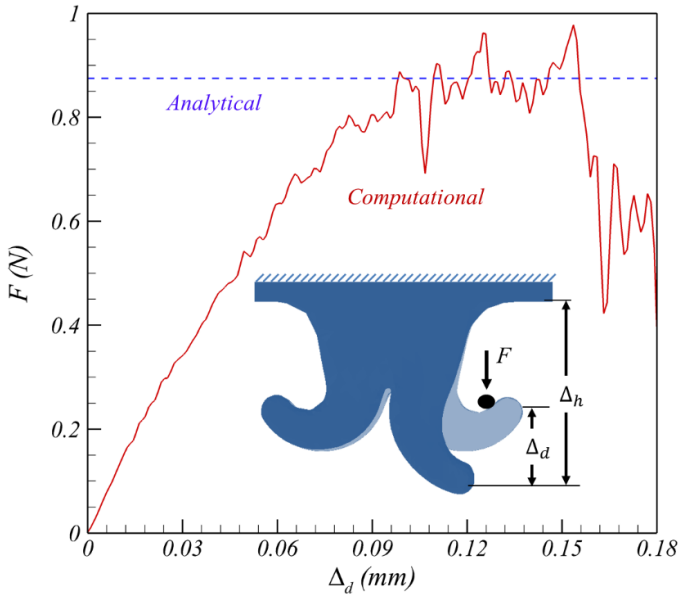

Figure 2.8. Force-displacement curve required to bend a single arm of the hook compared with the analytical solution.
Oscillations in the measures are due to instabilities of the process captured with Abaqus/Explicit formulation

The observations during the detachment process of a hook-and-loop fastener from both numerical simulations and experiments confirm that each hook at least engages with 3 to 4 fibers. Therefore, for most cases, the required force to bend a single hook exceeds the required force to break a single fiber.

2.3.1.5 Two-step process: engagement and pull-out

The RHLE model in this study consists of a total of six hooks and thirty-two loops as previously described in Section 2.1. During the analysis, the ends of the loops were fixed and clamped to the substrate (i.e., both translation and rotation degrees of freedom were constrained). The origin of the coordinate system was placed at the lowest corner of the loops tape (Figure 2.9a). General contact with no-penetration and no-friction was assigned between all the loops and hooks. Two loading steps are considered: (i) engagement and (ii) pull-out, as shown in Figure 2.9. At the beginning of the engagement step, the hooks tape is placed at $\Delta_0 = 2\ mm$ (with respect to the origin of the coordinate system). At such distance, there is no contact between loops and hooks (initial step in Figure 2.9). In the engagement step, a uniform displacement rate is applied on the

top surface of the hook tape towards the loops tape compressing the hooks into the fibers. This loading step continues until it reaches to $\Delta_1 = 0.8$ mm. This final height in the engagement step is selected such that it enables all the loops (even the loops with the lowest height) to come into contact with the hooks, maximizing the engagement and promoting interlocking with the hooks, while keeping the top surfaces of the hooks away from the bottom surface of the loops to avoid higher forces and plastic deformation (i.e., due to the geometry and material properties, the computational cost increases significantly, leading to nonlinear behavior and potential numerical instabilities). Similar to what it was shown in Figure 2.2a, the effective traction, σ_{eff}, is obtained by the total force applied to the hook tape divided by its area (the area of the RHLE is 6.88 mm^2). The numerical implementation of this steps is done with Abaqus/Standard using an implicit scheme which is computationally efficient as it is unconditionally stable.[80] The process then continues with the detachment process (i.e., pull-out) by applying opening displacement, starting at $\Delta_1 = 0.8\,mm$, until the complete separation occurs. This pull-out step could, in principle, be assumed to be quasi-static; however, due to the snap-through instabilities caused by the sudden release or fracture of some fibers, dynamic effects should be expected. As such, and only for the pullout process, we switch the analysis to dynamic explicit using Abaqus/Explicit[80] which performs better in terms of damage, failure, and instabilities. In order to replicate the quasi-static conditions of the experiments, a very slow displacement rate was applied on the top surface of the hook. In the pull-out step, the hook tape moves upward until the complete separation observed at around $\Delta_2 = 6.8$ mm.

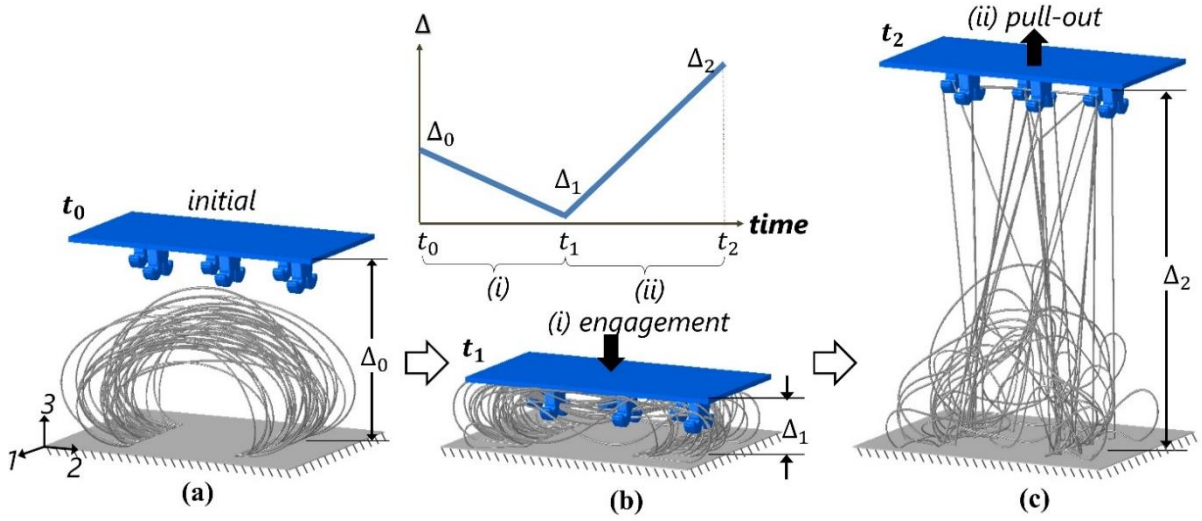

Figure 2.9. Deformation process for the micromechanical model of the RHLE.
(a) initial position, (b) engagement step, (c) pull-out step.

2.3.1.6 Boundary conditions

In order to mimic the correct behavior of hook-and-loop fasteners in the micromechanical model regardless of the sample size, we employ periodic boundary conditions (PBC) at selected loops located at the boundaries of the RHLE domain (Figure 2.10). The PBC enables us to produce a model that represents an infinite system by using small computational domains such as the RHLE. Figure 2.10a shows an SEM image of the loops and their arrangements inside the tapes. Based on experimental observation, loops in the adjacent columns do not interact with each other; therefore, periodicity was only considered in direction 1, as shown in Figure 2.10a. and b shows a 10 mm by 10 mm hook-and-loop fastener with 144 hooks and 600 loops. Figure 2.10c and d shows good qualitative agreement between the finite element analysis and the experiments for the selected RHLE.

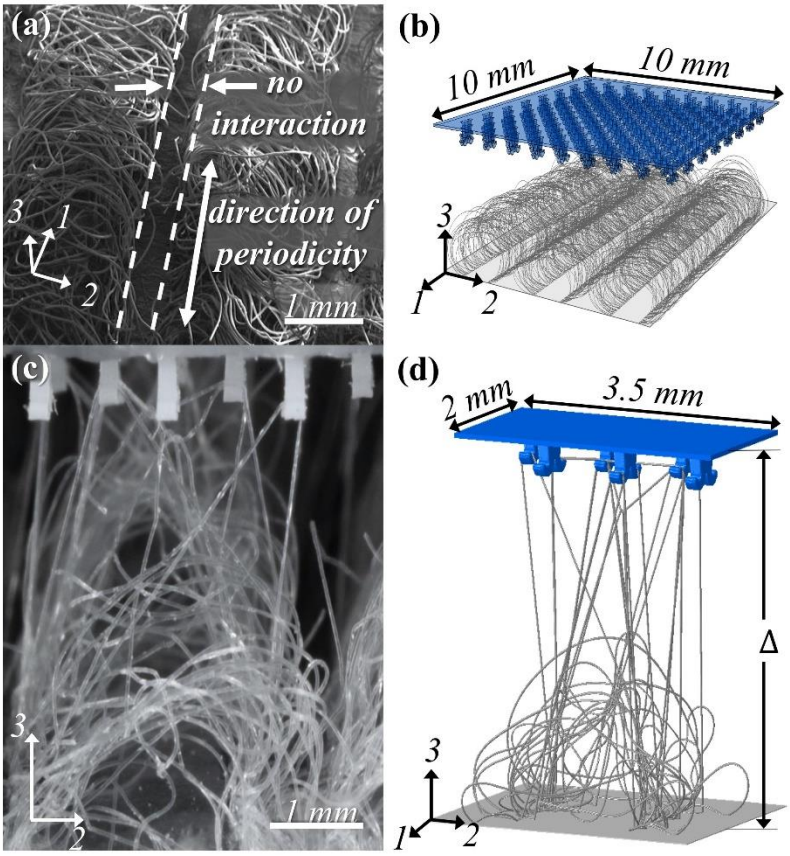

Figure 2.10. Selection of Representative Hook and Loop Element (RHLE).
(a) SEM image of loop tape with initial considerations, no interaction between columns of loops and periodicity direction (b) Schematic of a large hook-and-loop fastener. (c) Experimental observation of hook-and-loop tape in pull-out step. (d) RHLE is composed by 6 hooks and 32 loops showing good agreement with the experimental observations.

To achieve periodicity for the loops inside the RHLE, the loops at the one end of the borders ("master loops") are replicated and translated to the other end of the boundary domain ("slave loops"), as shown in Figure 2.11. Then, for each master loop, an identical slave loop exists (see Figure 2.11a) where the nodes on the slave loop are kinematically coupled to their respective nodes in a master loop. As a result, the same displacement and constraints are applied to both master and slave loops during the attachment and detachment processes. In our RHLE, the PBC are applied to the last three loops in the boundary domain (Figure 2.11b). The kinematic constraints between master and slave loops enable the nodes in both master or slave to move with each other regardless of their contact with the hooks. This process ensure that contact also occurs in the slave loops. All other loops in the middle of the RHLE (denoted as "random loops" in Figure 2.11c), which are not either master or slave, can move independently. Finally, Figure 2.11d shows the pull-out process showing deformation of the loops (including the salves and masters).

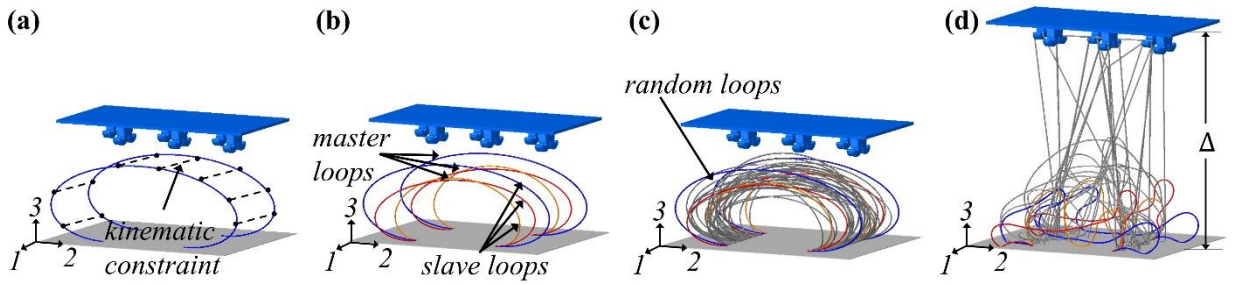

Figure 2.11. Periodic Boundary Conditions (PBCs).
(a) the master and slave loop are connected with kinematic constrains. (b) three sets of slave and master loops are placed at each end of the RHLE to simulate periodicity in the longitudinal direction (i.e., direction 1). (c) individual loops with statistical variability are placed in the middle to fill the rest of the RHLE. (d) pull-out step with the RHLE showing the equal deformation pattern of the coupled loops.

2.3.1.7 Results for the micromechanical model

We created and analyzed 15 different RHLE finite element models; each one with a unique combination of loops with geometrical variability that follows a statistical distribution as described in Section 2.3.1.3. This will provide a statistical range of the mechanical response of the RHLE considering material and geometrical variability. The resulting effective traction-displacement ($\sigma_{eff} - \Delta$) obtained from these numerical simulations are shown in Figure 2.12a. While the entire simulation consists of the engaging and pullout process (as described in Figure 2.9) only the pullout portion is plotted, initiating at $\Delta_1 = 0.8\ mm$ (minimum displacement reached during the engagement step), until complete separation at $\Delta_2 = 6.8\ mm$. The result of the engaging process is

a system of hooks engaging a given number of loops. Due to the statistical distribution of the geometrical variation of the loops, each simulation ends up with different number of loops being engaged to the hooks which, as consequence, determines the mechanical behavior during the pullout process. The individual simulations are shown in dashed grey lines. The solid green line describes the average values of $\sigma_{eff} - \Delta$ and the light green area bounds the maximum and minimum standard deviation. Figure 2.12b-d describes the deformation sequence of one of the RHLE illustrating three distinct mechanisms found during the engagement (Figure 2.12b) and pull-out (Figure 2.12c) process. In particular, Figure 2.12d shows fiber entanglement and interlocking at an advanced stage of the pull-out process.

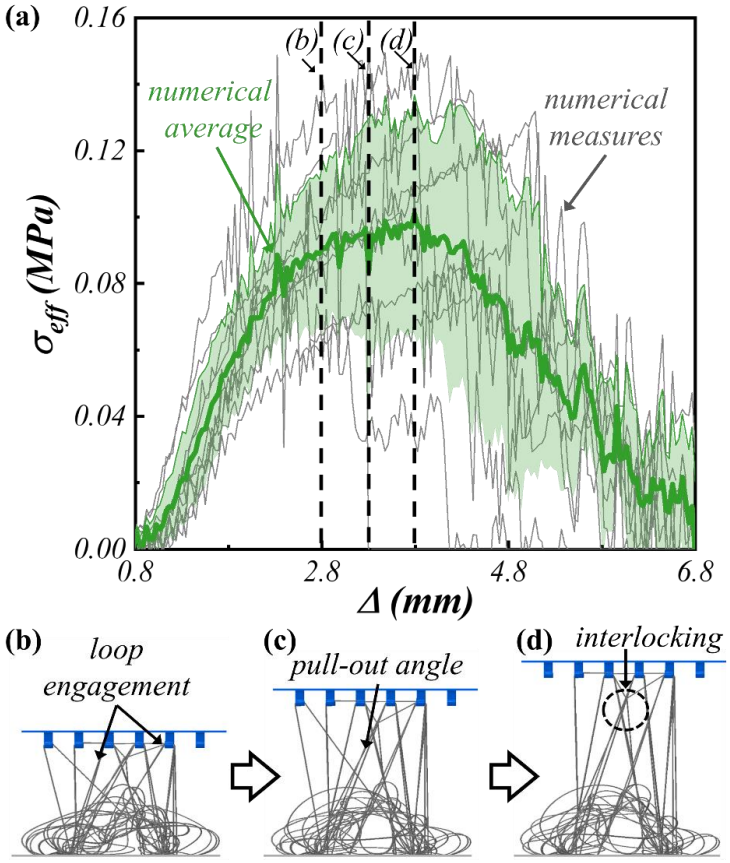

Figure 2.12. Numerical simulation for the micromechanical model. Pull-out step.

(a) σ_{eff}-Δ curves for the 15 numerical simulations (gray) with average curve (green), within a light green area computed from the maximum and minimum standard deviation. The dashed black vertical lines correspond to the deformation position of panels (b), (c), and (d) (b) hook and loop engagement at the initial state of pull-out step. (c) deformation of the fibers that reveals different pull-out angles. (d) fiber entanglement during the pull-out process which increases the interaction between loops inducing their interlocking.

The result of these simulations allows us to make several observations. First, we notice that the fracture of the loops do not take place simultaneously. Instead, the individual loops fracture

one at the time. The collective behavior of individual mechanisms such as these fibers resemble a similar behavior exhibited by protein and long molecules found in the interface of some naturally-occurring materials such as nacre.[63] The values of the force shown in Figure 2.12 depends on the number of loops that are engaged in the pullout process. The cases with higher number of loops being pulled out by the hooks (e.g., typically around 15 loops) are the ones exhibiting higher values of σ_{eff} , whereas the ones with 7 or less loops engaged in the pullout process are the ones giving the lower values of σ_{eff}. The maximum value of σ_{eff} , which can represent the strength of the RHLE, depends on two competing mechanisms: fracture of the individual loops versus the release of the loops by elastic deformation of the hooks. This competition heavily relies on the number of loops that are engaged with a single hook. In average, each individual hook engages about 3 loops. Under tensile deformation, the force required to fracture three loops oscillates around 0.27 N (Figure 2.4c). On the other hand, each individual hook requires a force of approximately 0.875N to deform, bend and release the loops (Figure 2.8). This means that 3 loops are more likely to fracture than to bend the hook.

The geometrical variability of the individual fibers also causes the loops to fracture at different force levels. Shorter loops tend to fracture earlier than the longer loops during the pull-out deformation process. The fiber diameter also plays an important role in determining when the fibers break. Since the loops are mostly subjected to uniaxial stress conditions, except where they contact the hooks, the loops fracture when their stress reach the fracture stress ($\sigma^* = 135\ MPa$). As such, the shortest fibers tend to break at $\Delta \approx 2.1\ mm$, while the longest at $\Delta \approx 6\ mm$, and the average fiber will break at around $\Delta \approx 4\ mm$. The collective contribution of these mechanisms leads to σ_{eff} vs. Δ curves that exhibit several peaks and drops of the stress denoting local snap-through instabilities driven by the fracture or sudden release of the fibers. Figure 2.13 describes two representative cases in more details. The grey line represents one of the cases with higher resulting peak stress, whereas the blue curve represents a case with low peak stress, both with their corresponding number of loops that are engaged at some selected steps. For instance, the case that leads to higher stress initially pulls 15 loops, until it reaches the first peak at about 0.14 MPa (which correspond to a total force of 0.95 N). The sudden drop corresponds to the fracture of the first fiber, leaving only 14 fibers until the second and highest peak at about 0.15 MPa (with a total force of 1.1 N) in Figure 2.13i . The subsequent drops correspond to a series of fracture events that affect 6 loops (Figure 2.13ii). The final large drop corresponds to a group of 5 loops leaving only 3 loops

(Figure 2.13iii) that are being stretched at a force lower than 0.3 N (or at a stress lower than 0.04 MPa). The blue line corresponds to one of the cases that engages a lower number of loops (i.e., 7 loops); however, the pull-out process follows a similar trend. The number of loops that can fracture at once, does seem to be more stochastic in nature due to the material and geometrical variability. Shorter loops contribute to increase the force at shorter distances (higher initial slope) and longer loops contribute to extend this force for larger displacements. Additionally, we observe relatively long fibers engaging more than one hook (both cases can be observed in Figure 2.13). This uneven fracture process of the loops, which results in the jagged stress-displacement curve in the current RHLE, is expected to become smooth as larger collections of hooks and loops are considered. On the other hand, the average behavior shown as a green curve in Figure 2.12, which considers a group of individual simulations with statistical variations of the loops geometry, can also be representative of larger RHLEs.

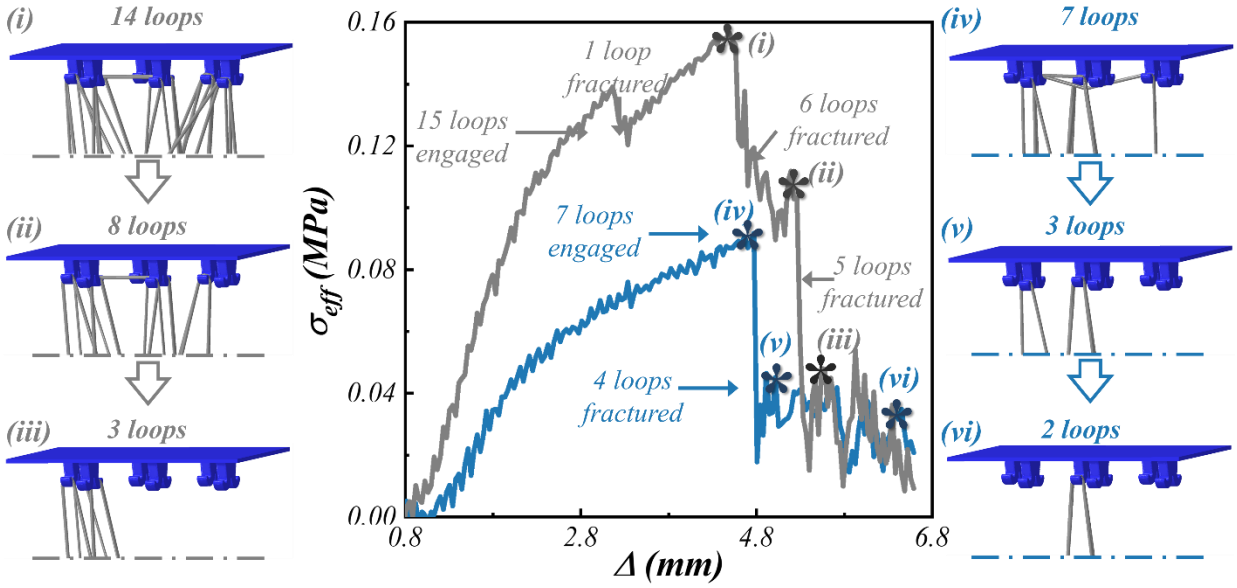

Figure 2.13. Detailed description of two different numerical simulations for the micromechanical model. The gray line represents the force-displacement for 15 loops engaged (high force) while the blue curve represents the force-displacement for 7 loops engaged (low force).

The results in Figure 2.12 and Figure 2.13 also reveal general mechanical behavior like total energy dissipated through the pullout process (or work of separation) of the RHLE, which can be calculated as the area below the curve. As we can observe, the multiple fracture events promote energy dissipation per unit area in the system. The more distributed the fracture events are, leading to a smoother decaying/degrading curve, the more energy is dissipated through the process.

2.3.1.8 Effect of the RHLE size

The RHLE size was chosen based on the material behavior and the capability of the RHLE domains with different sizes to reproduce the same result. However, the selection of the hook tape size was done in the undeformed configuration. Figure 2.14 shows the comparison between the two RHLE of different sizes. From the deformed configuration of the RHLE with 6 loops (Figure 2.14a) it is evident that the loops are pushed away and spread out of the sample arising the question if more hooks are needed to fulfill the requirements of periodicity. Consequently, the second set of simulations was performed with a slightly larger RHLE, with 8 hooks, adding one extra hook to the ends of each row, Figure 2.14b. The load-displacement curve was recorded for both cases (Figure 2.14c) and can be concluded that the difference in engagement is subtle . The result from this numerical test validate the assumption that 6 hooks is sufficient to capture the "real area" of engagement between hooks and loops.

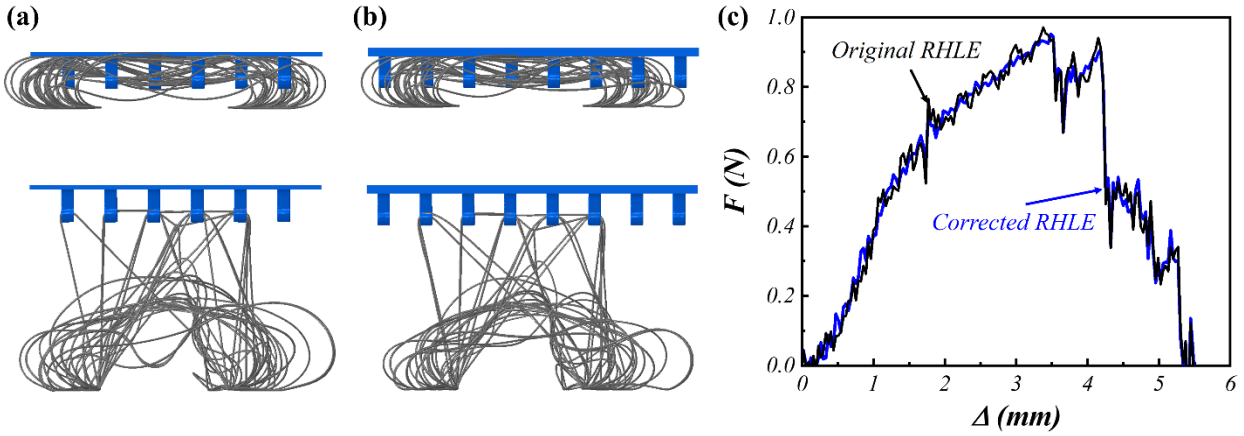

Figure 2.14. Effect of the RHLE size.
(a) RHLE size with six hooks and (b) RHLE size with eight hooks, one added to each end of the tape. (c) Force-displacement curve comparing the two RHLEs.

2.3.1.9 Hook rotation analysis

As discussed in Section 3, the output results from micromechanical models are used as an input for macromechanical analysis. During the detachment process in the micromechanical models, both hooks and loops are placed on top of each other, parallel the plane 1-2 and faced in the direction perpendicular to 3, as shown in Figure 2.1. On the other hand, the interaction between hooks and loops right at DPZ during the DCB test takes place at an angle ζ (Figure 2.17). In order to assess the effect of using data from the micromechanical model (that assume pure mode I conditions) on the micromechanical model, we investigated the effect of hooks rotation on the

mechanical response of the micromechanical model. To this aim, two sets of micromechanical models with and without hooks rotation were developed, as presented in Figure 2.15a and b, respectively. The comparison between the load-displacement of these two cases is presented in Figure 2.15c. The results state that the model with rotated hooks tape (solid red curve) shows higher values of reaction force in comparison to the case without rotation (solid blue curve). Figure 2.15c also presents the numerical results of zero rotated hooks with a variety of loops statistically oriented. The results comparison showed good consistency between two models and also confirmed that the current assumption on micromechanical modeling of a hook-and-loop fastener is valid to use as an input for macromechanical model (i.e., peel test in DCB) and as a result, the effect of initial hooks rotation can be ignored.

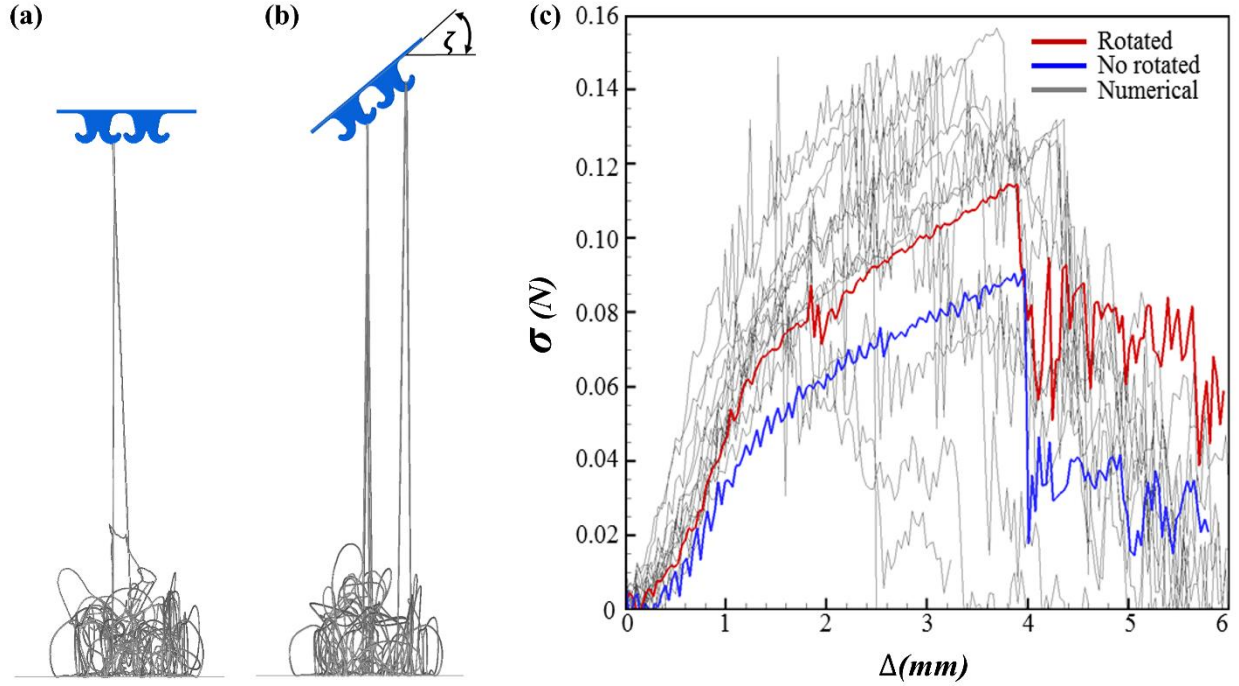

Figure 2.15. Schematics of hook-and-loop fastener.
(a) hooks tape without rotation, (b) hooks tape with rotation. (c) The load-displacement curves of hook-and-loop fastener with and without hooks tape rotation, and various loops orientations (shown in grey) for hooks tape without rotation.

2.3.1.10 Micromechanical experimental tests

The primary purpose of the experimental tests is to validate the numerical results obtained in Section 2.3.1.7. The experiments consisted in testing a set of 40 mm by 40 mm hook-and-loop fasteners already engaged under tensile load and quasi-static conditions until complete separation.

Both hooks and loops tapes were attached to 3D printed T-shaped grips using a strong adhesive (See Figure 2.16a). The adhesive was monitored during the experiments to ensure there was no delamination. Each test starts with an initial engaging process. The process starts by aligning and pressing the two parts against each other. To have a consistent engagement process among samples, each sample was also subjected to 10 cycles and shear deformation with a nominal load of approximately 10 kPa. We observed that this procedure ensures an average of at least three fibers engagement per single hook arm (similar to the numerical simulations). The samples were placed in a universal tensile testing machine (MTS Insight 10) with a 1 kN load cell. A series of tests at different low loading rates were performed, and it was found that applying a displacement rate of 3 mm/min on the top surfaces of the hooks guarantees no loading-rate or viscoelastic effect. The resulting effective traction vs. displacement ($\sigma_{eff} - \Delta$) curves are shown as dashed grey lines in Figure 2.16b representing the test done on ten different specimens. The average values of these curves is represented by the blue solid curve, whereas the light blue area is delimited by the standard deviation. Optical micrographs of the pull-out process of the hook-and-loop fastener are presented in Figure 2.16c-e. These images reveal three distinct mechanisms: loop engagement, pull-out, and loop interlocking; similar to was predicted by the FE models (Figure 2.12b-d). The variability on the initial loading slope observed in both numerical simulations and experiments can be attributed to the statistical distribution of the loops geometry and loop lengths, as well as variation in the number of loops that engage during the interaction. As previously discussed, the initial number of engagements and the variability in length of the loops are responsible for the variation in stiffness. Finally, the comparison between experimental results and FE simulations is shown as an inset figure in Figure 2.16b. This comparison confirms that the loops deformation and fracture is a dominant mechanism in the pullout process. Careful inspection of the hooks specimens after each test indicated that the hooks did not deform inelastically or underwent any damage during the pullout process, validating our hypothesis that the hooks only deform elastically in these hook-and-loop systems. However, we observed two failure mechanisms depending on the length of the loop: pull-out and fracture. For very short fibers, the fracture was observed inside the loops while in this set of experiments most of the loops deformed plastically until the final sudden release of the individual loops as observed in most cases in our simulations.

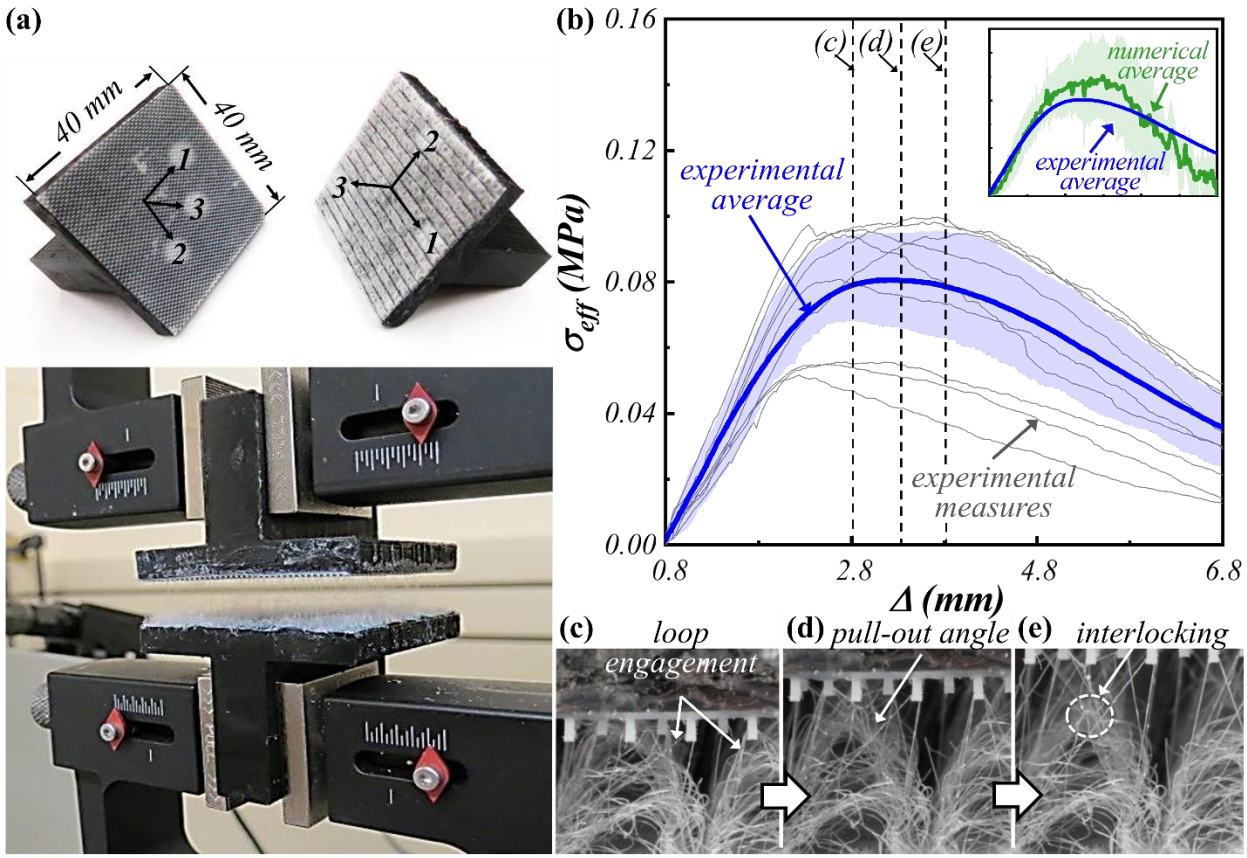

Figure 2.16. Micromechanical experimental test.
(a) "T" shape samples with hook and loops (top) and assembly placed in the grips of the MTS machine (bottom). (b) Experimental results for the micromechanical test (gray lines) with average curve (blue) within a light blue area computed from the maximum and minimum standard deviation of the experimental results. In the inset, the comparison between the average experimental results (blue line) and the average numerical simulations results (green line) for the micromechanical test, the light green area is defined by the standard deviation of the numerical results. Dashed black lines correspond to the deformation position of panels (c), (d), and (e). (c) hook and loop engagement at the initial state of the experimental pull-out step. (d) engagement and deformation of fibers reveal different pull-out angles. (e) pull-out process increases the interaction between loops inducing their interlocking.

2.3.2 Macromechanical model: Stage (II)

In this section, the information from the high-fidelity micromechanical model is employed to capture the macroscopic behavior of fasteners in the macromechanical stage, such as the DCB test. Figure 2.17 represents the schematic of the transition from microscopic to macroscopic model (DCB peel model) where the effective traction-separation ($\sigma_{eff} - \Delta$) results from the micromechanical model is used as an input for the cohesive zone layer as previously discussed. The DCB model depicted in Figure 2.17 consist of two strips made of a homogeneous elastic material with part of its length (*L*-*a*) connected using a hook and a loop tape glued on both sides of the strip. *a* is the initial length of the crack and L is the entire length of the DCB. As the load is

applied at the ends of the individual beams, the crack propagates from left to right as shown in Figure 2.17. The DPZ then develops ahead of the crack tip. To obtain the correct of $\sigma_{eff} - \Delta$ response, we adopt a potential-based cohesive model[81,82] which is available as a user-defined element (UEL) and allows us to capture the correct shape of traction-separation model that observed numerically and experimentally. While the micromechanical model provides the necessary of $\sigma_{eff} - \Delta$ response under pure opening (Mode I) mode, there are certain aspects of the DCB that need to be considered. First, the DCB needs to be symmetric in order to replicate mode I conditions at the crack tip. This is partially true considering that the hook-and-loop tapes can be glued to two elastic strips of equal thickness and mechanical properties. Considering that the bending stiffness of the strips is high enough, any asymmetry given by the fact that one strip contains the hooks and the other strip has the loops is minimized. The other geometrical aspect is related to the angle, ζ between the strip and the horizontal line right at the crack tip (Figure 2.17b). If ζ is significant, then the loops and hooks will be subject to side loads (as opposed to the ideal condition depicted in Figure 2.9-Figure 2.11). The effect of ζ on micromechanical model was investigated and presented in Section 2.3.1.9. For the scope of this work, we consider that ζ is small enough (smaller than 25°).

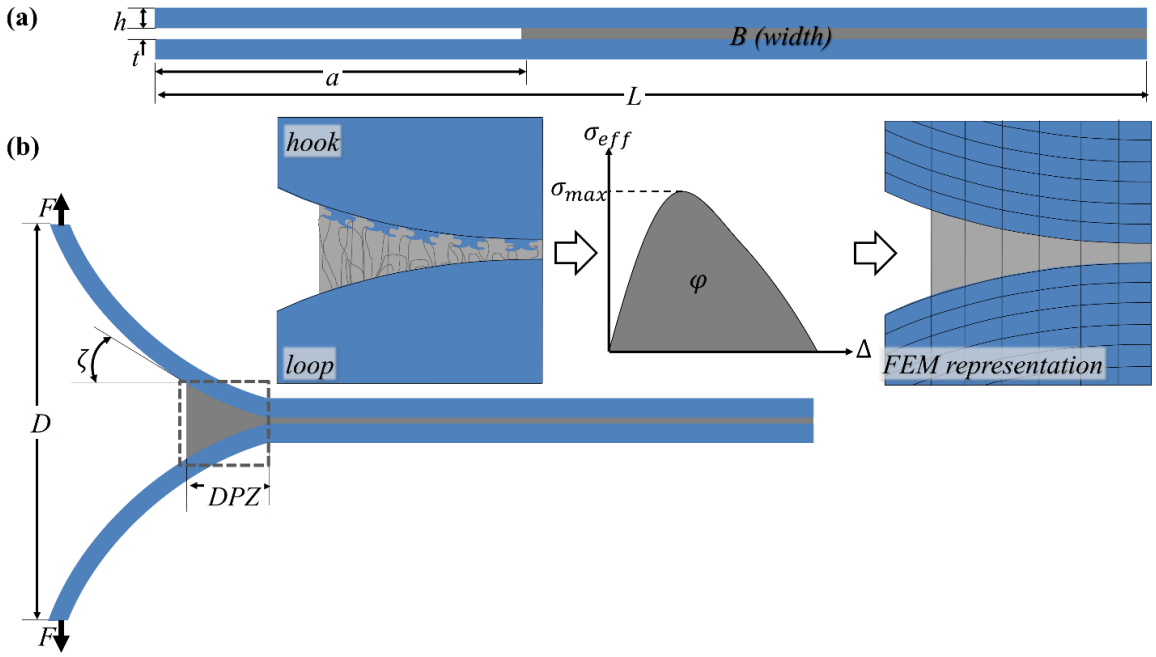

Figure 2.17. The transition between micromechanical and micromechanical model.
(a) A schematic of the DCB specimen employed in this study. (b) The specimens are loaded on both free end with a force (F) perpendicular to the hook and loop surfaces to separate them. To ensure mode I conditions only, the geometry of the beam was controlled such as the curvature induced by the bending moment and the local rotation angle between the two surfaces, ζ,was kept under 25◦degrees.

2.3.2.1 Detachment Process Zone (DPZ)

As previously discussed, the DPZ, which emerges from the interaction of the loops and hooks ahead of the crack tip in a crack propagation situations such as those depicted in the DCB case (Figure 2.1 and Figure 2.17) can be described by a cohesive model. The cohesive zone model adopted for this work is described in terms of its normal and tangential cohesive tractions in Equation 8 and Equation 9.[82]

$$\sigma(\Delta_n,\Delta_t)=\frac{\Gamma_n}{\delta_n}\left[m\left(1-\frac{\Delta_n}{\delta_n}\right)^{\alpha}\left(\frac{m}{\alpha}+\frac{\Delta_n}{\delta_n}\right)^{m-1}-\alpha\left(1-\frac{\Delta_n}{\delta_n}\right)^{\alpha-1}\left(\frac{m}{\alpha}+\frac{\Delta_n}{\delta_n}\right)^{m}\right]\times\left[\Gamma_t\left(1-\frac{|\Delta_t|}{\delta_t}\right)^{\beta}\left(\frac{n}{\beta}+\frac{|\Delta_t|}{\delta_t}\right)^{n}+\langle\phi_t-\phi_n\rangle\right] \quad (8)$$

$$\Gamma(\Delta_n,\Delta_t)=\frac{\Gamma_t}{\delta_t}\left[n\left(1-\frac{|\Delta_t|}{\delta_t}\right)^{\beta}\left(\frac{n}{\beta}+\frac{|\Delta_t|}{\delta_t}\right)^{n-1}-\beta\left(1-\frac{|\Delta_t|}{\delta_t}\right)^{\beta-1}\left(\frac{n}{\beta}+\frac{|\Delta_t|}{\delta_t}\right)^{n}\right]\times\left[\Gamma_n\left(1-\frac{|\Delta_n|}{\delta_n}\right)^{\alpha}\left(\frac{m}{\alpha}+\frac{\Delta_n}{\delta_n}\right)^{m}+\langle\phi_n-\phi_t\rangle\right]\frac{|\Delta_t|}{\delta_t} \quad (9)$$

In Equation 4, α and β represent the shape parameters; $\delta, \Delta, \phi,$ accounts for final crack opening width, separation distance, and work of separation (or fracture energy), respectively. Sub-indices *n* and *t* indicate the normal and tangential direction, respectively. The variables m and n are the exponents associated with the initial slope and calculated as $m = \alpha(\alpha-1)\lambda_n{}^2/(1-\alpha\lambda_n{}^2)$ and $n=\beta(\beta-1)\lambda_t{}^2/(1-\beta\lambda_t{}^2)$. The work of separation in normal and tangential directions are defined by $\Gamma_n=-\phi_n(\alpha/m)^m$ and $\Gamma_t=(\beta/n)^n$, respectively. Considering only mode I, as discussed in the previous section, we assumed the tangential and normal parameters to be equal and constant ($\lambda_n=\lambda_t$, $\phi_n=\phi_t$, $\delta_n=\delta_t$, $\alpha=\beta$). Finally, the maximum traction can be calculated using Equation 9.[82]

$$\sigma_{max}=\frac{\phi_n}{\delta_n}\alpha\lambda_n(1-\lambda_n)^{\alpha-1}(\frac{\alpha}{m}+1)(\frac{\alpha}{m}\lambda_n+1)^{m-1} \quad (10)$$

Based on Equation 5, $\alpha, \delta,$ and λ are the three main parameters in cohesive traction-separation law under mode-I loading, the effect of each parameter is shown in Figure 2.18a-c. By keeping the values of work of separation constant and keeping a reference case for comparison purposes (shown as a solid black line), we can illustrate the individual contributions of the main parameters to cohesive traction-separation shape. By increasing the values of α, the softening response of the curve changes from convex to a concave shape decreasing the peak traction value (Figure 2.18a). Similarly, when the values of final crack opening width δ increases, both peak

traction and initial slope (stiffness) decrease (Figure 2.18b). However, when we increase the values of initial slope λ, an irregular variation on the peak traction was observed as well as a change from concave to convex in the softening response (Figure 2.18c). The comparison between material characterization using the PPR model and results from the micromechanical model (i.e., average line within a light gray area computed from the maximum and minimum standard deviation from the micromechanical model) is presented in Figure 2.18d. Additionally, the parameters used for the material characterization are presented in Table 2-1.

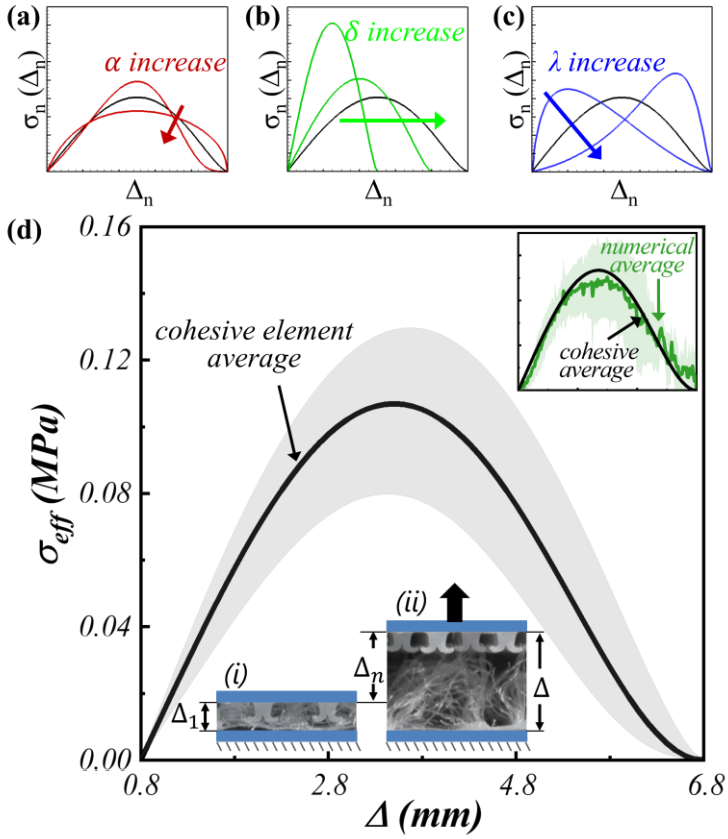

Figure 2.18. Incidence of main parameters on the shape of the traction separation law for a constant fracture energy value in mode I.

(a) shape parameter α, (b) final crack opening parameter δ, and (c) initial slope parameter λ. Black curves sever as reference. (d) Average traction separation curve obtained from the PPR cohesive element (solid black line), with light gray area between the lower and upper bounds computed from the micromechanical model results. In the inset, the comparison between the PPR cohesive element (solid black line) and the average numerical simulations results (green line), the light green area correspond to the maximum and minimum standard deviation of the numerical results.

Based on the results of the micromechanical numerical model (i.e., $\sigma_{eff} - \Delta$ curves from Figure 2.12a), we took the average curve and identified: (*i*) the total separation distance ($\delta_n = 6\ mm$ where all the fibers were fractured); (*ii*) the value for peak stress ($\sigma_{max} = 0.11\ MPa$

for the average case); and (*iii*) the critical opening width ($\delta_{nc} = 3\ mm$ separation at which we reach the peak stress). Subsequently, we calculated the energy required to separate the hook and loop (i.e., work of separation) as the area below the average $\sigma_{eff} - \Delta$ curve obtained from the model, $\phi = 0.37\ N/mm$. Based on the previous parameters, we then obtained the initial slope ($\lambda_n = {}^{\delta_{nc}}/_{\delta_n} = 0.5$). Finally, the parameter α is obtained by fitting the cohesive model to the average $\sigma_{eff} - \Delta$ curves, following the concept depicted in Figure 2.18a, after all the other parameters are plugged into Equations 9 and 10. The lower and upper bounds of all these parameters, which were obtained using the same procedure on the $\sigma_{eff} - \Delta$ curves that have the standard deviation, are also reported in Table 2-1.

Table 2-1. Main cohesive zone parameters

Parameter	α	$\sigma_{(max)}$ (MPa)	Φ (N/mm)	λ (MPa/mm)
Minimum	3.8	0.08	0.26	0.44
Average	3.1	0.11	0.37	0.45
Maximum	2.5	0.13	0.48	0.48

2.3.2.2 Loading and unloading mechanical response of the PPR cohesive model

The behavior of the cohesive model under cyclic loading can be used to capture the irreversible process of the inelastic behavior of the hook-and-loop fastener; more precisely in our case, the plastic deformation and fracture of some of the hooks, and snap through events observed during the sudden release of some of the loops. Figure 2.19 depicts the finite element simulation of the behavior of the cohesive traction-separation law based on the PPR potential under different loading/unloading cycles.[81,83] In the first cycle *AB*, all the loops deform in their elastic regime and therefore the unloading takes place following the same load-displacement path. However, in the cycle *AC*, the load is very close to the required load to break the first loop, and therefore, point *C* denotes the last point where reversible unloading can take place. For a cycle that undergoes larger deformation, (for instance, until point *D*) the unloading process follows a different path, denoting an irreversible process. The area enclosed by the curve connecting the points *ABCD* and back to *A* is the energy that has been dissipated by the irreversible process previously described as the

inelastic mechanical response of the loops, fracture and instabilities related to the release of elastic energy.

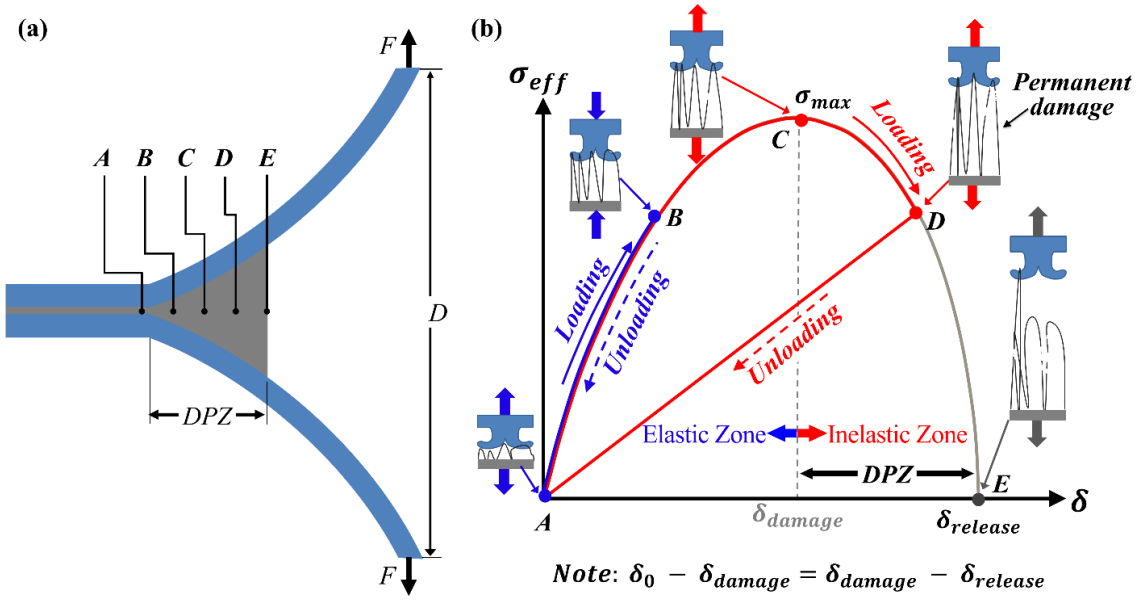

Figure 2.19. Loading-unloading behavior of PPR cohesive model.
(a) Schematic representation of the DCB with the location of hook-and-loop cohesive element during deformation. (b) Loading and unloading path followed by the hook-and-loop cohesive element under tensile loading conditions.

2.3.2.3 Results of the macromechanical model

A total of five DCB specimens comprising Nylon strips as beams with hooks and loops tapes were prepared and tested under quasi-static conditions, as shown in Figure 2.20. The Nylon beams dimensions are 250 mm (length) × 25.4 mm (width) × 2 mm (thickness). The hooks and loops tapes were bonded to the beams using Instant-Bonding Adhesive Loctite® and were left to dried at room temperature for 24 hours before testing. To avoid delamination between the tapes and Nylon strips, the surfaces of the tapes and Nylon strip were hand-sanded prior to bonding in order to increase adherence. The tapes (both hooks and loops) cover the entire width of the sample and have a length of 200 mm, leaving an initial crack of a = 50 mm. The total thickness of the fastener (including both hooks and loops tapes under attachment) is equal to 0.8 mm. Before testing, the two strips were attached by applying a relative shear movement to achieve a consistent engagement, similar to the process used in Section 2.3.1.10. Subsequently, the sample was tested using a universal tensile testing machine (MTS Insight 10) with a load cell of 100 N by applying a displacement rate equal of 3mm/min at the ends of the upper beam as shown in Figure 2.20a. The

measured force *F* and mouth opening *D* are plotted in Figure 2.20b. The blue curve and light blue region denote the average, lower and upper bounds.

Similarly, a 2D finite element model of the DCB (with the same dimensions used in the experiments) was developed using ABAQUS. The individual beams were modeled as elastic materials, assuming Young's Modulus and Poisson's ratio of Nylon (E_{nylon}= 2.2 GPa and ν_{nylon} = 0.45). The hook-and-loop interface was modeled as a cohesive layer with the average properties reported in Table 2-1. Additional simulations were also done considering the lower and upper bounds reported in Table 2-1. The interface is modeled considering an initial thickness of Δ_1 = 0.8 mm, as explained in Figure 2.18. A comparison between the numerical simulations and the average experimental response is shown in inset in Figure 2.20b. The green curve shows the numerical simulations using the average values from Table 2-1. The light green region denotes the lower and upper bounds. While the variation between peak loads and initial stiffness can be explained in terms of the geometrical variability of the loops and hooks, the general decaying portion of the curve, which represents the typical behavior of the DCB was well captured by our two-scale approach.

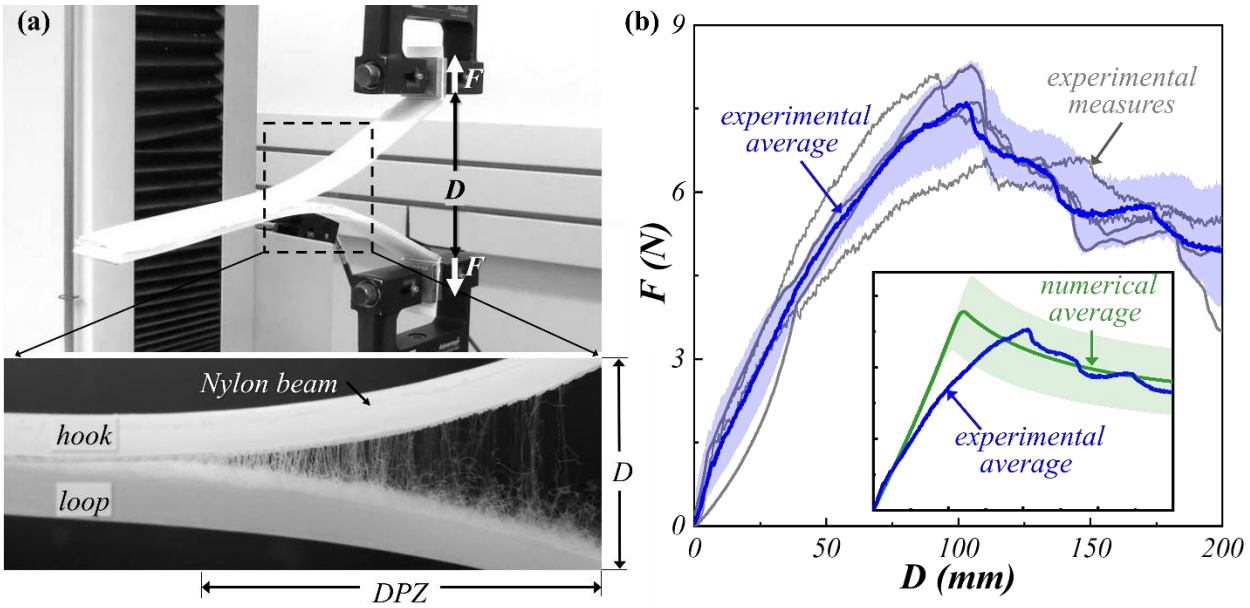

Figure 2.20. Macromechanical experimental test.
(a) details of the experimental setup used to test the DCB specimen applying a force (F) and a displacement (D) to separate the hook-and-loop tapes. (b) Experimental results for the macromechanical test (gray lines) with average curve (blue) within a light blue area computed from the maximum and minimum standard deviation of the experimental results. In the inset, the comparison between the average experimental results (blue line) and the average numerical simulations results (green line) for the macromechanical test, the light green area correspond to the lower and upper bounds given by the standard deviation.

2.4 Discussion

In general, the results presented in Section 2.3 confirm a good agreement between our numerical simulations and the experiments at two specific scales. While the experiments were done to validate the models at the two scales, we demonstrate that the two-scale approach presented here is capable of predicting the behavior of macroscale structures, such as a DCB, using basic mechanical behavior of the individual building blocks at the microscale. On one hand, the high-fidelity micromechanical model demonstrated to be efficient at capturing the proper mechanisms typically found in these types of hooks-and-loops systems. Such mechanisms are mostly related to the inelastic behavior of the loops in terms of elastic-plastic deformation followed by fracture, and the elastic response of the hooks. The micromechanical model is capable of replicating the same type of entanglements observed in the experiments, as shown in Figure 2.10,Figure 2.11, Figure 2.13 and Figure 2.16. As discussed, a relatively small group of hooks and loops selected as the RHLE is sufficient to represent the mechanical behavior inside the detachment process zone. These RHLE not only capture the main averaged properties such as overall stiffness, strength, and work of separation, but also the variability measured in the experiments (see Figure 2.16b). The model is also able to reproduce the main mechanisms that contribute to the initial stiffness and strength. Since the loop variability is directly taken from measurements (as described in Section 2.3.1.3) and explicitly implemented in the micromechanical model with loops of different lengths and cross section areas, it manifests directly in the spread of the initial stiffness and strength of the RHLE. Careful observation of the models, and their corresponding experiments, reveal that most hooks engage three loops in average. Such level of engagement typically leads to fiber fracture as it typically requires 10 to 15 loops to bend a hook. The load required to deform and fracture a loop varies from 0.06 to 0.08 N whereas the force require to bend a single hook is 0.8-0.9N.

It is worth noticing that the experiments reported in Figure 2.16 are merely a checkpoint in our two-scale strategy, as they do not provide any input for our model. Moreover, our numerical results, as reported in Figure 2.12), are then employed as cohesive properties of the DPZ for a larger system, e.g., DCB, which is then validated with another set of experiments as shown in Figure 2.20. The experimental results presented in Section 2.3.2.3 confirm the efficacy of our strategy, demonstrating that one could use these models to predict the behavior of a larger system by simply providing some key geometrical details and basic mechanical properties of the building blocks at the microscale.

While the scope of the present work and example presented in this paper only considers monotonically increasing loads, the mechanical behavior of the hook-and-loop system under cyclic load can also be handled by proposed modeling strategy. The irreversible processes that take place during the detachment process (e.g., plastic deformation and fracture of the loops, snap-through behavior of the sudden release of energy when the loops are either fracture or released from the hooks, friction, etc.) can be considered in the cohesive model by providing a path dependent traction-separation law. The details of such model are included in the Section 2.3.2.2 and will be included in future work considering the reformulated version of the PPR model into the anisotropic Helmholtz form as reported by.[83]

2.5 Conclusions

In this study, we employed the multi-scale approach to understand the mechanical behavior of the hook-and-loop fastener at the micro- and macroscales. The multi-scale approach enabled us to connect the results from the RHLE model (micromechanical model) to a larger scale structures, such as the DCB or peel tests (macromechanical model). We first presented a new computational high-fidelity micromechanical model that includes detailed information of the hooks and loops geometry and basic mechanical behavior. This model captures the general behavior and response of the fastener, such as detachment and pull-out under mode-I loading condition. By establishing a general contact formulation between hooks and loops, we were able to capture both engagement and pull-out process similar to experimental observation. Hook-and-loop fastener are made of polypropylene, and the mechanical behavior of individual loops was characterized by performing pull-out tests on a single and multiple fibers. Based on the experiments, the fibers behave elastoplastic while the hooks remained elastic during the tests. To increase the accuracy of this model, we developed a loop mesh generator code to account for the statistical variation in geometry, volume fraction , diameter, and length of an individual fiber. The loop generator code enabled us to capture the statistical variations that we observed the loops fibrous tape.

The computational domain (RHLE) represents the detachment zone process (DPZ) in the micromechanical model and the DPZ is defined as a new emerging length scale in the macromechanical model. The relationship between RHLE size and DPZ length plays an important role in multiscale modeling. During the analysis, we selected the size of the RHLE much smaller in comparison to the DPZ to satisfy the uniform field conditions in the applied displacement-

traction field and, as a result, represent the mechanical behavior inside the DPZ in macro-scale. Additionally, the entire detachment process at the macroscale model was analyzed using a unique effective traction-separation law obtained directly as the output of RHLE model. The comparison between FE results and experiments of both the RHLE model (micro-scale) and DCB test (macro-scale) shows a good consistency between the results and validated the idea of using the two-sale approach in modeling the hook-and-loop fastener at different scales.

Finally, we successfully developed the multi-scale to predict the mechanical performance of hook-and-loop fastener under mode-I loading conditions. This method could also be extended for various loading conditions scenarios (i.e., mode II, multiaxial loading). The results from computational multi-scale models provide us with new insight through the mechanics of the fastener and significantly decrease the design and production cost by avoiding unnecessary production and experimental testing.

3 BIOINSPIRED FABRICATION OF RECONFIGURABLE ELASTOMERIC CEMENTITIOUS STRUCTURES USING SELF-HEALING MECHANICAL ADHESIVES

Motivation and rationale: Modern construction technologies are in high demand of new highly customizable and easy-to-assemble structural materials with enhanced mechanical performance and the capability to self-repair autonomously. This article describes the simple and cost-effective manufacturing of Self-Healing Elastomeric/Cementitious/Mechanical Adhesive Structures (SECMAS). SECMAS are comprised of cementitious bricks joined by mechanical adhesive interfaces and organized in nacre-inspired, brick-and-mortar structures. This scalable staggered design provides SECMAS with the capability to concentrate the formation and propagation of cracks along the mechanical adhesive interfaces, which efficiently distribute loading forces and accommodate deformation. The periodic distribution of elastomeric reinforcing layers inside the SECMAS facilitates its elastic self-recovery after severe deformation, restoring the interlocking of the mechanical adhesive interfaces and enabling SECMAS to autonomously recover their original mechanical properties at room temperature. Moreover, the rapid recovery of the mechanical adhesive interfaces enables repeated self-healing under cycling bidirectional loading forces. The modular structure of SECMAS and their easy-to-assemble and easy-to-disassemble mechanical adhesive interfaces facilitates the rapid exchange of damaged components for new ones, enlarging service life. Furthermore, the simple and scalable design rules derived for the construction of SECMAS facilitate their rapid reconfiguration into a variety of self-repairing structural elements, promoting sustainable construction.

3.1 Introduction

This chapter presents Self-Healing Elastomeric/Cementitious/Mechanical Adhesive Structures (SECMAS), nacre-inspired hybrid structures capable to be easily reconfigured into a variety of designs. SECMAS are comprised of regularly staggered cementitious bricks (99% in mass), joined by mechanical adhesive (0.2% in mass), and reinforced by elastomeric layers (0.8% in mass). The structure of SECMAS concentrates crack formation and propagation

along the mechanical adhesive interfaces, which rapidly self-repair after the load disappears thanks to the elastic recovery of the elastomeric layers. SECMAS can be easily and rapidly assembled and disassembled using a scalable staggered layout that enables the rapid exchange of damaged bricks for new ones. Moreover, SECMAS self-repair repeatedly and autonomously at room temperature, completely recovering their strength and toughness after loads inducing severe cyclic bidirectional deformation ($\varepsilon_f = 0.21$). We demonstrate that SECMAS exhibit flexural and compression toughness values 50 and 12 times greater than their monolithic counterparts, respectively, and are able to remain functional after failure. When compared with other cementitious/polymeric self-healing composites,[84,85] SECMAS are assembled structures capable of enduring multiple large deformations cycles by exploiting the elastic recovery of their elastomeric layers to repair the mechanical adhesive interfaces that concentrate crack formation. We expect SECMAS to serve as an attractive strategy for the development of resilient self-repairing structures shed light on the design of new deployable, convertible, and temporary constructions capable to meet the rapidly increasing modern demands.[86]

3.2 Nacre Inspired Design of SECMAS

Nacre exhibits an organic-inorganic brick-and-mortar structure (Figure 3.1a) that provides this biomaterial with outstanding toughness and self-healing properties.[63] External forces are efficiently distributed across the organic adhesive interfaces (5 vol%) serving as the mortar for the aragonite platelets (95 vol%) in nacre. These protein-based adhesive interfaces joining aragonite platelets unfold into biopolymer fibrils (Figure 3.1b, c) upon elongation but can restore their folded configuration in the presence of moisture, providing self-healing properties to nacre.[61] Inspired by nacre, SECMAS brick-and-mortar structure is comprised of staggered cementitious bricks (99% in mass), bonded by mechanical adhesive (0.2% in mass), and reinforced by elastomeric layers (0.8% in mass), Figure 3.1d. The mechanical adhesive interfaces of SECMAS comprise arrays of polymeric hook and loops fasteners (Figure 3.1e). Upon contact, the hooks in one side of the interface engage and get entangled with the loop on the other side, creating a strong mechanical interlocking across the interface. Under increasing external loads (Figure 3.1f), the hook-and-loop fasteners in the interface stretch first and then detach, maintaining their capability to restore their attachment when there are brought into contact again.

3.3 Experimental Details

3.3.1 Fabrication of SECMAS

Cement bricks were fabricated by casting Portland Cement CEM-I (TXI Industries Inc., chemical composition in Table 3-1) with water/cement ratio of 0.42 in 10 mm x 28 mm x 50 mm silicone molds. The molds were vibrated for 45 s to help the paste settle and consolidate. The molds were hardened at 23ºC and 90% relative humidity for 24 h. After unmolding, the cement bricks were submerged in water at 45ºC for 7 days for maturation. Prior to assembly the SECMAS, cement bricks were removed from the water bath and dried at 45ºC for 6h. Hook-and-loop mechanical adhesive (3/4-US-41FT; JIHO Inc.) was attached to each of the cement bricks using a cyanoacrylate adhesive gel (Loctite 409; Henkel Ltd.) so that the hooks cover the bottom and one side of the brick and the loops cover the top and the opposite side of the brick. Hook-and-loop covered bricks were attached to each other following a staggered brick-and-mortar pattern. The elastomeric layers of the SECMAS were fabricated using a two-component platinum-catalyzed silicone elastomer, produced by Smooth On, Inc. and commercially known as Ecoflex 00-30. This elastomer has excellent elongation capabilities (elongation at break, $\varepsilon_{frac} \sim 600\%$), a tensile strength, $\sigma_T = 1.38$ MPa, and an elastic modulus, E = 125 KPa.[87] The fabrication process of the elastomeric layers followed a two-step process: First, the inter-brick space of a single layer of bricks assembled over a dense loop casting surface was filled with Ecoflex 00-30. Second, after curing the elastomer at room temperature for 2 h, the dense loop mechanical adhesive surface used to prevent the penetration of the elastomer to the bottom surface of the bricks was removed.

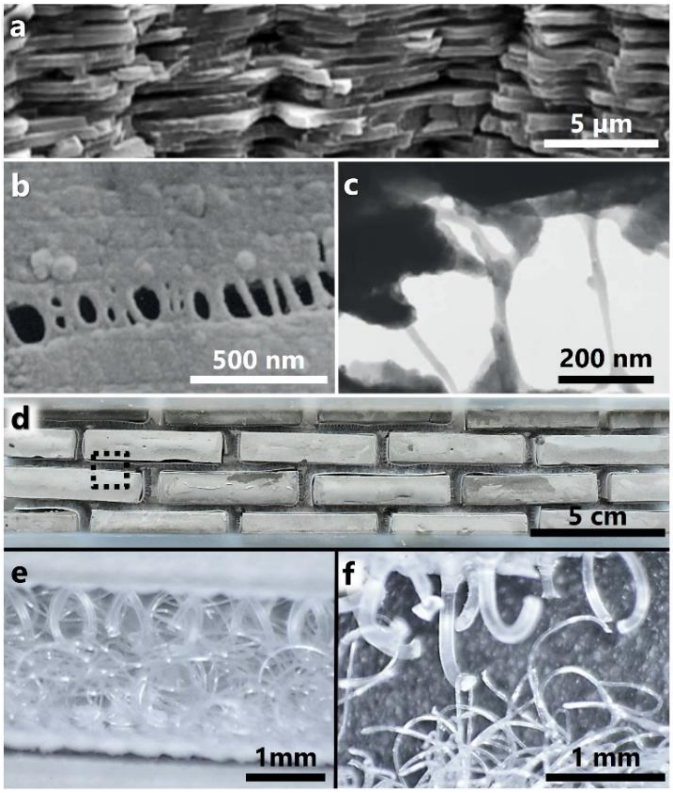

Figure 3.1. Nacre-inspired design of SECMAS.
(a) Brick-and-mortar structure of nacre comprising stiff ~500-nm-thick aragonite platelets bonded by soft and elastic biopolymers. (b) The application of a tensile force induces the delamination of two aragonite platelets, showing their protein adhesive interfaces.[61] (c) Transmission electron microscope image of the adhesive biopolymer fibrils bonding two aragonite platelets in nacre.[63] (d) Nacre-inspired design of SECMAS composed of brittle cement bricks assembled in a brick-and-mortar pattern, joined by mechanical adhesive interfaces, and reinforced with elastomeric layers (at the top and the bottom). (e) Optical image from the area highlighted in (d), showing the mechanical adhesive interface between two cement bricks in a SECMAS. (f) Stretching of the hook-and-loop mechanical adhesive interface between two cement bricks upon tensile forces.

3.3.2 Mechanical Characterization of SECMAS Constituents

SECMAS benefit from the synergistic collaboration of each of its constituents to exhibit high toughness and self-repairing properties (Figure 3.2a). The staggered bricks in SECMAS have high compression strength (~90 MPa)[88] but exhibit a brittle behavior which impede them to sustain deformations larger than 1.8% flexural strain (Figure 3.2b and Figure 3.3). Under external loads, the stretching and detaching of the hook-and-loop mechanical adhesive interfaces exhibit a characteristic stress-strain "saw-tooth" response similar to nacre.[54] where the peaks correspond to hook-and-loop detachment events. The continuous detachment of the hook-and-loop bonds across the mechanical adhesive interface efficiently dissipate tensile and shear stresses applied to the SECMAS (Figure 3.2c, d, and Figure 3.3). Note that, due to the direction of staggering and the

different mechanical properties of the mechanical adhesive interfaces under pure shear and pure tension forces (Figure 3.2c, d) make SECMAS to exhibit strong mechanical anisotropy along orthogonal directions. These mechanical adhesive interfaces, however, efficiently concentrate deformation and crack formation/propagation along the interfaces of SECMAS preserving the integrity of the cement bricks. To provide SECMAS with the capability to restore the attachment between separated mechanical adhesive interfaces, we reinforce its brick-and-mortar structure by introducing elastomeric Ecoflex layers between every four rows of bricks (Figure 3.2a, e). After the dissipation of a deforming load, the elastic recovery of SECMAS brings back into contact the separated mechanicals adhesive interfaces, restoring the binding between their hooks-and-loops.

Tensile, compression, and three-point bending tests were performed in a universal testing machine (MTS ESM1500; Mark-10 Corp.) equipped with a 1 kN load cell (model MR01-1000). To characterize the tensile properties of the elastomer used, dogbone-shaped Ecoflex 00-30 samples were tested according to ASTM D412-16 at a crosshead speed of 3 mm/min. Compression tests were performed according to ASTM D575-91 at a crosshead speed of 3 mm/min. Three-point bending tests were performed according to ASTM D7264-15 at a crosshead speed of 3 mm/min. The adhesion of 19 mm x 40 mm hook-and-loop surfaces was characterized at pure tension and pure shear according to ASTM D4541-17 and D5169-98 at a crosshead speed of 3 mm/min.

3.3.2.1 Mechanical Adhesive

The performance of the mechanical adhesive under pure tension and shear was characterized by attaching a 19 mm x 40 mm hook-and-loop surfaces to opposite faces of 3D printed samples (Figure 3.3a, b). The two samples were first aligned together and pressed against each other. Then, the samples were mounted in a universal tensile testing machine (MTS ESM1500; Mark-10 Corp.) with a 1 kN load cell (model MR01-1000) and pulled at a crosshead speed of 3 mm/min to guarantee quasi-static equilibrium, which allowed us to neglect viscoelastic effects.

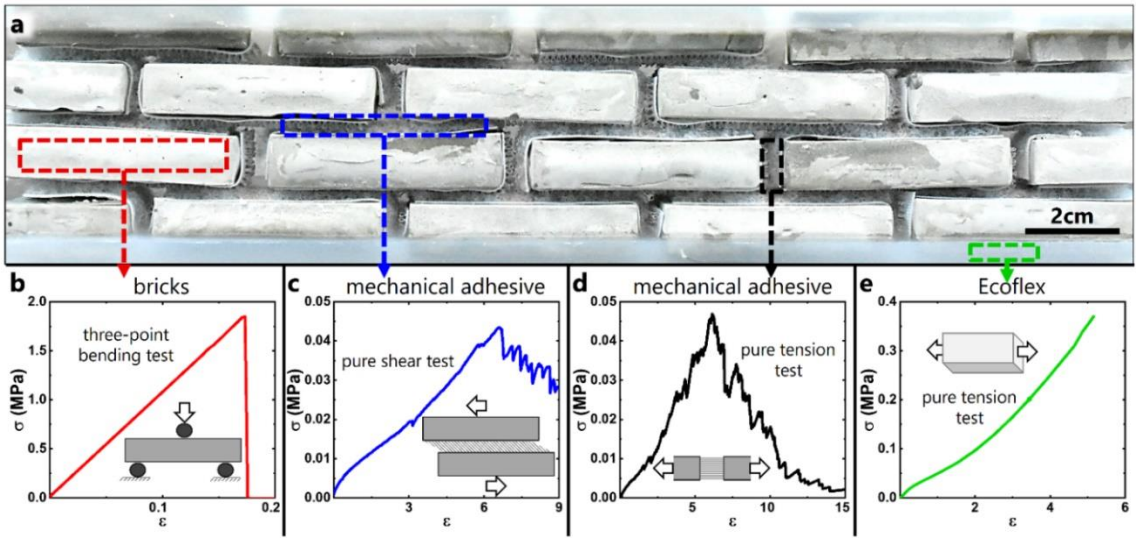

Figure 3.2. Mechanical properties of the constituents of SECMAS.
(a) SECMAS beam with elastomeric layers at the top and the bottom. (b) Flexural behavior of the cement bricks during a three-point bending test with 40 mm span length. (c, d) Performance of the mechanical adhesive interface during a pure shear test (c) and a pure tension test (d). (e) Stress-strain response of Ecoflex 00-30 under uniaxial tension.

3.3.2.2 Bricks

To characterize the mechanical performance of the bricks used in SECMAS, I placed the bricks on two steel supports and performed a three-point bending test using a loading pin moving at a crosshead speed of 3 mm/min, midway between the supports (Figure 3.3c). The span-length between supports was 40 mm.

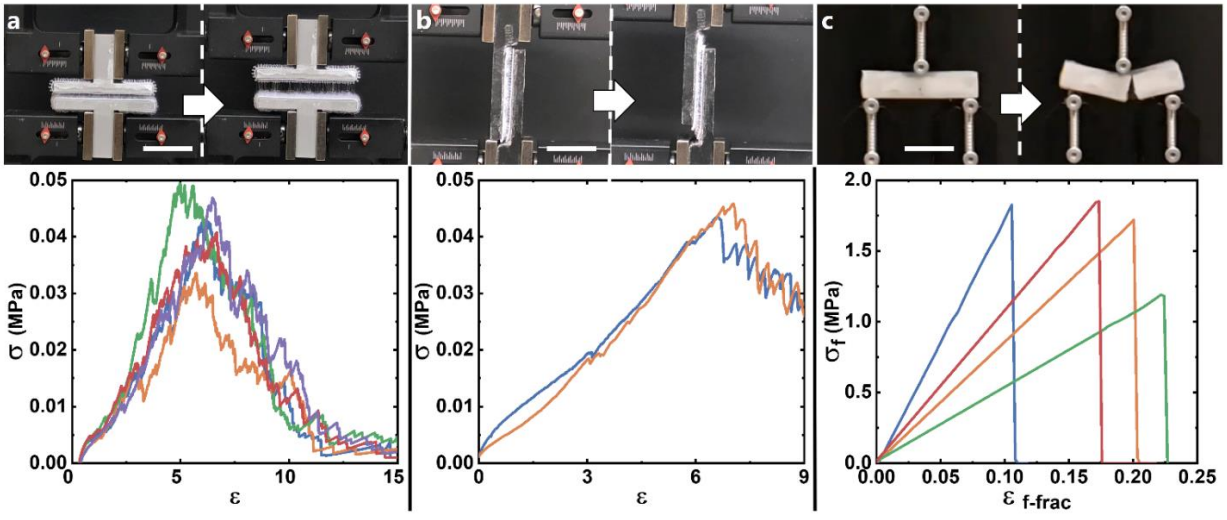

Figure 3.3. Mechanical characterization of SECMAS constituents.
Mechanical adhesive interface in pure traction (a) and pure shear (b). c) Cementitious bricks under three-point bending loads. All scale bars are 2 cm.

Table 3-1. Chemical composition and phase compounds for Portland cement – Type I., in compliance with the ASTM C150, AASHTO M85, and CSA-3001_GU specifications.

Chemical Data	**(%)**
Silicon Dioxide (SiO_2)	19.54
Aluminum Oxide (Al_2O_3)	5.26
Ferric Oxide (Fe_2O_3)	2.71
Calcium Oxide (CaO)	63.49
Magnesium Oxide (MgO)	2.18
Sulfur Trioxide (SO_3)	3.12
Loss on Ignition	2.85
Insoluble Residue	0.39
Carbon Dioxide (CO_2) in Cement	1.67
Limestone	3.94
Calcium Carbonate ($CaCO_3$) in Limestone	96.7
Phase Compounds	**(%)**
Tricalcium Silicate (C_3S)	59.5
Dicalcium Silicate (C_2S)	9.0
Tricalcium Aluminate (C_3A)	9.0
Tetracalcium Aluminoferrite (C_4AF)	7.9
Sodium Oxide (Na_2O) Equivalent	0.62
Free Calcium Oxide (CaO)	1.05

3.3.2.3 Elastomeric Layers

The elastomeric layers of the SECMAS were fabricated using a two-component platinum-catalyzed silicone elastomer called Ecoflex 00-30 (Smooth On, Inc.). After mixing the two components of Ecoflex 00-30 in liquid form at a 1:1 weight ratio, the prepolymer cures into a solid elastomer according to a hydrosilylation curing mechanism. This curing process is based on the addition of Si-H bonds via unsaturated C=C, C−O, and C=N bonds in presence of a platinum-based Karsted catalyst.[89] The performance of the silicone elastomer used to fabricate the elastomeric layers was characterized by placing dogbone-shaped Ecoflex 00-30 samples in a

universal tensile testing machine (MTS ESM1500; Mark-10 Corp.) with a 1 kN load cell (model MR01-1000) and pulled at a crosshead speed of 3 mm/min according to ASTM D412 16 to guarantee quasi-static equilibrium, which allowed us to neglect viscoelastic effects. A representative result from these experiments is displayed in Figure 3.4.

3.3.2.4 Ogden model describing the hyperelastic behavior of the elastomeric layers in SECMAS

The Ogden model has been used to describe the hyperelastic behavior of a variety of highly stretchable elastomers.[90]

$$U = \sum_{i=1}^{N} \frac{2\mu_i}{\alpha_i^2}\left(\bar{\lambda}_1^{\alpha_i} + \bar{\lambda}_2^{\alpha_i} + \bar{\lambda}_3^{\alpha_i} - 3\right) + \sum_{i=1}^{N} \frac{1}{D_i}\left(J^{el} - 1\right)^{2i} \quad (11)$$

This model describes the volumetric response of a material to stretching by expressing the strain energy potential (U) as a function of the principal stretches (λ_i), the shear modulus (μ_i), and the volumetric material parameters (D_i). Note that α_i, μ_i, and D_i are all temperature-dependent material parameters that can be obtained by fitting the Ogden model using the experimental results obtained during the tensile testing of Ecoflex 00-30 (Figure 3.4).

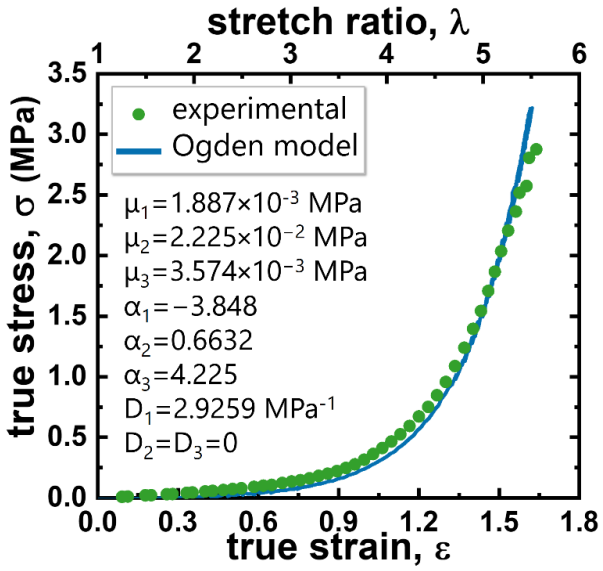

Figure 3.4. Mechanical characterization of SECMAS elastomeric layers.
Experimental true stress vs strain curves of Ecoflex 00-30 obtained during a uniaxial tensile test (green dots) fitted using a three-term Ogden model (solid blue line).

3.3.3 Finite Element Model of the Mechanical Performance of SECMAS

Simulations modeling the behavior of SECMAS were performed using a commercial finite element solver (Abaqus/CAE 6.13-1; Simulia Corp.). The experimental elastomeric behavior of Ecoflex 0030 (ρ = 1.06 g/cm^3) was approximated using a hyperelastic three-term Ogden model [90,91] with the following parameters: μ = 1.887×10^3 MPa, $\mu 2$ = 2.225×10^{-2} MPa, $\mu 3$ = 3.574×10^{-3} MPa, $\alpha 1$ = −3.848, $\alpha 2$ = 0.6632, $\alpha 3$ = 4.225, D1 = 2.9259 MPa^{-1}, D2 = D3 = 0 (Figure 3.4). Cement bricks were simulated using an elastic model with a density ρ = 1.8 g/cm^3, Young's modulus E = 10 MPa, and a Poisson's ratio ν = 0.49. The mechanical adhesive interfaces were approximated by a bilinear traction-separation law using a nominal stress of 0.045 MPa and a fracture energy of 0.27 N/mm, ρ = 0.9 g/cm^3, and E = 0.033 MPa. The interfaces between the mechanical adhesive and their corresponding cement bricks were connected using a surface-based tie constrain formulation.[80] Three-point bending steel supports and loading pin were simulated using an elastic model with ρ = 8.05 g/cm^3, E = 200 GPa, and ν = 0.30. Elastomeric layers and cement bricks were discretized using solid first order hexahedral C3D8 elements, while the mechanical adhesive was discretized with linear tridimensional cohesive COH3D8 elements. Three-point bending supports and loading pin were discretized using solid tetrahedral C3D4 elements. The supports were restricted from motion and rotation in all directions, while the top loading pin was constraint to move vertically at a loading speed of 3 mm/min.

To replicate the experimental conditions of the three-point bending tests, the SECMAS beam is placed on top of the two steel supports (span length 150 mm) and loaded by a loading pin (Figure 3.5). The contact between the steel supports and the elastomeric layer in the SECMAS is defined using a master/slave condition where the upper surfaces of the supports are the "master" and the elastic layer is the "slave". The rest of the contacts in the SECMAS (brick mechanical adhesive interfaces) were defined using general contact conditions. Restriction of interpenetration and frictionless conditions were imposed in the model.

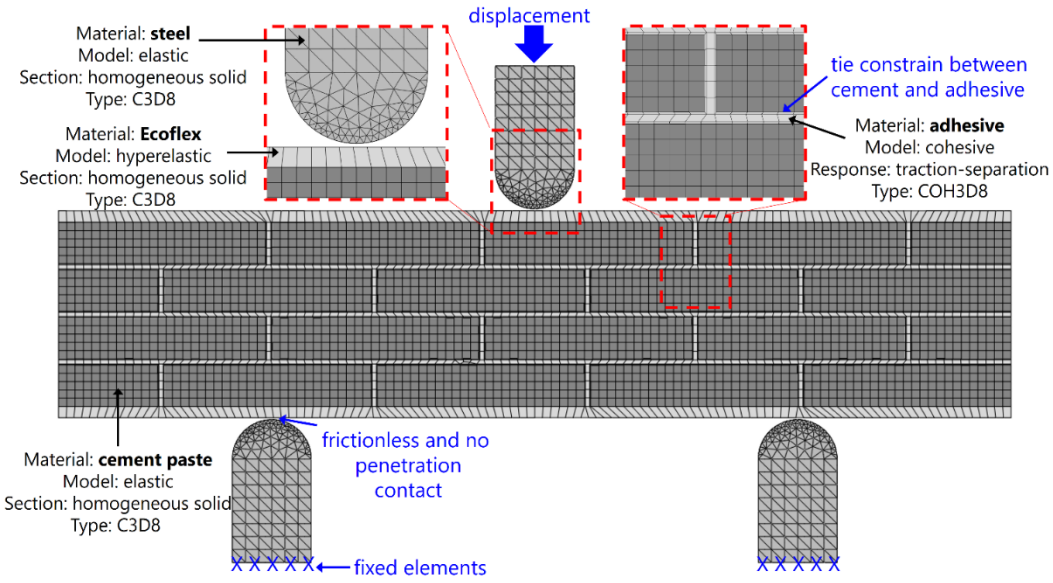

Figure 3.5. Finite element modeling of a SECMAS beam using Abaqus/CAE software.

3.4 Results and Discussion

3.4.1 Mechanical Performance of SECMAS

Figure 3.6 shows the comparison between the mechanical performance of SECMAS and their monolithic cementitious counterpart while undergoing three-point bending and compression tests. Upon flexural deformation, a monolithic cementitious beam exhibit higher Young's modulus (~700 MPa) than a SECMAS of the same dimensions. The brittle behavior of cementitious materials limits their capability to accommodate deformation to a mere flexural strain at fracture $\varepsilon_{f\text{-}frac} = 0.0019$ (Figure 3.6a). After reaching $\varepsilon_{f\text{-}frac}$, cementitious materials develop cracks that rapidly propagate through their structure,[92] leading to catastrophic failure (Figure 3.6a, bottom). The reduced maximum deformation ($\varepsilon_{f\text{-}frac} = 0.0019$) of monolithic cementitious counterparts hinders their toughness ($U_{flex} = 1.3$ KJ/m^3) and limits the tolerance of conventional brick walls joined by brittle mortar interfaces to cycling loading forces of large amplitude, such as earthquakes.[93] On the other hand, SECMAS, while exhibiting lower Young's modulus that their monolithic cementitious counterparts, exhibit flexural toughness values 50 times greater ($U_{flex} = 65$ KJ/m^3) than their monolithic counterparts, since the mechanical adhesive interfaces joining the cementitious bricks efficiently dissipate tensile and shear forces (Figure 3.6b). SECMAS exhibit a remarkable 39.4% maximum flexural strain (strain at which the first brick in

the SECMAS breaks). When subjected to compressive forces, the mechanical adhesive interfaces accommodate deformation and distribute the pressure over the surface of the bricks, retarding crack formation (Figure 3.6c, d), imparting the reconfigurable bricks in SECMAS with a compression toughness 12 times greater (U_{comp} = 78 KJ/m^3) than their cementitious counterparts. Furthermore, even after some bricks fracture, the mechanical adhesive interfaces in SECMAS maintain the cohesion between bricks in the structure, avoiding catastrophic failure and enabling the further dissipation of applied loads.

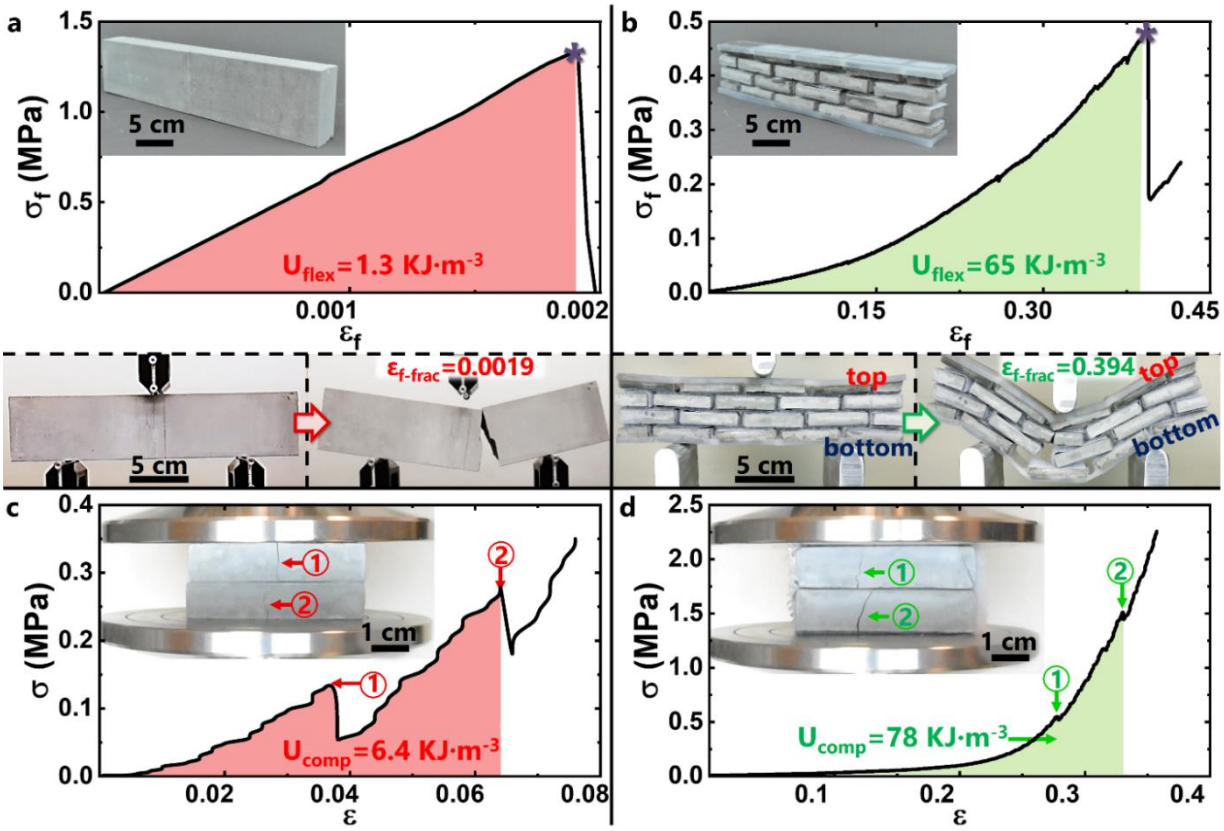

Figure 3.6. **Mechanical performance of SECMAS compared with its monolithic cementitious counterpart.** (a) Dependence of the pure bending (flexural) stress induced on a 53 x 28 x 235 mm monolithic cement block as a function of its vertical flexural strain at the center. This cement block experiences catastrophic failure (marked with an asterisk) after a flexural strain εf-frac = 0.0019. The red colored area under the stress-strain curve prior to fracture corresponds to the flexural toughness of the cement block. (b) Flexural stress-strain response of a beam-like SECMAS with the same dimensions of the cement block shown in (a). The flexural strain at which the first brick in the SECMAS breaks is εf-frac = 0.3940. The flexural toughness of the SECMAS is calculated as the area below the flexural stress-strain curve (green colored) until the first brick in its structure fails (event marked with an asterisk). After the fracture of the first brick, the mechanical interfaces between the bricks continue accommodating the deformation and distributing the bending load, preventing the sudden catastrophic failure of the SECMAS. (c) Dependence of the compressive stress induced on two 10 x 28 x 50 mm overlapping cement bricks (no mechanical adhesive interface) as a function of its vertical strain. The fracture of the top brick (point 1) induces the accumulation of the load across the crack, which leads to the fracture of the bottom brick (point 2). (d) Compressive stress-strain response two overlapping SECMAS bricks with the same dimensions of the cement bricks shown in (c). The incorporation of compliant mechanical adhesive interfaces enables the distribution of compression loads over their surface, delaying crack formation and enhancing compression toughness (Movie 1).

3.4.2 Autonomous Self-healing of SECMAS at Room Temperature

Even after enduring loads inducing large deformations, SECMAS can rapidly, repeatedly, and autonomously recover their mechanical performance at room temperature thanks to the facility with which their mechanical adhesive interfaces can restore their bonds upon contact. This self-healing capability is illustrated in Figure 3.7, which shows the recovery of the mechanical properties of a SECMAS beam after the application of bidirectional cycling loads inducing flexural strains up to 20%. While bidirectional cycling loads inducing such flexural strains often cause the cracking of cement structures, these loads are not sufficient are not sufficient to induce the cracking of the cement SECMAS bricks. During odd loading cycles (1, 3...), a bending force is applied at the top surface of the SECMAS, in a direction perpendicular to its elastomeric layers (Figure 3.7a). The continuous bending of the SECMAS induces the accumulation of compressive forces at the mechanical adhesive interfaces closer to the loading pin, reducing the distance between the hook-and-loop fasteners and enhancing their attachment. Simultaneously, tensile forces are generated on the opposite side of the bending SECMAS, leading to the dissipation of energy through the detachment of the mechanical adhesive interfaces on that region. When the bending load is removed, the elastic recovery of the SECMAS induced by the elastomeric layers embedded in its structure brings the mechanical adhesive interfaces back into contact, restoring the binding of their hook-and-loop fasteners (Figure 3.7c). The self-healing of SECMAS, however, is limited by the capability of the elastomeric layer to absorb the deformation within its elastic deformation range ($\varepsilon \leq 600\%$, Figure 3.2e). During even loading cycles (2, 4...), the SECMAS beam is loaded in the opposite direction (load applied perpendicularly to its bottom surface, Figure 3.7b). This load now compresses the mechanically adhesive interfaces stretched during cycle 1, enhancing their contact and completely restoring their attachment. Similarly, layers previously compressed during cycle 1 are now stretched during cycle 2, dissipating energy. It is important to note that, upon the application of punctual loads, the strength of the SECMAS depends on the location of the load relative to the brick-and-mortar pattern (see differences between cycles 1 and 2, Figure 3.7c). These differences in strength minimize when the load is distributed along the length of the SECMAS, as it often occurs in construction structures.[94]

By comparing the material response of SECMAS during odd or even cycles (Figure 3.7c), we observe that the elastic recovery based self-healing of SECMAS at room temperature efficiently restores their strength and toughness. The capability of SECMAS to efficiently dissipate

energy from external loads through their mechanical adhesive interfaces and to elastically recover provide them with values of flexural strain and toughness higher than several previously reported self-repairing structures[84,85] (Table 3-4). It is important to highlight, that the use of Ecoflex 00-30—a highly stretchable elastomer with a low elastic constant—in SECMAS optimizes their stretchability but limits their elastic recovery force, impeding them to completely recover their initial configuration after one loading/unloading cycle ($\varepsilon f \approx 0.075$, Figure 3.7c). To minimize this permanent deformation in SECMAS, which could in turn limit their serviceability, elastomers less stretchable but with higher elastic constants could be used in their elastomeric layers. However, the capability of the proposed cementitious staggered structures to autonomously regain their mechanical performance after flexural strains up to 20% makes SECMAS a promising structural material to build reconfigurable constructions that might be subjected to cycling loading forces of large amplitude, such as ground-borne vibrations, earthquakes and/or extreme weather conditions.

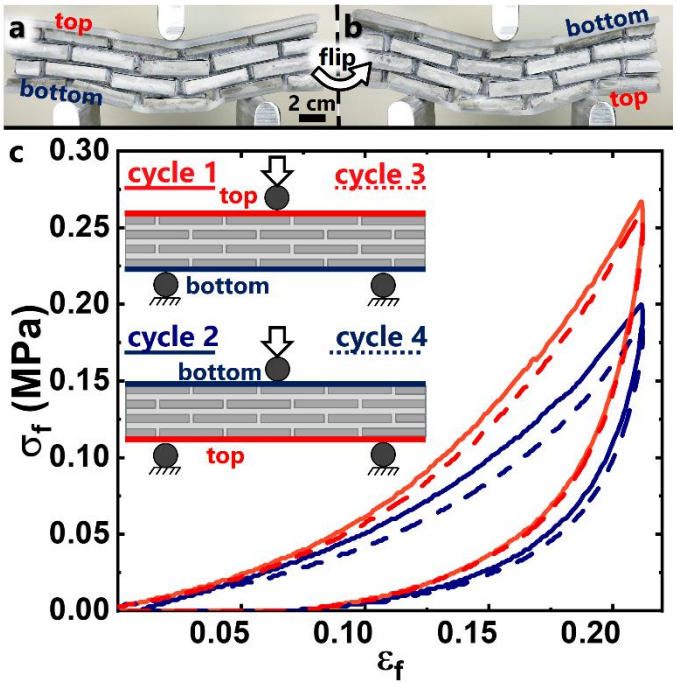

Figure 3.7. Self-healing capability of SECMAS exposed to cycling bidirectional bending loads.
(a, b) Cycling three-point bending tests simulating the effect of a bidirectional bending load on a beam-like SECMAS. The bending force is applied to the top of the SECMAS in cycles 1 and 3 (a) and to the bottom of the SECMAS in cycles 2 and 4 (b). (c) Dependence of the flexural bending stress applied to the SECMAS as a function of the flexural vertical strain at its center. This graph shows the complete autonomous self-healing of the SECMAS at room temperature after withstanding repeated bidirectional bending loads (see Movie 2).

3.4.3 Rapid Exchange of SECMAS

SECMAS, as staggered cementitious bricks joined by mechanical adhesive interfaces, can be rapidly disassembled and re-assembled at room temperature, without requiring curing time. Figure 3.8 demonstrates how, after the fracture of one or several bricks in their structure, the modular design of SECMAS facilitates the rapid exchange of the damaged bricks for new ones, restoring the mechanical performance of the assembled structure. To demonstrate the rapid reparation of SECMAS by exchanging damaged components, we performed three consecutive loading cycles applying a bending force perpendicular to the top surface of a SECMAS beam: During the first cycle, the SECMAS beam experiences a flexural strain of 21%, which the SECMAS can withstand and recover from thanks to the elastomeric layers in its structure. After the SECMAS autonomously recovers its mechanical properties, we applied a second loading cycle, which exposed the SECMAS beam to a flexural strain of 42%. Such flexural strain caused the failure of one of the bricks on the SECMAS (see point III in Figure 3.8c). After the removal of the bending load, the elastomeric layers restored the original shape of the SECMAS beam. The maximum flexural strain that SECMAS are able to endure before their elastomeric layers delaminate from the bricks was 62%. After the second loading cycle, we benefited from the rapid detachment and reattachment of the mechanical adhesive interfaces of the SECMAS to replace the fractured brick for a new one in only 21s (see Movie 3). We tested the mechanical performance of the repaired SECMAS by applying a third cycle replicating the loading conditions of the first cycle. When comparing these first and third loading cycles (red solid and blue dashed lines in Figure 3.8c), we observed the SECMAS regained its original mechanical performance completely after the replacement of the broken component.

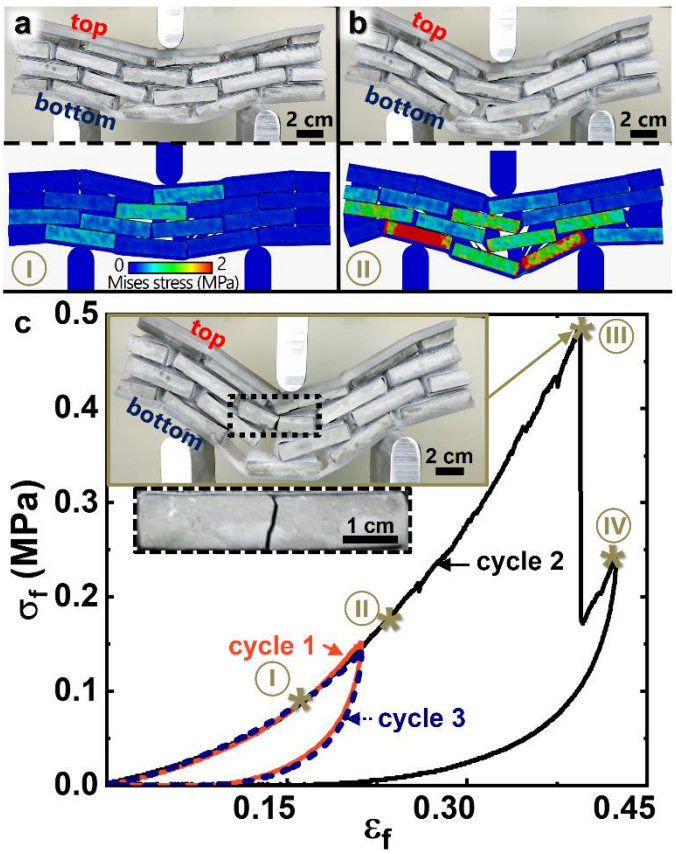

Figure 3.8. Restoring the mechanical performance of SECMAS by rapidly replacing its damaged components.

(a, b) Match between the experimental three-point bending tests and FEA simulations showing the distribution of stress across the SECMAS for a flexural vertical strain of $\varepsilon f = 0.17$ at point I (a) and $\varepsilon f = 0.24$ at point II (b). (c) Three-point bending tests for three different loading cycles. During cycle 1, the SECMAS is bent until it reaches $\varepsilon f = 0.21$, crossing point I (panel a). During cycle 2, the SECMAS is bent until the first fracture event occurs in one of its bricks at $\varepsilon f\text{-frac} = 0.394$ (point III), after crossing points I and II (panels a, b). Even after the mechanical failure of one of their bricks, SECMAS remain capable of bearing load ($\varepsilon f = 0.42$ at point IV). After the bending load is removed and the broken brick is replaced by a new one (see Movie 3), a three-point bending cycle 3 is performed at the loading conditions of cycle 1, demonstrating the complete recovery of the mechanical properties of the SECMAS after the replacement of the broken component.

3.4.4 Scalable Design Rules for SECMAS

The mechanical properties of SECMAS beams can be tailored, even after fixing the choice of fabrication materials, by modifying the length (b_L), thickness (b_t), and overlapping (b_o) of its staggered bricks. Based on previous theoretical models for staggered structures across scales,[18] we developed an analytical formulation for SECMAS that enables the rapid determination of the geometry of the bricks required to achieve a desired mechanical performance (Figure 3.9a and Section S3 in the Supplementary Information). This formulation facilitates the understanding of

the effect that the geometry of the bricks has on the mechanical performance (toughness U_{flex}, flexural strain at fracture ε_{f_frac}, maximum strength at fracture σ_{f_max}, and flexural stiffness E_f) of the SECMAS beams. The toughness of a SECMAS beam rapidly decreases when the thickness of its bricks increases, independently of the length of the bricks, due to the increase in the spacing between the horizontal mechanical adhesive interfaces (Figure 3.9a-I). On the other hand, the flexural strain that can be sustained by a SECMAS increases rapidly when the length of the bricks decreases, independently of the thickness of the bricks (Figure 3.9a-II). Both the maximum flexural strength and flexural stiffness of the SECMAS increase with the aspect ratio (b_L/b_t) of the bricks (Figure 3.9a-III, IV). Reducing the overlap (b_o) among bricks reduces the overall mechanical performance of the SECMAS beams (Figure 3.11). Increasing the thickness of the mechanical adhesive interfaces reduces the flexural stiffness of the SECMAS beam (Figure 3.12).

After using Figure 6a to calculate the design parameters of a SECMAS beam, a simple scalable design rule can be applied to the construction of larger SECMAS by simply stacking, in a staggered configuration, SECMAS beams (Figure 3.9b, top). Our analytical formulation can be extended to these SECMAS-based structures, allowing us to determine the relationship between the length (s_L), thickness (s_t), and overlapping (s_o) of the SECMAS beam used as unit cell and the mechanical properties of the resulting assembled structure (Figure 3.9b). The toughness of SECMAS-based structures, constructed by staggering SECMAS beams, decreases with the thickness of the SECMAS beam, as this correlates with the thickness of its bricks (Figure 3.9a, b-I). Similarly, the maximum strain supported by SECMAS-based structures, decreases with the length of the SECMAS beams, as this corresponds to a decrease in the length of the bricks on each SECMAS beam (Figure 3.9a, b-II). As expected, both the maximum flexural strength and flexural stiffness of SECMAS-based structures increase with the aspect ratio of the SECMAS beams (s_L/s_t) as this aspect ratio is proportional to the aspect ratio of the bricks (b_L/b_t), Figure 3.9a, b-III and Figure 3.9a, b-IV. Since SECMAS exhibit higher compression resistances than their monolithic cementitious counterparts (Figure 3.6c, d), we expect that, after properly scaling their design, SECMAS-based walls will serve as structural supports with a similar compression performance as conventional brick and mortar walls.[95]

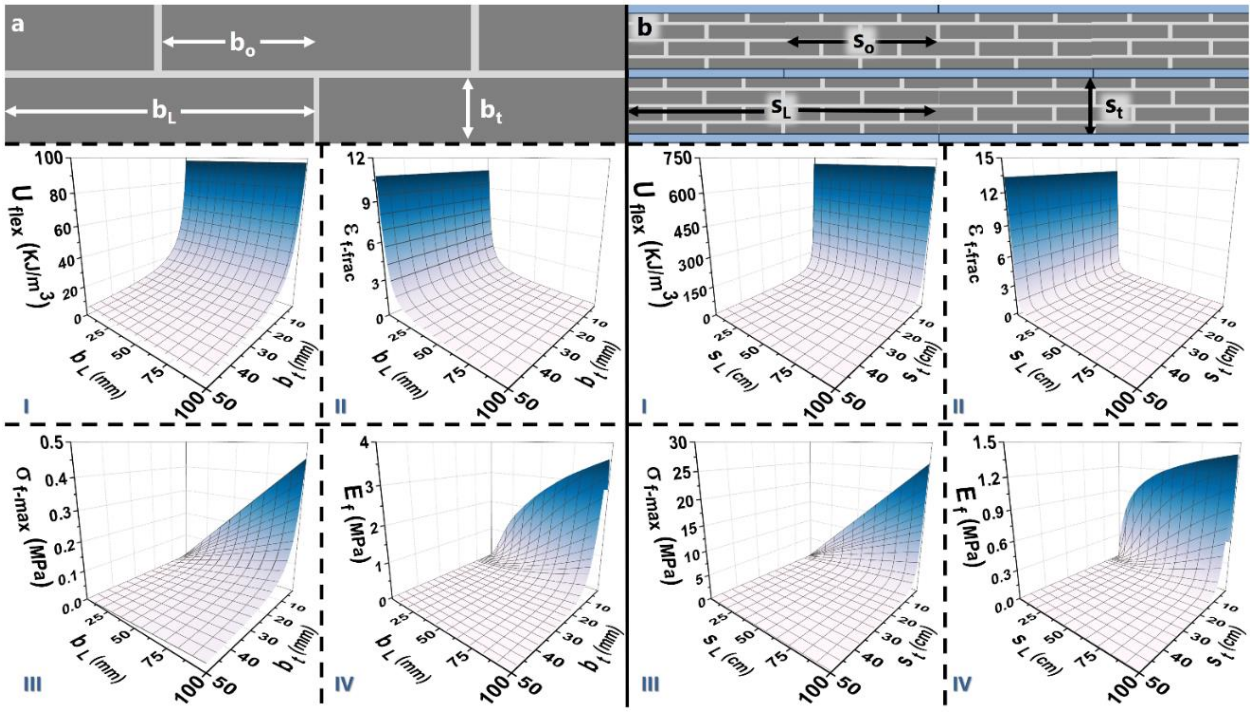

Figure 3.9. Scalable design rules of SECMAS.
(a) Dependence of the mechanical properties of the proposed SECMAS beams (brick overlap, bo=bL/2; as shown in Figure 3.1d and Figure 3.2a) on their geometrical parameters (brick length bL and thickness bt). (b) Dependence of the mechanical properties of a SECMAS-based structure composed of staggered SECMAS beams (beam overlap, so=sL/2) on the geometrical parameters of the SECMAS beam (length sL and thickness st).

3.4.5 SECMAS Analytical Model

I elaborate an analytical model that serves as a guideline for the optimization of SECMAS-like structures at different scales using previous theoretical models for staggered composites across scales.[18,96,97] My analytical formulation predicts the mechanical performance of the SECMAS by inputting the geometrical parameters and material properties of its constituents (Figure 3.10). When the required mechanical performance of the SECMAS is known, this formulation facilitates the rapid selection of constituents that will achieve the desired mechanical behavior. This analytical model assumes that only the top and bottom surface of the bricks are covered by mechanical adhesive interfaces (there is no mechanical adhesive interfaces in vertical junctions among the bricks). As seen in Figure 3.9, Figure 3.11, and Figure 3.12, this model highlights the following two design rules for SECMAS:

(i) The thickness of the bricks should be small to increase the toughness, stiffness and strength of the staggered composite.[98,99]

(ii) The overlap between the bricks should be close to $b_L/2$ to promote strength, and toughness,[61,96,100,101] as shown in Figure 3.12.

Table 3-2 and Table 3-3 summarize the analytical equations used to predict the mechanical behavior of SECMAS by varying the brick thickness (b_t) and brick length (b_L), and the mechanical behavior of SECMAS-based structures by varying the SECMAS beam thickness (s_t) and length (s_L). The parameters marked with an asterisk (*) are required inputs in order to calculate the predicted mechanical behavior of the staggered composite.

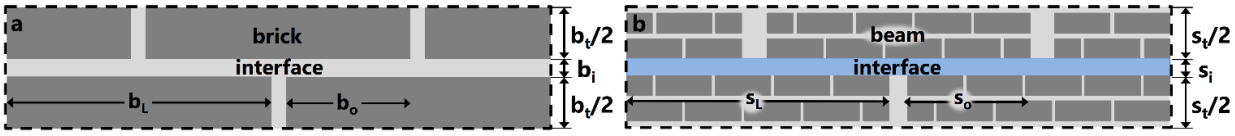

Figure 3.10. Schematics of the geometrical parameters of staggered composites.
(a) SECMAS beam. (b) SECMAS-based structure comprising several staggered SECMAS beams.

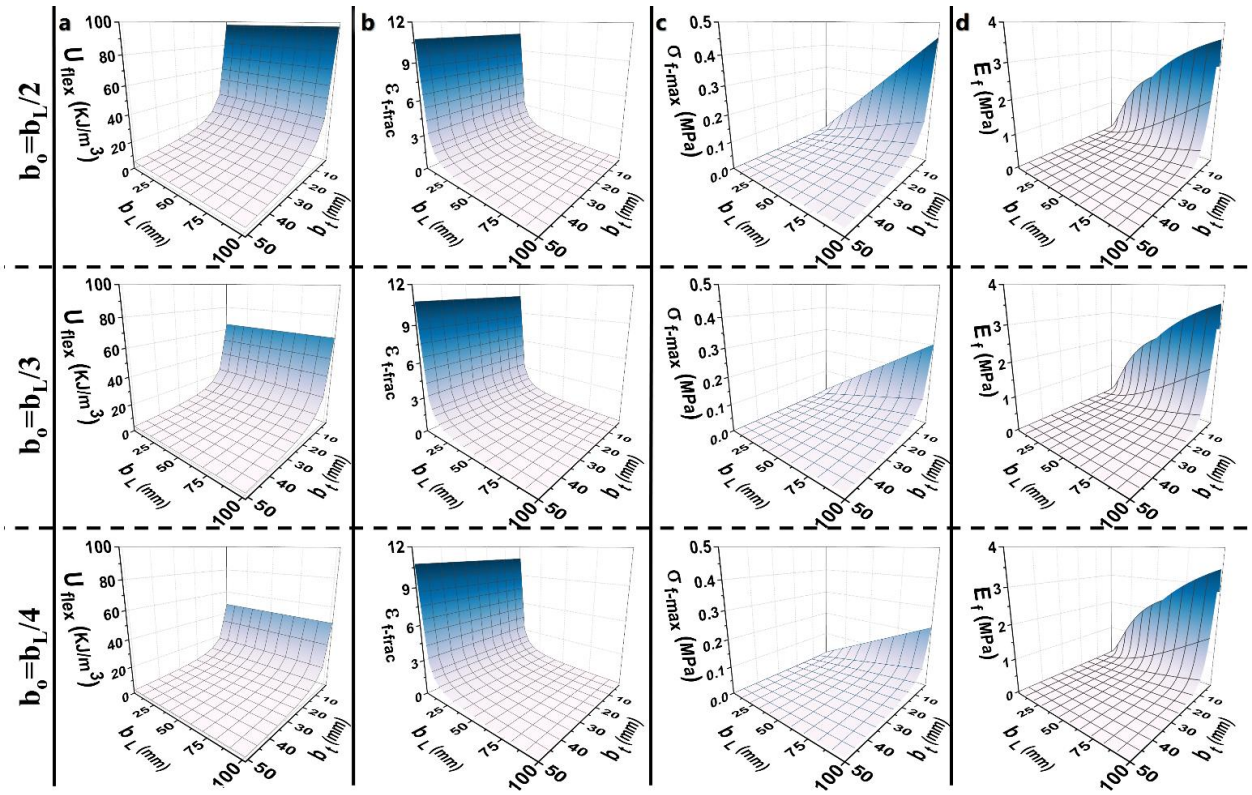

Figure 3.11. Dependence of the mechanical response of a SECMAS beam on the overlap of its bricks.

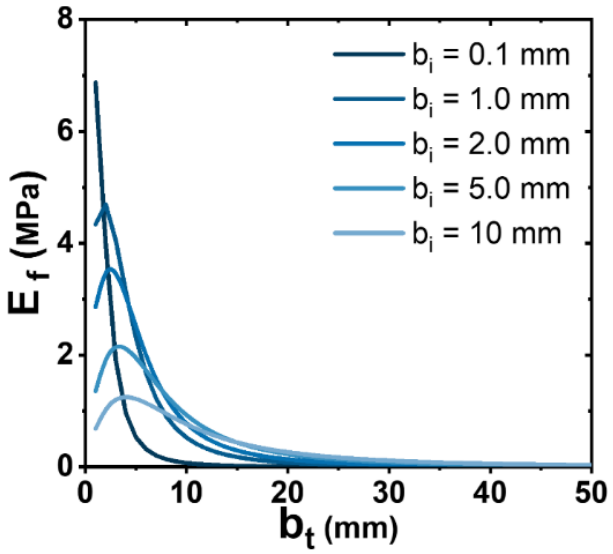

Figure 3.12. Dependence of the flexural stiffness (E_f) of a SECMAS beam on the thickness of the bricks (b_t) for different thicknesses of its mechanical adhesive interfaces (b_i).
Brick length bL=100 mm.

3.4.6 Mechanical Performance of SECMAS Compared to Similar Self-healing Composites.

Table 3-4 and Figure 3.13 summarize the maximum toughness and flexural strains exhibited by previously reported self-healing staggered composites. SECMAS exhibit higher values of flexural strain and toughness than previously reported self-healing composites, opening up an avenue toward the development of a new generation of reconfigurable self-healing structural elements, promoting sustainable construction. It is important to remark that several self-healing composites previously reported[84,85] exhibit a superior mechanical performance when compared with SECMAS; however, their ability to restore their mechanical properties after failure is limited to one cycle, while SECMAS can self-heal multiple times. Additionally, by changing the components of SECMAS it will be possible to tailor the mechanical properties of the resulting hybrid structure. For example, thermoplastic polyurethanes (TPU) could be used as elastic layers, since they can be easily reshaped when the temperature is increased over their glass transition (~80 °C) and their elasticity is re-gained upon cooling at room temperature. The higher strength of TPUs, when compared with silicone elastomers, will lead to hybrid structures with higher stiffness, but less capability to withstand large deformations than SECMAS.

Table 3-2. Analytical equations for SECMAS composite

Geometrical inputs		SECMAS
brick thickness (*)	b_t	10 [mm]
interface thickness (*)	b_i	2 [mm]
brick length (*)	b_L	50 [mm]
brick overlap (*)	b_0	25 [mm]
Composite properties		**SECMAS**
volume fraction	$\phi = {b_t}/{(b_t + b_i)}$	0.833 [-]
aspect ratio brick	$\rho = {b_L}/{b_t}$	5.0 [-]
aspect ratio overlap	$\rho_0 = {b_0}/{b_t}$	2.5 [-]
overlap ratio	$k = {b_0}/{b_L}$	0.5 [-]
Material properties of tablets		**SECMAS**
brick stiffness (*)	E_t	10.756 [MPa]
fracture toughness (*)	K_{IC}	0.165 [MPa√m]
initial crack length (*)	a	0.002 [mm]
geometrical factor	f_0	1.12 [-]
tensile strength	$\sigma_t = {K_{IC}}/{f_0\sqrt{\pi a}}$	1.858 [MPa]
Material properties of interface		**SECMAS**
interface stiffness (*)	E_i	0.0075 [MPa]
interface strength (*)	σ_i	0.047 [MPa]
interface tensile strain failure (*)	ε_i	6.22 [-]
interface shear strength	$\tau_i = \sigma_i$	0.047 [MPa]
interface shear strain	$\gamma_i = \varepsilon_i$	6.22 [-]
interface toughness	$U_i = \sigma_i \varepsilon_i$	292 [KJ/m^3]
Mechanical properties of the composite		**SECMAS**
shear transfer number	$\beta_0 = \rho_0\sqrt{{E_i\phi}/{3E_t(1-\phi)}}$	0.153 [-]
SECMAS stiffness	$E_f = {\phi E_t}/{(1 + \frac{\kappa}{\beta_0}[\frac{1}{\tanh(\beta_0)} + \frac{1}{\tanh(\frac{1-k}{k}\beta_0)}])}$	0.24 [MPa]
SECMAS strength	$\sigma_f = \left({b_0\tau_i}/{(b_t + b_i)}\right)$	0.098 [MPa]
SECMAS strain	$\varepsilon_f = \left({(1-\phi)\gamma_i}/{\phi\rho}\right)$	0.249 [-]
SECMAS toughness	$U_{flex} = \sigma_f \varepsilon_f + U_e$	24.4 [KJ/m^3]

Table 3-3. Analytical equations for SECMAS-based structures

Geometrical inputs		SECMAS' wall
beam thickness (*)	s_t	53 [mm]
interface thickness (*)	s_i	3 [mm]
beam length (*)	s_L	235 [mm]
beam overlap (*)	s_0	117.5 [mm]
Composite properties		**SECMAS' wall**
volume fraction	$\phi = {s_t}/{(s_t + s_i)}$	0.946 [-]
aspect ratio beam	$\rho = {s_L}/{s_t}$	4.43 [-]
aspect ratio overlap	$\rho_0 = {s_0}/{s_t}$	2.22 [-]
overlap ratio	$k = {s_0}/{s_L}$	0.5 [-]
Material properties of beams		**SECMAS' wall**
SECMAS stiffness	E_f	2.04 [MPa]
SECMAS strength	σ_f	0.098 [MPa]
SECMAS strain	ε_f	0.259 [-]
SECMAS toughness	U_{flex}	64.3 [KJ/m^3]
Material properties of interface		**SECMAS' wall**
interface stiffness (*)	$\mathrm{E_i}$	0.072 [MPa]
interface strength (*)	σ_i	0.37 [MPa]
tensile strain failure (*)	ε_i	5.14 [-]
shear strength	$\tau_\mathrm{i} = {\sigma_\mathrm{i}}/{\sqrt{3}}$	0.21 [MPa]
shear strain	$\gamma_\mathrm{i} = \sqrt{3}\varepsilon_\mathrm{i}$	8.90 [-]
energy dissipated	$\mathrm{U_i} = \sigma_\mathrm{i}\varepsilon_\mathrm{i}$	1900 [KJ/m^3]
Mechanical properties of the composite		**SECMAS' wall**
elastic shear transfer number	$\beta_0 = \rho_0 \sqrt{{E_i\phi}/{3E_f(1-\phi)}}$	0.0763 [-]
SECMAS' wall modulus	$E_{f\_wall} = {\phi E_f}/{(1 + \frac{\kappa}{\beta_0}[\frac{1}{\tanh(\beta_0)} + \frac{1}{\tanh(\frac{1-k}{k}\beta_0)}])}$	0.00532 [MPa]
SECMAS' wall strength	$\sigma_{f\_wall} = {s_0\tau_i}/{(s_t + s_i)}$	0.4483 [MPa]
SECMAS' wall strain	$\varepsilon_{f\_wall} = {(1-\phi)\gamma_i}/{\phi\rho}$	0.113 [-]
SECMAS' wall energy	$U_{flex\_wall} = \sigma_{f\_wall}\varepsilon_{f\_wall}$	50.65 [KJ/m^3]

Table 3-4. Comparison between the mechanical properties of SECMAS and those of self-healing staggered composites previously reported.

Staggered self-healing composite	Toughness (KJ/m$^{3)}$	Strain	Healing efficiency (%)
SECMAS	137 66.2 45.5	0.98 0.394 0.21	~0.97
Smart Nacre[102]	0.016 0.17 0.31	0.01 0.034 0.099	~0.97
Autonomous Self-healing Composite[103]	53.527 32.213	0.0654 0.0503	~0.6

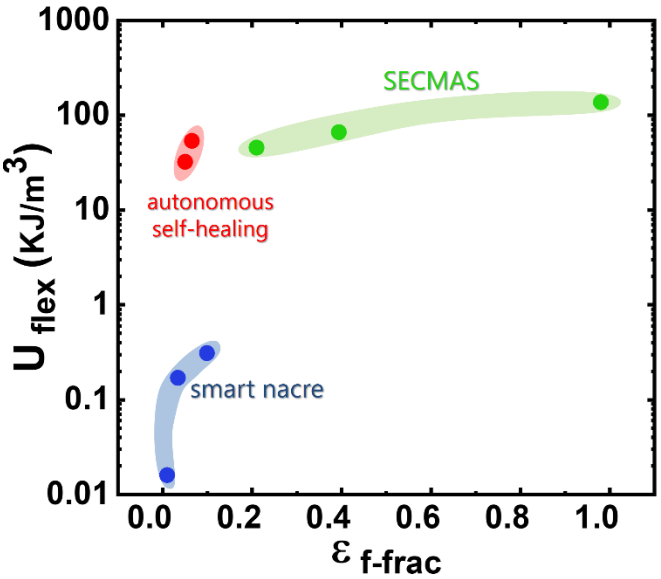

Figure 3.13. Maximum values of toughness and flexural strain of self-healing staggered composites under three-point bending loading.
Smart nacre,[102] Autonomous Self-healing composite,[103] and SECMAS.

3.4.7 Rapid Reconfigurability of SECMAS

The simple assembly and disassembly of SECMAS facilitates their rapid reconfigurability into a variety of structures, such as pillars, slabs, stairs, domes, or bridges (Figure 3.14). These structures benefit from the flexibility (Figure 3.14a), modularity (Figure 3.14b), self-healing properties (Figure 3.14c), and high resistance to compression (Figure 3.14a, d, e) provided by the mechanical adhesive interfaces and the elastomeric layers in SECMAS. Additionally, the modularity of SECMAS enables their fast dismantling, reconfiguration, and expansion into

different structures in order to meet new requirements (see how a dome-like SECMAS is reconfigured into a bridge, Figure 3.14d, e).

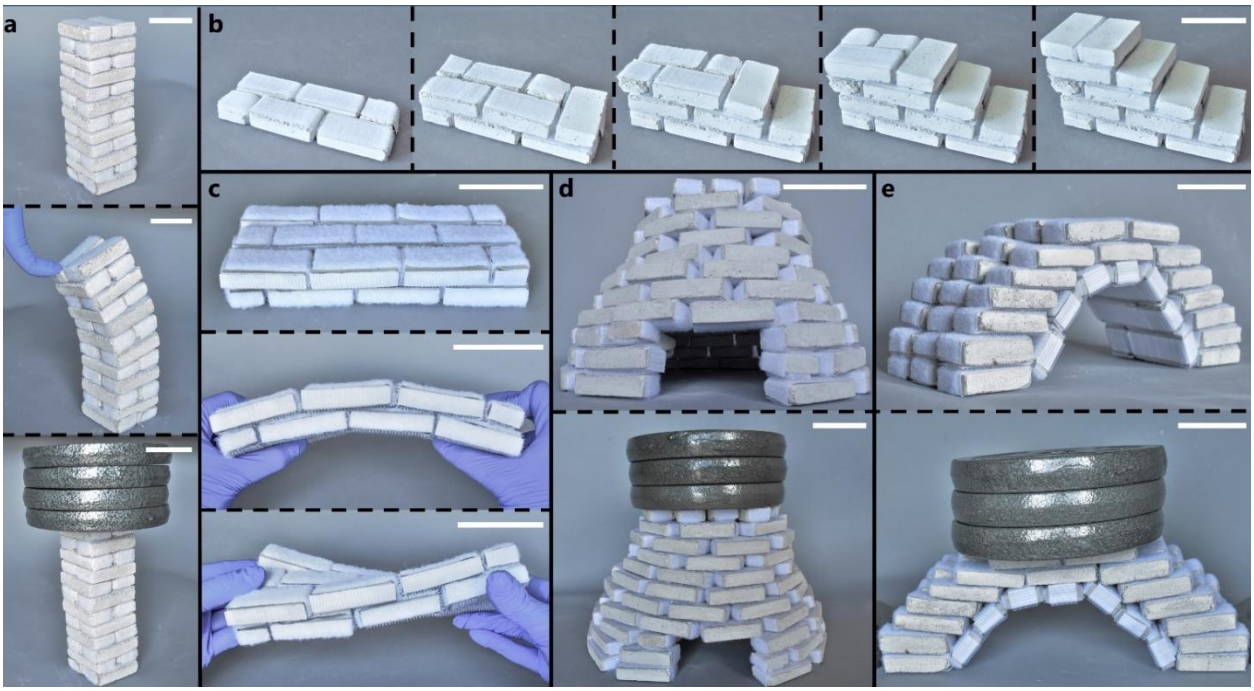

Figure 3.14. Rapid reconfigurability of SECMAS.
(a) flexible and strong SECMAS pillar holding a 10 lb. weight. (b) SECMAS stairs. (c) Flexible SECMAS slab. (d) SECMAS dome holding a 15 lb. weight. (e) SECMAS bridge holding a 15 lb. weight. All scale bars are 5 cm.

3.5 Conclusions

In summary, this work presents SECMAS, self-healing elastomeric/cementitious /mechanical adhesive structures easy to assemble and reconfigure into a variety of designs. SECMAS have a nacre-inspired structure composed of staggered cementitious bricks (99% in mass) connected by mechanical adhesive interfaces (0.2% in mass) and reinforced by elastomeric layers (0.8% in mass). Upon external loading, the mechanical adhesive interfaces of SECMAS efficiently distribute stresses, accommodate deformation, and concentrate crack formation and propagation. After the load disappears, the elastic recovery of the elastomeric layers in SECMAS brings back into contact the separated mechanical adhesive interfaces, restoring their binding and self-repairing SECMAS autonomously at room temperature. The rapid self-repairing of SECMAS allows them to recover their original strength and toughness after loads inducing severe cyclic bidirectional deformation ($\varepsilon_f = 0.21$). When compared with their monolithic counterparts, SECMAS exhibit flexural and compression toughness values 50 and 12 times greater,

respectively. Additionally, even after the mechanical failure of some of the bricks in their structure, the mechanical adhesive interfaces in SECMAS maintain the cohesion between the bricks, retarding catastrophic failure and enabling further dissipation of applied loads. SECMAS, at their present level of development, also have four limitations: (i) the rapidly self-healing but relatively weak mechanical adhesive interfaces reduce the maximum strength and stiffness of these composites assembled structures; (ii) the layer of glue needed to attach the mechanical adhesive interfaces to the surfaces of the cementitious bricks could be subject to delamination in the long term; (iii) The self-healing property of SECMAS is limited by the capability of the elastomeric layer to absorb the deformation within its elastic deformation range ($\varepsilon \leq 600\%$); (iv) the polymeric materials in SECMAS limit the capability of these assembled structures to endure extreme temperatures or fire. However, due to their simplicity, modularity, and rapid reconfigurability, SECMAS are versatile and can be extended, with the proper choice of materials, to the fabrication of resilient self-repairing structures for the rapid setup of new temporary and convertible constructions.

4 SELF-HEALING INTERFACES INSPIRED BY THE MOLECULAR UNFOLDING OF SELF-ASSEMBLED PROTEINS

4.1 Introduction

This chapter presents self-healing interfaces inspired by the molecular unfolding of self-assembled proteins. These interfaces are comprised of a set of adhesive materials placed between two magnets forming a "sandwich" structure. The judicious arrangement of its components makes the proposed interfaces monostable—the interface returns to the undeformed/close stable state upon the removal of the external load—which imparts self-assembly and self-healing capabilities to the interfaces. Furthermore, the bio-inspired modular unfolding mechanism of the interfaces endows the system with the ability to dissipate energy. I aim to provide a comprehensive analytical and experimental characterization of these self-healing interfaces to elucidate the design guidelines for the development of materials with high-energy dissipative characteristics. I also expect to extend the proposed methodology to different structural interfaces with improved performance under cycling loading conditions, expanding the design spectrum of resilient self-healing composites.

4.2 Problem Description

Advances in experimental, theoretical, and computational materials science have led to a deeper understanding of the proteins at the nacre interface and the important role they play in the overall material behavior as an energy dissipation mechanism.[104] Sacrificial bonds, hidden length in structural molecules, and modular elongation mechanism have been found to considerably increase the fracture toughness of biomaterials by providing a reversible, high energy dissipation mechanism, and self-healing property.[105] Schematics of the behavior of long modular molecules compared with short and long molecules are shown in Figure 4.1. The idealized curve for a fiber made of long molecules shows a gradual increment in the force as the material is stretched until it breaks. On the other hand, a fiber made of short molecules reaches the maximum force with less deformation compared to a fiber made of long molecules. Despite the differences in the mechanical behavior of both fibers (short and long molecules), the energy dissipated—measured as the area below the force-extension curve—in the deformation process is far from optimal. Therefore, a

fiber that display a force-extension curve that reaches a large force after a small deformation, but then maintains this force over large extensions dissipates more energy. This fiber would consist of molecules with modules that display a "saw-tooth" response where the peaks correspond to modules unfolding events.

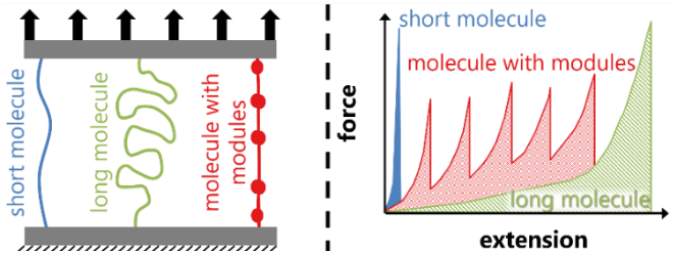

Figure 4.1. Schematics of the force-extension behavior of modular molecules compared with short and long molecules.[104]

The protein-based adhesive interfaces—joining aragonite platelets to form nacre—unfold into biopolymer fibrils upon elongation exhibiting a mechanical behavior similar to a molecule with modules (Figure 4.2a). The biopolymer fibrils can restore their folded configuration in the presence of moisture providing self-healing properties to nacre.[104] Similarly, organic interfaces and hook-and-loop mechanical adhesives have shown an analogous behavior to nacre's proteins-based interface. Under external loads, the attaching and detaching of the mechanical adhesive interfaces exhibit a characteristic force-extension response similar to nacre (Figure 4.2b, c), where the peaks correspond to ligaments or hook and loop detachment events. Shorter loops dominate the initial force-extension behavior (first peaks to appear in the force-extension curve, Figure 4.2b) and then longer loops carry out the loading upon larger deformation, enhancing the total energy dissipation at the interface.

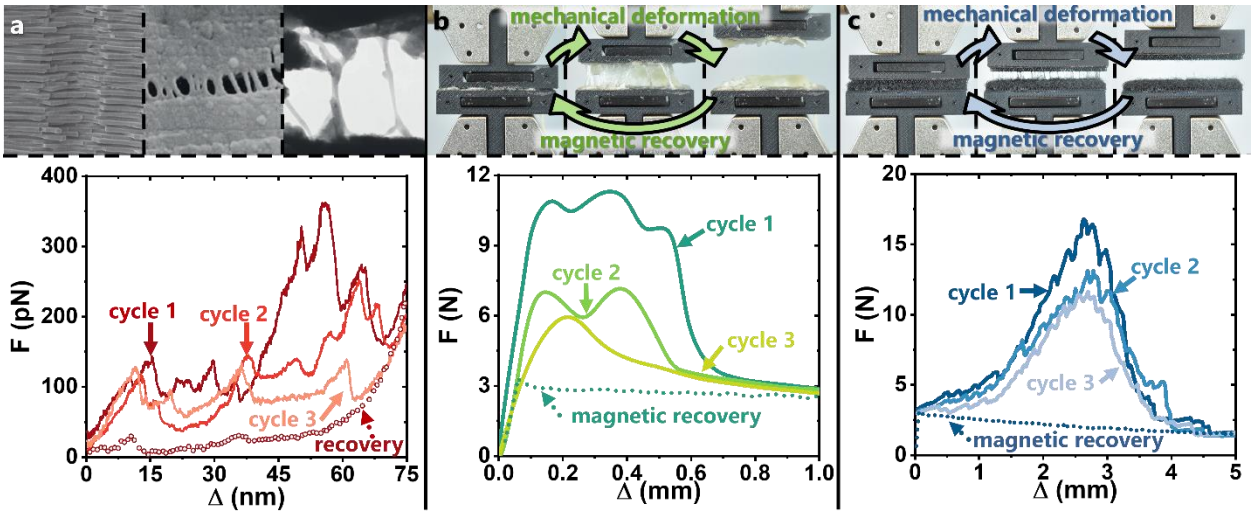

Figure 4.2. Nacre-inspired self-healing interfaces.
(a) SEM and transmission electron microscope image of the adhesive biopolymer fibrils bonding two aragonite platelets in nacre upon deformation (top).[63] Force-extension curve of the cyclic deformation process obtained by pulling two aragonite platelets using an atomic force microscope (bottom).[104] (b) and (c) Mechanical deformation and magnetic recovery cycles of the adhesive interfaces employed in this study (organic and mechanical adhesive interfaces, respectively).

4.3 Analytical Model for Self-Healing Interfaces Under Tension

4.3.1 Simplified Mathematical Formulation for One Simple Interface

First, I propose an analytical model for the mechanical behavior of the self-healing interfaces and its constituents, organic adhesive, hook-and-loop mechanical adhesive, and magnetic links. This simplified mathematical formulation is applicable in situations where the behavior of a mechanical adhesive interface can be described with a bi-linear force-displacement curve, such is the case for conventional adhesives like double-sided tape (Figure 4.3a). Upon tensile deformation of the conventional adhesive interface, the reaction force increases with an initial slope (k_1) until reaching a maximum (F_{max1}), following by a linearly decrement with slope (k_2). On the other hand, the magnet link is described with an initial linear increment of the force (initial slope k_3) and a post-peak force decrement that follow a non-linear behavior (Figure 4.3a).

The overall mechanical behavior of the self-healing conventional adhesive interface can be decomposed in the individual contribution of its constituents working synergistically—similar to a damper/spring system connected in parallel. Upon external deformation, the separation of the self-healing interface Δ_t is equal to the separation of the mechanical adhesive fastener Δ_1 and the

magnetic links Δ_2 ($\Delta_t = \Delta_1 = \Delta_2$). Conversely, the total force exerted by this self-healing interface F_t is the contribution the mechanical adhesive fasteners (F_1) and magnetic links ($F_t = F_1 + F_2$).

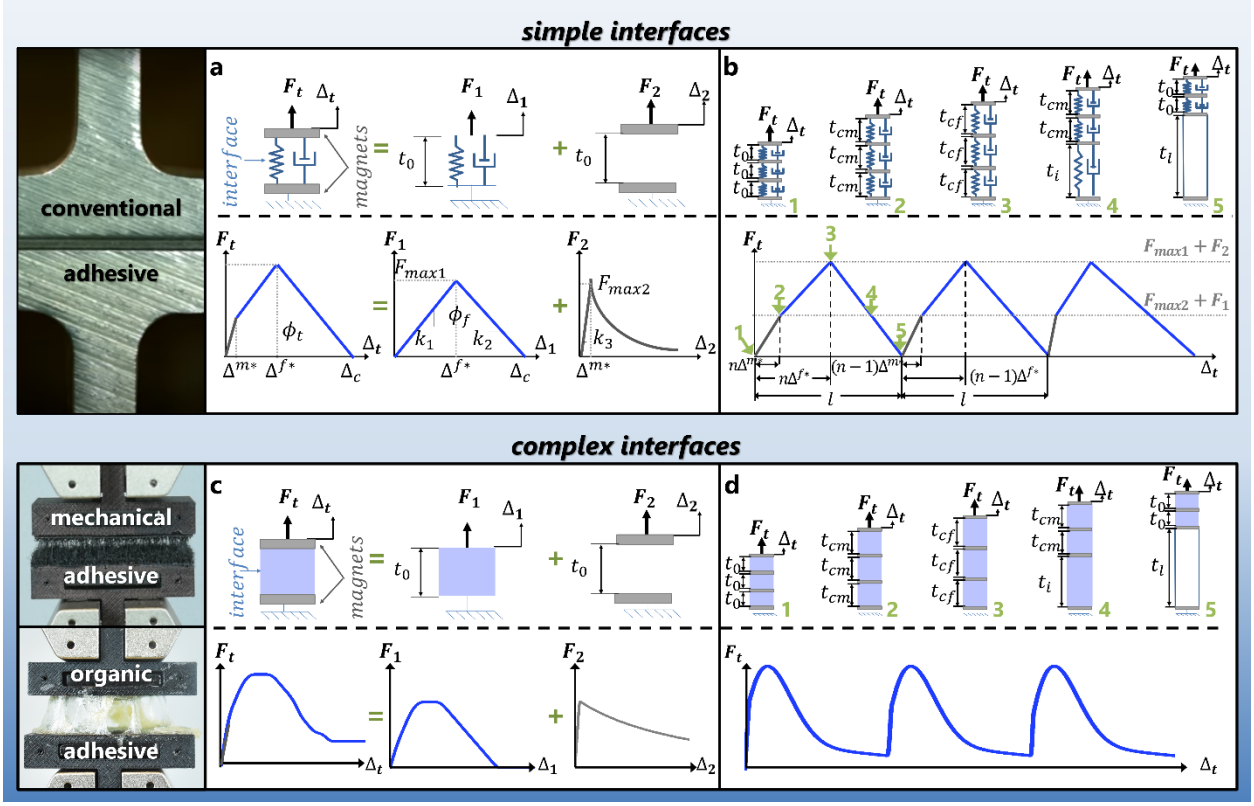

Figure 4.3. Schematic representation of the proposed self-healing interfaces.
(a) Mechanical adhesive fastener is placed between two cuboidal magnets to form a "sandwich" structure. The mechanical behavior of the self-healing interface can be taken/decouple as the combined reaction/behavior of its constituents. bilinear force displacement curve for the fasteners and non-linear performance for the magnetic links. (b) Stacked set of three self-healing interfaces with its force-displacement curve

The energy dissipated by the mechanical adhesive fasteners is calculated as the area below the curve: ϕ (Equation 12). The bi-linear force-displacement curve for the conventional adhesive can be described according to Equation 13, where the total displacement is given by $\Delta_c = F_{max1}/|k_1| + F_{max1}/|k_2|$ and the maximum force is reached at the displacement given by $\Delta^{f*} = F_{max1}/|k_1|$. On the other hand, the non-linear behavior of the magnets can be described according to Equation 14 where the displacement to reach the maximum force in the magnets is given by $\Delta^{m*} = F_{max2}/|k_3|$. The total force produced by the synergistic contribution of the constituents in the conventional self-healing interface can be calculated as the sum of the force exerted by the adhesive and the magnets (Equation 15).

$$\phi = \frac{\Delta_c F_{max1}}{2} = \frac{F_{max1}^2(|k_1|+|k_2|)}{2|k_1 k_2|} \quad (12)$$

$$F_1 = \frac{k_1\Delta_1 - F_{max1}}{2}\left(\frac{\Delta^{f*}-\Delta_1+\epsilon}{|\Delta^{f*}-\Delta_1+\epsilon|}+1\right) + \frac{k_2(\Delta_1-\Delta^{f*})}{2}\left(\frac{\Delta_1-\Delta^{f*}+\epsilon}{|\Delta_1-\Delta^{f*}+\epsilon|}+1\right) + F_{max1} \quad (13)$$

$$F_2 = \frac{k_3\Delta_2}{2}\left(\frac{\Delta^{m*}-\Delta_2+\epsilon}{|\Delta^{m*}-\Delta_2+\epsilon|}+1\right) - \frac{F_{max2}(\Delta_2-\Delta^{m*})}{2{\Delta_2}^2}\left(\frac{\Delta_2-\Delta^{m*}+\epsilon}{|\Delta_2-\Delta^{m*}+\epsilon|}+1\right) \quad (14)$$

$$F_t = \frac{k_1\Delta_t - F_{max1}}{2}\left(\frac{\Delta^{f*}-\Delta_t+\epsilon}{|\Delta^{f*}-\Delta_t+\epsilon|}+1\right) + \frac{k_2(\Delta_t-\Delta^{f*})}{2}\left(\frac{\Delta_t-\Delta^{f*}+\epsilon}{|\Delta_t-\Delta^{f*}+\epsilon|}+1\right) + F_{max1} + \frac{k_3\Delta_2}{2}\left(\frac{\Delta^{m*}-\Delta_2+\epsilon}{|\Delta^{m*}-\Delta_2+\epsilon|}+1\right) - \frac{F_{max2}(\Delta_2-\Delta^{m*})}{2{\Delta_2}^2}\left(\frac{\Delta_2-\Delta^{m*}+\epsilon}{|\Delta_2-\Delta^{m*}+\epsilon|}+1\right) \quad (15)$$

4.3.2 Simplified Mathematical Formulation for Stacked Simple Interfaces

Displacement control analysis is performed on a set of stacked self-healing interfaces. Starting from the initial close configuration where all the interfaces have an inherent thickness t_0 (size of the interface) Figure 4.3b-1, the stacked interfaces are deformed until the maximum magnetic force was reached (Figure 4.3b-2). Until point 2, the magnetic links dominate the initial slope for the force-extension curve. Continuing with the deformation process, the conventional adhesive in each interface carried out the reaction force of the system reaching the maximum force for the system (Figure 4.3b-3). If an infinitesimal displacement is applied at this point, given the irregularities and defects at the interfaces, one of the interfaces is triggered and starts to deform beyond the maximum force (Figure 4.3b-4), which implies a sudden reduce of the force. However, since the analysis is performed under displacement control, the other "sill open" interfaces take over the sudden change in displacement, recovering the equivalent displacement. The overall displacement is not affected, but the forces at the interfaces are subjected to sudden changes. This phenomenon is captured as a jump in the force-displacement curve of the system (See Figure 4.3b-5).

4.3.3 Refined Mathematical Formulation for One Complex Interface

4.3.3.1 Organic and Mechanical Adhesives

In Chapter 2, I developed and exhaustive numerical model that captures the mechanical performance of the mechanical adhesives, which can be used to describe a wide set of complex interfaces including the organic interfaces. The average traction-separation curve, obtained from

the experimental characterization of the complex adhesive interfaces, can be described mathematically with a potential-based cohesive model (PPR).[81,82] As explained in greater detail in Section 2.3.2.1, the PPR cohesive model will allow to capture the correct shape of the traction-separation model, by modifying its constitutive parameters (shape parameter α, final crack opening width δ, initial slope indicator λ, and fracture energy ϕ) in the effective traction-separation curve (σ_{eff}-Δ_n), see Figure 2.18. The cohesive model with respect to normal tractions is presented in Equation 16.[82] This mathematical derivation, compared with Equation 8, focus only in normal/tensile forces and omits the effect of tangential cohesive traction. The energy constants $\Gamma_1 = -\phi(\alpha/m)^m$ and $\Gamma_2 = (\alpha/m)^m$, and exponent associated with the initial slope $m = \alpha(\alpha-1)\lambda_n{}^2/(1-\alpha\lambda_n{}^2)$ are implemented in a Matlab code for effective manipulation of the parameters. The resulting parameters that replicates the average traction-separation curve can be found in Table 4-1.

Table 4-1. Analytical parameters for complex interfaces

Parameter	Organic Interface	Mechanical Interface
α	9.0 [−]	6.5 [−]
ϕ_n	0.01 [N/mm]	0.02 [N/mm]
λ_n	0.2 [MPa/mm]	0.3 [MPa/mm]
δ_n	5 [mm]	5 [mm]

$$\sigma_{eff}(\Delta_n) = \frac{\Gamma_1}{\delta_1}\left[m\left(1-\frac{\Delta_t}{\delta_1}\right)^{\alpha}\left(\frac{m}{\alpha}+\frac{\Delta_t}{\delta_1}\right)^{m-1} - \alpha\left(1-\frac{\Delta_t}{\delta_1}\right)^{\alpha-1}\left(\frac{m}{\alpha}+\frac{\Delta_t}{\delta_1}\right)^{m}\right] \mathrm{x}\left[\Gamma_2\left(\frac{n}{\beta}\right)^{n}\right] \quad (16)$$

4.3.3.2 Cuboidal Magnets

Akoun et al,[106] presented an analytical calculation to quantify the interaction forces exerted between two cuboidal magnets in a three-dimensional space, Equation 19. The authors approach considers the different spatial interaction (separation in X, Y or Z direction with centers shifted a distance α, β and γ, respectively) between two cuboidal magnets with dimensions $2a \times 2b \times 2c$ and $2A \times 2B \times 2C$ (Figure 4.4). Despite the complexity of the mathematical calculation, this section focuses on capturing the behavior of two identical magnets ($\mathrm{a} = \mathrm{A} = 12.7[\mathrm{mm}], \mathrm{b} = \mathrm{B} = 12.7[\mathrm{mm}], \mathrm{c} = \mathrm{C} = 1.5875[\mathrm{mm}]$) aligned in X and Y

direction ($\alpha = \beta = 0$) experiencing separation only in the Z direction ($\gamma = \Delta_n$). Made of Machinable Rare Earth Magnetic Bar ($J = J' = 0.0038$ [mT], $u_0 = 0.0001$ [mm T / Amp]), the exerted force between the magnets is strictly correlated with their dimensions. The interaction energy between the magnets depends on the separation and is calculated with the Equation 17, with the displacements in X, Y, Z, and radius r.

$$u_{ij} = \alpha + (-1)^j$$

$$v_{ij} = \beta + (-1)^l$$

$$w_{pq} = \gamma + (-1)^q$$

$$r = \left(u_{ij}^2 + v_{kl}^2 + w_{pq}^2\right)^{1/2} \tag{17}$$

$$\varphi_z = -uw\ln(r-u) - vu\ln(r-v) + uv\ \tan^{-1}\left(\frac{uv}{rw}\right) - rw \tag{18}$$

$$F_2(\Delta_n) = \frac{JJ'}{4\pi u_0}\sum_{i=0}^{1}\sum_{j=0}^{1}\sum_{k=0}^{1}\sum_{l=0}^{1}\sum_{p=0}^{1}\sum_{q=0}^{1}(-1)^{i+j+k+l+p+q}\ \varphi_z(u_{ij}, v_{kl}, w_{pq}, r) \tag{19}$$

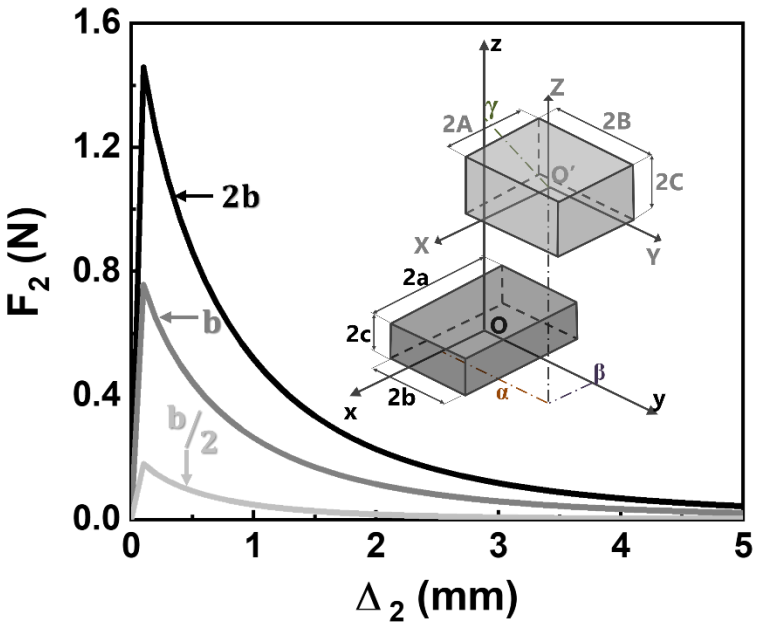

Figure 4.4. Force exerted by two cuboidal magnets of different sizes.[106]

4.4 Materials and Methods

4.4.1 Nacre-Inspired Self-Healing Interfaces

The process of unfolding self-healing molecules with modules is reproduced by placing an interface of adhesive materials between two cuboidal magnets forming a “sandwich” structure that efficiently captures the modular behavior, while preserving the ability to self-assemble, of a molecule when removing external load. Upon the application of tensile forces, the self-healing interface experiences two combined forces acting on it: the complex interface (organic or mechanical adhesive) and the magnetic link. Assembled sequentially, several independent interfaces are connected by strong but flexible threads that allow the distribution of tensile forces between neighboring interfaces. Following the complete detachment of one interface, the thread transfers the tensile force to the following interface.

4.4.2 Fabrication of Supports and Sample Preparation

Organic adhesive material were fabricated by mixing beef gelatin (Aspen Naturals) with egg whites in a 1:5 weight ratio. The mixture was then homogenized by increasing its temperature up to 80°F and then poured into the flat surface of the 3D printed supports. Mechanical adhesive interfaces were constructed by bonding 24.5 mm x 40 mm hook-and-loop surfaces to opposite faces of 3D printed supports using a cyanoacrylate adhesive gel (Loctite 409; Henkel Ltd.). The 3D supports have a square opening in the middle to place the Neodymium Grade N10 (Rare Earth) cuboidal magnets (25.4 mm x 25.4 mm x 3.175 mm). Strong and flexible Nylon threads (0.032” diameter) connect neighboring interfaces limiting their deformation and allowing sequential activation of the stacked structure. An aluminum rail constrains the stacked interfaces to move only vertically while restricting their rotation in all directions.

4.4.3 Mechanical Performance of Self-healing Interfaces

Figure 4.5 and Figure 4.6 shows the mechanical performance of self-healing interfaces under tension forces, for one and three stacked interfaces, respectively. For one interface, the refined analytical model accurately capture the behavior of the self-healing interface. These results open the possibility to fine-tune key parameters in the architecture design of the self-healing interface (such as peak-force, displacement to reach maximum force, initial slope, etc.) to optimize the

overall system performance. For the case of three interfaces, the number of peaks in force-extension curve matches the number of interfaces. Such behavior can be comparable to the modular unfolding of the proteins, in which case, each module/domain would correspond to an interface. Furthermore, the three stacked interfaces display an ascending peak-force pattern in its force-extension curve.

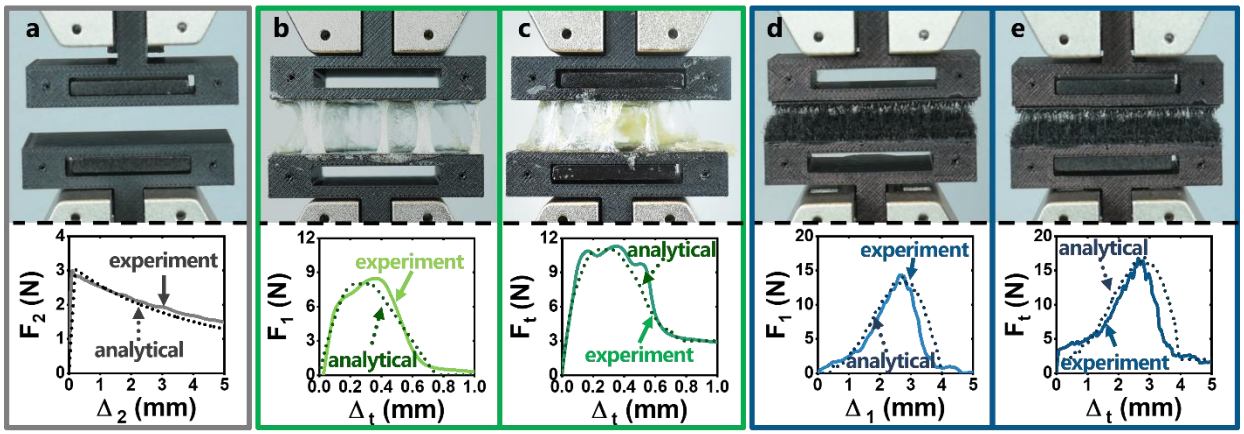

Figure 4.5. Comparison between experimental results and the refined analytic model for tensile loading condition.

(a) magnet only. (b) organic interface only. (c) organic interface and magnet. (d) mechanical adhesive interface only. (e) mechanical adhesive interface and magnet.

The force required to detach an interface increases with each successive break (e.g., the first peak reports a lower force value than the third peak). The random distribution of fibers in the hook-and-loop mechanical adhesive introduces variability in the adhesion of mechanical adhesive interfaces. As result, the weakest interface is more likely to detach first leaving the stronger interfaces for the consecutive detachment (higher maximum force). The mechanical characterization experiments were performed in a universal tensile testing machine (MTS ESM1500; Mark10 Corp.) equipped with a 100 N load cell (model MR011000). at a loading rate of 3 mm/min.

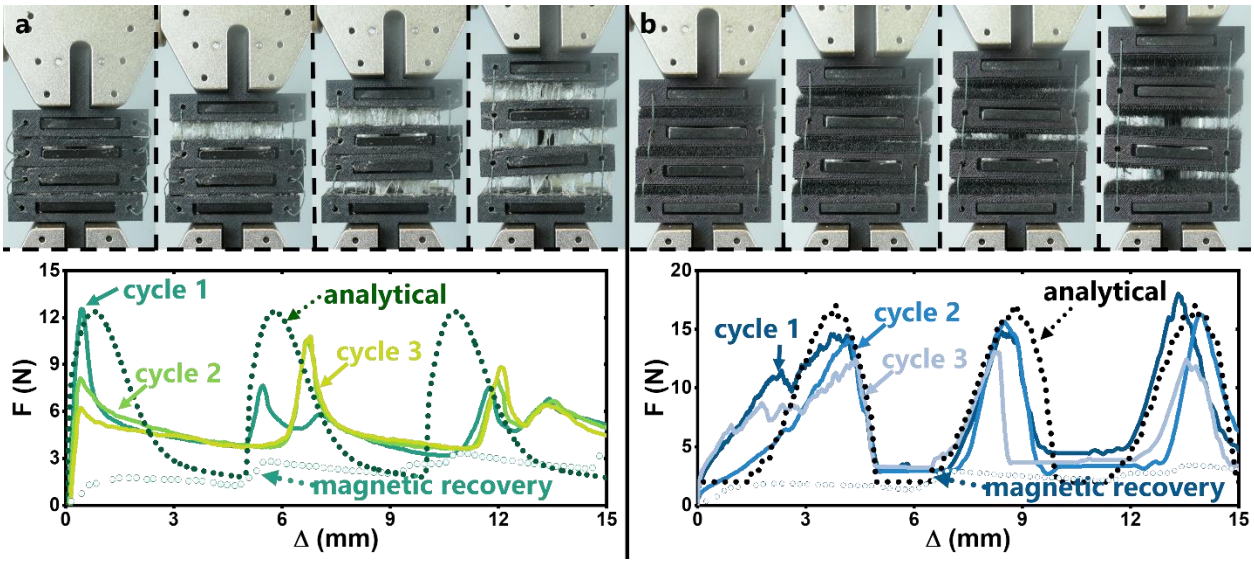

Figure 4.6: Comparison between experimental results and the refined analytic model for three stacked interfaces under tensile loading condition.
(a) organic interfaces and magnets. (b) mechanical adhesive interfaces and magnets.

4.5 Conclusions

In summary, this work presents self-healing interfaces inspired by the molecular unfolding of self-assembled proteins. These interfaces are comprised of a set of adhesive materials placed between two magnets forming a layered structure. The judicious arrangement of its components imparts self-assembly and self-healing capabilities to the proposed interfaces. Furthermore, the bio-inspired modular unfolding mechanism of the interfaces endows the system with the ability to dissipate energy. The comprehensive analytical and experimental characterization of self-healing interfaces proposed here enables the development of materials with high energy dissipative characteristics. The number of peaks in load matched the number of interfaces opening the possibility to extend the numbers of interfaces and improve the energy absorption property of the structure. The force increased as the interfaces were stretched, and the reversible adhesive remained attached. However, when the bond starts to break the force decreased, and then built up again as interface was slowly pulled apart. The measured force reached a higher peak with each successive break, the non-uniformity and the randomly distribution of fibers in the mechanical adhesives, generates weaker bonds in the interface. As result, the weakest interface is more likely to detach first leaving the stronger ones for the consecutive detachment (higher maximum force). Unloading curves followed a different path back to zero extension compared with loading, with the corresponding load decreasing along the y-axis over time. An analytical and experimental

characterization of stacked set of self-healing interfaces arranged in series was performed. The experimental results with three interfaces exhibit a pattern that mimics the proteins' unfolding mechanism in loading mode. I expect to extend the methodology to different structural interfaces with improved performance under cycling loading conditions, expanding the design spectrum of resilient self-healing composites.

5 CONCLUSIONS

In summary, this Ph.D. dissertation demonstrates scalable and modular structural materials that have enhanced mechanical performance and the capability to self-repair autonomously. The bioinspired self-healing composite and modular interfaces introduced in Chapter 3 and 4, benefit from the hook-and-loop mechanical adhesive interfaces developed in Chapter 2.

In Chapter 2, I employed the multi-scale approach to understand the mechanical behavior of the hook-and-loop fastener at the micro- and macroscales. The two-scale approach enabled me to connect the results from the RHLE model (micromechanical model) to a larger scale structures, such as the DCB or peel tests (macromechanical model). I first presented a new computational high-fidelity micromechanical model that includes detailed information of the hooks and loops geometry and basic mechanical behavior. This model captures the general behavior and response of the fastener, such as detachment and pull-out under mode-I loading condition. By establishing a general contact formulation between hooks and loops, I was able to capture both engagement and pull-out process similar to experimental observation. Hook-and-loop fastener are made of polypropylene, and the mechanical behavior of individual loops was characterized by performing pull-out tests on a single and multiple fibers. Based on the experiments, the fibers behave elastoplastic while the hooks remained elastic during the tests. To increase the accuracy of this model, I developed a loop mesh generator code to account for the statistical variation in geometry, volume fraction , diameter, and length of an individual fiber. The loop generator code enabled me to capture the statistical variations that we observed the loops fibrous tape.

In Chapter 3, I presented SECMAS, self-healing elastomeric/cementitious/mechanical adhesive structures easy to assemble and reconfigure into a variety of designs. SECMAS have a nacre-inspired structure composed of staggered cementitious bricks (99% in mass) connected by mechanical adhesive interfaces (0.2% in mass) and reinforced by elastomeric layers (0.8% in mass). Upon external loading, the mechanical adhesive interfaces of SECMAS efficiently distribute stresses, accommodate deformation, and concentrate crack formation and propagation. After the load disappears, the elastic recovery of the elastomeric layers in SECMAS brings back into contact the separated mechanical adhesive interfaces, restoring their binding and self-repairing SECMAS autonomously at room temperature. The rapid self-repairing of SECMAS allows them to recover their original strength and toughness after loads inducing severe cyclic bidirectional

deformation ($\varepsilon_f = 0.21$). When compared with their monolithic counterparts, SECMAS exhibit flexural and compression toughness values 50 and 12 times greater, respectively. Additionally, even after the mechanical failure of some of the bricks in their structure, the mechanical adhesive interfaces in SECMAS maintain the cohesion between the bricks, retarding catastrophic failure and enabling further dissipation of applied loads. SECMAS, at their present level of development, also have four limitations: (i) the rapidly self-healing but relatively weak mechanical adhesive interfaces reduce the maximum strength and stiffness of these composites assembled structures; (ii) the layer of glue needed to attach the mechanical adhesive interfaces to the surfaces of the cementitious bricks could be subject to delamination in the long term; (iii) The self-healing property of SECMAS is limited by the capability of the elastomeric layer to absorb the deformation within its elastic deformation range ($\varepsilon \leq 600\%$); (iv) the polymeric materials in SECMAS limit the capability of these assembled structures to endure extreme temperatures or fire. However, due to their simplicity, modularity, and rapid reconfigurability, SECMAS are versatile and can be extended, with the proper choice of materials, to the fabrication of resilient self-repairing structures for the rapid setup of new temporary and convertible constructions.

Finally, in Chapter 4, I provided a comprehensive analytical and experimental characterization of two self-healing interfaces inspired by the molecular unfolding of self-assembled proteins. These adhesive interfaces are monostable—the interface returns to the undeformed/close stable state upon the removal of the external load—which imparts self-assembly and self-healing capabilities to the interfaces. Furthermore, the bio inspired modular unfolding mechanism of the interfaces endows the system with the ability to dissipate energy. It is expected that the proposed methodology sheds light on the design guidelines for the development of materials with high energy dissipative characteristics. It is also expected to extend the methodology to different structural interfaces with improved performance under cycling loading conditions, expanding the design spectrum of resilient self-healing composites.

I envision that the results from this dissertation provide new insight through the design and fabrication of mechanics of scalable and modular structural materials and serves as an attractive strategy for the development of resilient, deployable, convertible, and temporary constructions capable to meet the rapidly increasing modern demands.

REFERENCES

(1) Buehler, M. J. Molecular Nanomechanics of Nascent Bone: Fibrillar Toughening by Mineralization. *Nanotechnology* **2007**, *18* (29), 295102. https://doi.org/10.1088/0957-4484/18/29/295102.

(2) Egan, P.; Sinko, R.; LeDuc, P. R.; Keten, S. The Role of Mechanics in Biological and Bio-Inspired Systems. *Nat Commun* **2015**, *6* (1), 7418. https://doi.org/10.1038/ncomms8418.

(3) De Temmerman, N.; Mira, L. A.; Vergauwen, A.; Hendrickx, H.; De Wilde, W. P. Transformable Structures in Architectural Engineering; New Forest, UK, 2012; pp 457–468. https://doi.org/10.2495/HPSM120411.

(4) Rios, F. C.; Chong, W. K.; Grau, D. Design for Disassembly and Deconstruction - Challenges and Opportunities. *Procedia Engineering* **2015**, *118*, 1296–1304. https://doi.org/10.1016/j.proeng.2015.08.485.

(5) Corni, I.; Harvey, T. J.; Wharton, J. A.; Stokes, K. R.; Walsh, F. C.; Wood, R. J. K. A Review of Experimental Techniques to Produce a Nacre-like Structure. *Bioinspir. Biomim.* **2012**, *7* (3), 031001. https://doi.org/10.1088/1748-3182/7/3/031001.

(6) Bouville, F. Strong and Tough Nacre-like Aluminas: Process–Structure–Performance Relationships and Position within the Nacre-Inspired Composite Landscape. *J. Mater. Res.* **2020**, 1–19. https://doi.org/10.1557/jmr.2019.418.

(7) Ko, K.; Jin, S.; Lee, S. E.; Lee, I.; Hong, J.-W. Bio-Inspired Bimaterial Composites Patterned Using Three-Dimensional Printing. *Composites Part B: Engineering* **2019**, *165*, 594–603. https://doi.org/10.1016/j.compositesb.2019.02.008.

(8) He, G.; Li, X.; Dai, Y.; Yang, Z.; Zeng, C.; Lin, C.; He, S. Constructing Bioinspired Hierarchical Structure in Polymer Based Energetic Composites with Superior Thermal Conductivity. *Composites Part B: Engineering* **2019**, *162*, 678–684. https://doi.org/10.1016/j.compositesb.2019.01.046.

(9) Ashby, M. F.; Bréchet, Y. J. M. Designing Hybrid Materials. *Acta Materialia* **2003**, *51* (19), 5801–5821. https://doi.org/10.1016/S1359-6454(03)00441-5.

(10) Barthelat, F.; Yin, Z.; Buehler, M. J. Structure and Mechanics of Interfaces in Biological Materials. *Nature Reviews Materials* **2016**, *1* (4), natrevmats20167. https://doi.org/10.1038/natrevmats.2016.7.

(11) Jia, Z.; Yu, Y.; Wang, L. Learning from Nature: Use Material Architecture to Break the Performance Tradeoffs. *Materials & Design* **2019**, *168*, 107650. https://doi.org/10.1016/j.matdes.2019.107650.

(12) Walther, A.; Bjurhager, I.; Malho, J.-M.; Ruokolainen, J.; Berglund, L.; Ikkala, O. Supramolecular Control of Stiffness and Strength in Lightweight High-Performance Nacre-Mimetic Paper with Fire-Shielding Properties. *Angewandte Chemie International Edition* **2010**, *49* (36), 6448–6453. https://doi.org/10.1002/anie.201001577.

(13) Podsiadlo, P.; Kaushik, A. K.; Arruda, E. M.; Waas, A. M.; Shim, B. S.; Xu, J.; Nandivada, H.; Pumplin, B. G.; Lahann, J.; Ramamoorthy, A.; Kotov, N. A. Ultrastrong and Stiff Layered Polymer Nanocomposites. *Science* **2007**, *318* (5847), 80–83. https://doi.org/10.1126/science.1143176.

(14) Radi, K.; Jauffres, D.; Deville, S.; Martin, C. L. Strength and Toughness Trade-off Optimization of Nacre-like Ceramic Composites. *Composites Part B: Engineering* **2020**, *183*, 107699. https://doi.org/10.1016/j.compositesb.2019.107699.

(15) Liu, C. H.; Li, W.-Z.; Li, H.-D. Simulation of Nacre with TiC/Metal Multilayers and a Study of Their Toughness. *Materials Science and Engineering: C* **1996**, *4* (3), 139–142. https://doi.org/10.1016/S0928-4931(96)00145-2.
(16) Liu, F.; Li, T.; Jia, Z.; Wang, L. Combination of Stiffness, Strength, and Toughness in 3D Printed Interlocking Nacre-like Composites. *Extreme Mechanics Letters* **2020**, *35*, 100621. https://doi.org/10.1016/j.eml.2019.100621.
(17) Ha, N. S.; Lu, G. A Review of Recent Research on Bio-Inspired Structures and Materials for Energy Absorption Applications. *Composites Part B: Engineering* **2020**, *181*, 107496. https://doi.org/10.1016/j.compositesb.2019.107496.
(18) Barthelat, F. Designing Nacre-like Materials for Simultaneous Stiffness, Strength and Toughness: Optimum Materials, Composition, Microstructure and Size. *Journal of the Mechanics and Physics of Solids* **2014**, *73*, 22–37. https://doi.org/10.1016/j.jmps.2014.08.008.
(19) D'Elia, E.; Eslava, S.; Miranda, M.; Georgiou, T. K.; Saiz, E. Autonomous Self-Healing Structural Composites with Bio-Inspired Design. *Scientific Reports* **2016**, *6*, 25059. https://doi.org/10.1038/srep25059.
(20) Rezaee Javan, A.; Seifi, H.; Lin, X.; Xie, Y. M. Mechanical Behaviour of Composite Structures Made of Topologically Interlocking Concrete Bricks with Soft Interfaces. *Materials & Design* **2020**, *186*, 108347. https://doi.org/10.1016/j.matdes.2019.108347.
(21) Wu, K.; Zheng, Z.; Zhang, S.; He, L.; Yao, H.; Gong, X.; Ni, Y. Interfacial Strength-Controlled Energy Dissipation Mechanism and Optimization in Impact-Resistant Nacreous Structure. *Materials & Design* **2019**, *163*, 107532. https://doi.org/10.1016/j.matdes.2018.12.004.
(22) Sun, W.; Neuzil, P.; Kustandi, T. S.; Oh, S.; Samper, V. D. The Nature of the Gecko Lizard Adhesive Force. *Biophysical Journal* **2005**, *89* (2), L14–L17. https://doi.org/10.1529/biophysj.105.065268.
(23) Autumn, K.; Liang, Y. A.; Hsieh, S. T.; Zesch, W.; Chan, W. P.; Kenny, T. W.; Fearing, R.; Full, R. J. Adhesive Force of a Single Gecko Foot-Hair. *Nature* **2000**, *405* (6787), 681–685. https://doi.org/10.1038/35015073.
(24) Niederegger, S.; Gorb, S. N. Friction and Adhesion in the Tarsal and Metatarsal Scopulae of Spiders. *J Comp Physiol A* **2006**, *192* (11), 1223–1232. https://doi.org/10.1007/s00359-006-0157-y.
(25) Dejean, A.; Leroy, C.; Corbara, B.; Roux, O.; Céréghino, R.; Orivel, J.; Boulay, R. Arboreal Ants Use the "Velcro® Principle" to Capture Very Large Prey. *PLOS ONE* **2010**, *5* (6), e11331. https://doi.org/10.1371/journal.pone.0011331.
(26) Sullivan, T. N.; Pissarenko, A.; Herrera, S. A.; Kisailus, D.; Lubarda, V. A.; Meyers, M. A. A Lightweight, Biological Structure with Tailored Stiffness: The Feather Vane. *Acta Biomaterialia* **2016**, *41*, 27–39. https://doi.org/10.1016/j.actbio.2016.05.022.
(27) Hui, C.-Y.; Long, R.; Wahl, K. J.; Everett, R. K. Barnacles Resist Removal by Crack Trapping. *J. R. Soc. Interface.* **2011**, *8* (59), 868–879. https://doi.org/10.1098/rsif.2010.0567.
(28) Morano, C.; Zavattieri, P.; Alfano, M. Tuning Energy Dissipation in Damage Tolerant Bio-Inspired Interfaces. *Journal of the Mechanics and Physics of Solids* **2020**, *141*, 103965. https://doi.org/10.1016/j.jmps.2020.103965.

(29) Kapsali, V. Biomimetic Principles for Design of Water Repellent Surfaces. In *Waterproof and Water Repellent Textiles and Clothing*; Elsevier, 2018; pp 121–135. https://doi.org/10.1016/B978-0-08-101212-3.00005-8.
(30) Kennedy, W. J.; Rocha, G. F. Hook Design for a Hook and Loop Fastener. US5339499A, August 23, 1994.
(31) Restrepo, V.; Martinez, R. V. Bioinspired Fabrication of Reconfigurable Elastomeric Cementitious Structures Using Self-Healing Mechanical Adhesives Interfaces. *Materials & Design* **2021**, *205*, 109691. https://doi.org/10.1016/j.matdes.2021.109691.
(32) Hebeler, G. L.; Frost, J. D.; Myers, A. T. Quantifying Hook and Loop Interaction in Textured Geomembrane–Geotextile Systems. *Geotextiles and Geomembranes* **2005**, *23* (1), 77–105. https://doi.org/10.1016/j.geotexmem.2004.06.002.
(33) Meislin, R. Single Unit Surgical Fastener and Method. US6039753A, March 21, 2000.
(34) Berber, S.; Kwon, Y.-K.; Tománek, D. Bonding and Energy Dissipation in a Nanohook Assembly. *Phys. Rev. Lett.* **2003**, *91* (16), 165503. https://doi.org/10.1103/PhysRevLett.91.165503.
(35) Pugno, N. M. Velcro® Nonlinear Mechanics. *Applied Physics Letters* **2007**, *90* (12), 121918. https://doi.org/10.1063/1.2715478.
(36) Vokoun, D.; Sedlák, P.; Frost, M.; Pilch, J.; Majtás, D.; Šittner, P. Velcro-like Fasteners Based on NiTi Micro-Hook Arrays. *Smart Mater. Struct.* **2011**, *20* (8), 085027. https://doi.org/10.1088/0964-1726/20/8/085027.
(37) Williams, J. A.; Davies, S. G.; Frazer, S. The Peeling of Flexible Probabilistic Fasteners. *Tribol Lett* **2007**, *26* (3), 213–222. https://doi.org/10.1007/s11249-006-9187-4.
(38) Nguyen, V. P.; Stroeven, M.; Sluys, L. J. Multiscale Failure Modeling of Concrete: Micromechanical Modeling, Discontinuous Homogenization and Parallel Computations. *Computer Methods in Applied Mechanics and Engineering* **2012**, *201–204*, 139–156. https://doi.org/10.1016/j.cma.2011.09.014.
(39) Esmaeeli, H. S.; Shishehbor, M.; Weiss, W. J.; Zavattieri, P. D. A Two-Step Multiscale Model to Predict Early Age Strength Development of Cementitious Composites Considering Competing Fracture Mechanisms. *Construction and Building Materials* **2019**, *208*, 577–600. https://doi.org/10.1016/j.conbuildmat.2019.02.134.
(40) Aragón, A. M.; Soghrati, S.; Geubelle, P. H. Effect of In-Plane Deformation on the Cohesive Failure of Heterogeneous Adhesives. *Journal of the Mechanics and Physics of Solids* **2013**, *61* (7), 1600–1611. https://doi.org/10.1016/j.jmps.2013.03.003.
(41) Kulkarni, M. G.; Geubelle, P. H.; Matouš, K. Multi-Scale Modeling of Heterogeneous Adhesives: Effect of Particle Decohesion. *Mechanics of Materials* **2009**, *41* (5), 573–583. https://doi.org/10.1016/j.mechmat.2008.10.012.
(42) Matouš, K.; Kulkarni, M. G.; Geubelle, P. H. Multiscale Cohesive Failure Modeling of Heterogeneous Adhesives. *Journal of the Mechanics and Physics of Solids* **2008**, *56* (4), 1511–1533. https://doi.org/10.1016/j.jmps.2007.08.005.
(43) Cattaneo, S.; Biolzi, L. Assessment of Thermal Damage in Hybrid Fiber-Reinforced Concrete. *J. Mater. Civ. Eng.* **2010**, *22* (9), 836–845. https://doi.org/10.1061/(ASCE)MT.1943-5533.0000078.
(44) Ortiz, M. Microcrack Coalescence and Macroscopic Crack Growth Initiation in Brittle Solids. *International Journal of Solids and Structures* **1988**, *24* (3), 231–250. https://doi.org/10.1016/0020-7683(88)90031-5.

(45) Wu, M.; Johannesson, B.; Geiker, M. A Review: Self-Healing in Cementitious Materials and Engineered Cementitious Composite as a Self-Healing Material. *Construction and Building Materials* **2012**, *28* (1), 571–583. https://doi.org/10.1016/j.conbuildmat.2011.08.086.
(46) Wang, X.; Fang, C.; Li, D.; Han, N.; Xing, F. A Self-Healing Cementitious Composite with Mineral Admixtures and Built-in Carbonate. *Cement and Concrete Composites* **2018**, *92*, 216–229. https://doi.org/10.1016/j.cemconcomp.2018.05.013.
(47) Coppola, L.; Coffetti, D.; Crotti, E. Innovative Carboxylic Acid Waterproofing Admixture for Self-Sealing Watertight Concretes. *Construction and Building Materials* **2018**, *171*, 817–824. https://doi.org/10.1016/j.conbuildmat.2018.03.201.
(48) Borg, R. P.; Cuenca, E.; Gastaldo Brac, E. M.; Ferrara, L. Crack Sealing Capacity in Chloride-Rich Environments of Mortars Containing Different Cement Substitutes and Crystalline Admixtures. *Journal of Sustainable Cement-Based Materials* **2018**, *7* (3), 141–159. https://doi.org/10.1080/21650373.2017.1411297.
(49) Feiteira, J.; Tsangouri, E.; Gruyaert, E.; Lors, C.; Louis, G.; De Belie, N. Monitoring Crack Movement in Polymer-Based Self-Healing Concrete through Digital Image Correlation, Acoustic Emission Analysis and SEM in-Situ Loading. *Materials & Design* **2017**, *115*, 238–246. https://doi.org/10.1016/j.matdes.2016.11.050.
(50) Araújo, M.; Van Vlierberghe, S.; Feiteira, J.; Graulus, G.-J.; Van Tittelboom, K.; Martins, J. C.; Dubruel, P.; De Belie, N. Cross-Linkable Polyethers as Healing/Sealing Agents for Self-Healing of Cementitious Materials. *Materials & Design* **2016**, *98*, 215–222. https://doi.org/10.1016/j.matdes.2016.03.005.
(51) Sisomphon, K.; Copuroglu, O.; Koenders, E. A. B. Self-Healing of Surface Cracks in Mortars with Expansive Additive and Crystalline Additive. *Cement and Concrete Composites* **2012**, *34* (4), 566–574. https://doi.org/10.1016/j.cemconcomp.2012.01.005.
(52) Dong, B.; Wang, Y.; Fang, G.; Han, N.; Xing, F.; Lu, Y. Smart Releasing Behavior of a Chemical Self-Healing Microcapsule in the Stimulated Concrete Pore Solution. *Cement and Concrete Composites* **2015**, *56*, 46–50. https://doi.org/10.1016/j.cemconcomp.2014.10.006.
(53) Nagataki, S.; Gomi, H. Expansive Admixtures (Mainly Ettringite). *Cement and Concrete Composites* **1998**, *20* (2–3), 163–170. https://doi.org/10.1016/S0958-9465(97)00064-4.
(54) Lee, Y.-S.; Ryou, J.-S. Self Healing Behavior for Crack Closing of Expansive Agent via Granulation/Film Coating Method. *Construction and Building Materials* **2014**, *71*, 188–193. https://doi.org/10.1016/j.conbuildmat.2014.08.045.
(55) *Self-Healing Phenomena in Cement-Based Materials*; de Rooij, M., Van Tittelboom, K., De Belie, N., Schlangen, E., Eds.; RILEM State-of-the-Art Reports; Springer Netherlands: Dordrecht, 2013; Vol. 11. https://doi.org/10.1007/978-94-007-6624-2.
(56) Alghamri, R.; Kanellopoulos, A.; Litina, C.; Al-Tabbaa, A. Preparation and Polymeric Encapsulation of Powder Mineral Pellets for Self-Healing Cement Based Materials. *Construction and Building Materials* **2018**, *186*, 247–262. https://doi.org/10.1016/j.conbuildmat.2018.07.128.
(57) Huang, H.; Ye, G.; Qian, C.; Schlangen, E. Self-Healing in Cementitious Materials: Materials, Methods and Service Conditions. *Materials & Design* **2016**, *92*, 499–511. https://doi.org/10.1016/j.matdes.2015.12.091.
(58) Su, Y.; Feng, J.; Jin, P.; Qian, C. Influence of Bacterial Self-Healing Agent on Early Age Performance of Cement-Based Materials. *Construction and Building Materials* **2019**, *218*, 224–234. https://doi.org/10.1016/j.conbuildmat.2019.05.077.

(59) Gupta, S.; Kua, H. W.; Pang, S. D. Healing Cement Mortar by Immobilization of Bacteria in Biochar: An Integrated Approach of Self-Healing and Carbon Sequestration. *Cement and Concrete Composites* **2018**, *86*, 238–254. https://doi.org/10.1016/j.cemconcomp.2017.11.015.
(60) Neun, D.; Grothe, M.; Thompson, L. L. *A Report on the Feasibility of Deconstruction: An Investigation of Deconstruction Activity in Four Cities*; DIANE Publishing Company, 2001.
(61) A. P. Jackson; J. F. V. Vincent; R. M. Turner. The Mechanical Design of Nacre. *Proc. R. Soc. Lond* **1988**, *B 234, 415-440*.
(62) Barthelat, F.; Espinosa, H. D. An Experimental Investigation of Deformation and Fracture of Nacre–Mother of Pearl. *Experimental Mechanics* **2007**, *47* (3), 311–324. https://doi.org/10.1007/s11340-007-9040-1.
(63) Smith, B. L.; Schäffer, T. E.; Viani, M.; Thompson, J. B.; Frederick, N. A.; Kindt, J.; Belcher, A.; Stucky, G. D.; Morse, D. E.; Hansma, P. K. Molecular Mechanistic Origin of the Toughness of Natural Adhesives, Fibres and Composites. *Nature* **1999**, *399* (6738), 761. https://doi.org/10.1038/21607.
(64) Livanov, K.; Jelitto, H.; Bar-On, B.; Schulte, K.; Schneider, G. A.; Wagner, D. H. Tough Alumina/Polymer Layered Composites with High Ceramic Content. *J. Am. Ceram. Soc.* **2015**, *98* (4), 1285–1291. https://doi.org/10.1111/jace.13413.
(65) Espinosa, H. D.; Juster, A. L.; Latourte, F. J.; Loh, O. Y.; Gregoire, D.; Zavattieri, P. D. Tablet-Level Origin of Toughening in Abalone Shells and Translation to Synthetic Composite Materials. *Nat Commun* **2011**, *2* (1), 173. https://doi.org/10.1038/ncomms1172.
(66) Cordier, P.; Tournilhac, F.; Soulié-Ziakovic, C.; Leibler, L. Self-Healing and Thermoreversible Rubber from Supramolecular Assembly. *Nature* **2008**, *451* (7181), 977–980. https://doi.org/10.1038/nature06669.
(67) van Gemert, G. M. L.; Peeters, J. W.; Söntjens, S. H. M.; Janssen, H. M.; Bosman, A. W. Self-Healing Supramolecular Polymers In Action. *Macromol. Chem. Phys.* **2012**, *213* (2), 234–242. https://doi.org/10.1002/macp.201100559.
(68) Burnworth, M.; Tang, L.; Kumpfer, J. R.; Duncan, A. J.; Beyer, F. L.; Fiore, G. L.; Rowan, S. J.; Weder, C. Optically Healable Supramolecular Polymers. *Nature* **2011**, *472* (7343), 334–337. https://doi.org/10.1038/nature09963.
(69) Shen, X.; Belcher, A. M.; Hansma, P. K.; Stucky, G. D.; Morse, D. E. Molecular Cloning and Characterization of Lustrin A, a Matrix Protein from Shell and Pearl Nacre of *Haliotis Rufescens*. *J. Biol. Chem.* **1997**, *272* (51), 32472–32481. https://doi.org/10.1074/jbc.272.51.32472.
(70) Rief, M. Single Molecule Force Spectroscopy on Polysaccharides by Atomic Force Microscopy. *Science* **1997**, *275* (5304), 1295–1297. https://doi.org/10.1126/science.275.5304.1295.
(71) Rief, M. Reversible Unfolding of Individual Titin Immunoglobulin Domains by AFM. *Science* **1997**, *276* (5315), 1109–1112. https://doi.org/10.1126/science.276.5315.1109.
(72) Frauenfelder, H.; Sligar, S.; Wolynes, P. The Energy Landscapes and Motions of Proteins. *Science* **1991**, *254* (5038), 1598–1603. https://doi.org/10.1126/science.1749933.
(73) Cavelier, S.; Barrett, C. J.; Barthelat, F. The Mechanical Performance of a Biomimetic Nanointerface Made of Multilayered Polyelectrolytes. *Eur. J. Inorg. Chem.* **2012**, *2012* (32), 5380–5389. https://doi.org/10.1002/ejic.201200626.

(74) Kushner, A. M.; Gabuchian, V.; Johnson, E. G.; Guan, Z. Biomimetic Design of Reversibly Unfolding Cross-Linker to Enhance Mechanical Properties of 3D Network Polymers. *J. Am. Chem. Soc.* **2007**, *129* (46), 14110–14111. https://doi.org/10.1021/ja0742176.
(75) Vossen, B. G.; Schreurs, P. J. G.; van der Sluis, O.; Geers, M. G. D. Multi-Scale Modeling of Delamination through Fibrillation. *Journal of the Mechanics and Physics of Solids* **2014**, *66*, 117–132. https://doi.org/10.1016/j.jmps.2014.01.009.
(76) Kulkarni, M. G.; Matouš, K.; Geubelle, P. H. Coupled Multi-Scale Cohesive Modeling of Failure in Heterogeneous Adhesives. *Int. J. Numer. Meth. Engng.* **2010**, *84* (8), 916–946. https://doi.org/10.1002/nme.2923.
(77) Hang, F.; Lu, D.; Li, S. W.; Barber, A. H. Stress-Strain Behavior of Individual Electrospun Polymer Fibers Using Combination AFM and SEM. *MRS Online Proceedings Library Archive* **2009**, *1185*.
(78) Meyers, M. A.; Chen, P.-Y. *Biological Materials Science*, 1stEdition ed.; CAMBRIDGE UNIVERSITY PRESS, 2014.
(79) Meyers, M. A.; Chen, P.-Y.; Lopez, M. I.; Seki, Y.; Lin, A. Y. M. Biological Materials: A Materials Science Approach. *Journal of the Mechanical Behavior of Biomedical Materials* **2011**, *4* (5), 626–657. https://doi.org/10.1016/j.jmbbm.2010.08.005.
(80) Abaqus, V. 6.14 Documentation. *Dassault Systemes Simulia Corporation* **2014**, *651*, 6–2.
(81) Park, K.; Paulino, G. H.; Roesler, J. R. A Unified Potential-Based Cohesive Model of Mixed-Mode Fracture. *Journal of the Mechanics and Physics of Solids* **2009**, *57* (6), 891–908. https://doi.org/10.1016/j.jmps.2008.10.003.
(82) Park, K.; Paulino, G. H. Computational Implementation of the PPR Potential-Based Cohesive Model in ABAQUS: Educational Perspective. *Engineering Fracture Mechanics* **2012**, *93*, 239–262. https://doi.org/10.1016/j.engfracmech.2012.02.007.
(83) Spring, D. W.; Giraldo-Londoño, O.; Paulino, G. H. A Study on the Thermodynamic Consistency of the Park–Paulino–Roesler (PPR) Cohesive Fracture Model. *Mechanics Research Communications* **2016**, *78*, 100–109. https://doi.org/10.1016/j.mechrescom.2016.05.006.
(84) Pang, J. W. C.; Bond, I. P. A Hollow Fibre Reinforced Polymer Composite Encompassing Self-Healing and Enhanced Damage Visibility. *Composites Science and Technology* **2005**, *65* (11–12), 1791–1799. https://doi.org/10.1016/j.compscitech.2005.03.008.
(85) Yin, T.; Zhou, L.; Rong, M. Z.; Zhang, M. Q. Self-Healing Woven Glass Fabric/Epoxy Composites with the Healant Consisting of Micro-Encapsulated Epoxy and Latent Curing Agent. *Smart Mater. Struct.* **2008**, *17* (1), 015019. https://doi.org/10.1088/0964-1726/17/01/015019.
(86) Fenci, G. E.; Currie, N. G. Deployable Structures Classification: A Review. *International Journal of Space Structures* **2017**, *32* (2), 112–130. https://doi.org/10.1177/0266351117711290.
(87) Vaicekauskaite, J.; Mazurek, P.; Vudayagiri, S.; Skov, A. L. Mapping the Mechanical and Electrical Properties of Commercial Silicone Elastomer Formulations for Stretchable Transducers. *J. Mater. Chem. C* **2020**, *8* (4), 1273–1279. https://doi.org/10.1039/C9TC05072H.
(88) Kamal, M.; Safan, M. A.; Eltabey, M.; Zaki, E. S.; ABU, E. H. K. Compressive Strength of Portland Cement Pastes and Mortars Containing Cu-Zn Nano-Ferrite. **2012**.

(89) Lukin, R. Yu.; Kuchkaev, A. M.; Sukhov, A. V.; Bekmukhamedov, G. E.; Yakhvarov, D. G. Platinum-Catalyzed Hydrosilylation in Polymer Chemistry. *Polymers* **2020**, *12* (10), 2174. https://doi.org/10.3390/polym12102174.
(90) Ogden, R. W. Large Deformation Isotropic Elasticity–on the Correlation of Theory and Experiment for Incompressible Rubberlike Solids. *Proceedings of the Royal Society of London. A. Mathematical and Physical Sciences* **1972**, *326* (1567), 565–584.
(91) Pal, A.; Goswami, D.; Martinez, R. V. Elastic Energy Storage Enables Rapid and Programmable Actuation in Soft Machines. *Adv. Funct. Mater.* **2020**, *30* (1), 1906603. https://doi.org/10.1002/adfm.201906603.
(92) Shah, S. P.; Swartz, S. E.; Ouyang, C. *Fracture Mechanics of Concrete: Applications of Fracture Mechanics to Concrete, Rock and Other Quasi-Brittle Materials*; John Wiley & Sons, 1995.
(93) S, A., Anand; Teddy, B.; Yuji, I. *Guidelines for Earthquake Resistant Non-Engineered Construction*; UNESCO, 2014.
(94) Islam, M. M.; Aravinthan, T. Behaviour of Structural Fibre Composite Sandwich Panels under Point Load and Uniformly Distributed Load. *Composite Structures* **2010**, *93* (1), 206–215. https://doi.org/10.1016/j.compstruct.2010.05.019.
(95) Drougkas, A.; Roca, P.; Molins, C. Numerical Prediction of the Behavior, Strength and Elasticity of Masonry in Compression. *Engineering Structures* **2015**, *90*, 15–28. https://doi.org/10.1016/j.engstruct.2015.02.011.
(96) Bonderer, L. J.; Studart, A. R.; Gauckler, L. J. Bioinspired Design and Assembly of Platelet Reinforced Polymer Films. *Science* **2008**, *319* (5866), 1069. https://doi.org/10.1126/science.1148726.
(97) Wei, X.; Naraghi, M.; Espinosa, H. D. Optimal Length Scales Emerging from Shear Load Transfer in Natural Materials: Application to Carbon-Based Nanocomposite Design. *ACS Nano* **2012**, *6* (3), 2333–2344. https://doi.org/10.1021/nn204506d.
(98) Currey, J. D. Mechanical Properties of Mother of Pearl in Tension. *Proc R Soc Lond B Biol Sci* **1977**, *196* (1125), 443. https://doi.org/10.1098/rspb.1977.0050.
(99) Gao, H.; Ji, B.; Jäger, I. L.; Arzt, E.; Fratzl, P. Materials Become Insensitive to Flaws at Nanoscale: Lessons from Nature. *Proc Natl Acad Sci USA* **2003**, *100* (10), 5597. https://doi.org/10.1073/pnas.0631609100.
(100) Gao, H. Application of Fracture Mechanics Concepts to Hierarchical Biomechanics of Bone and Bone-like Materials. In *Advances in Fracture Research*; Carpinteri, A., Mai, Y.-W., Ritchie, R. O., Eds.; Springer Netherlands, 2006; pp 101–137.
(101) Barthelat, F.; Dastjerdi, A. K.; Rabiei, R. An Improved Failure Criterion for Biological and Engineered Staggered Composites. *J R Soc Interface* **2013**, *10* (79). https://doi.org/10.1098/rsif.2012.0849.
(102) Du, G.; Mao, A.; Yu, J.; Hou, J.; Zhao, N.; Han, J.; Zhao, Q.; Gao, W.; Xie, T.; Bai, H. Nacre-Mimetic Composite with Intrinsic Self-Healing and Shape-Programming Capability. *Nat Commun* **2019**, *10* (1), 800. https://doi.org/10.1038/s41467-019-08643-x.
(103) D'Elia, E.; Eslava, S.; Miranda, M.; Georgiou, T. K.; Saiz, E. Autonomous Self-Healing Structural Composites with Bio-Inspired Design. *Sci Rep* **2016**, *6* (1), 25059. https://doi.org/10.1038/srep25059.
(104) Molecular mechanistic origin of the toughness of natural adhesives, fibres and composites - ProQuest https://search.proquest.com/docview/204479383?pq-origsite=gscholar.

(105) Fantner, G. E.; Oroudjev, E.; Schitter, G.; Golde, L. S.; Thurner, P.; Finch, M. M.; Turner, P.; Gutsmann, T.; Morse, D. E.; Hansma, H.; Hansma, P. K. Sacrificial Bonds and Hidden Length: Unraveling Molecular Mesostructures in Tough Materials. *Biophysical Journal* **2006**, *90* (4), 1411–1418. https://doi.org/10.1529/biophysj.105.069344.
(106) Akoun, G.; Yonnet, J.-P. 3D Analytical Calculation of the Forces Exerted between Two Cuboidal Magnets. *IEEE Transactions on magnetics* **1984**, *20* (5), 1962–1964.

PUBLICATIONS

Restrepo, V., Hosseini, M., Gallant, C., Weymouth, B., and Zavattieri, P. (**2021**). “A Two-Scale Strategy for the Modeling of Hook and Loop Fasteners.” Journal of the Mechanics and Physics of Solids – Under Review.

Restrepo, V. and Martinez, R. V. (**2021**). “Bioinspired fabrication of reconfigurable elastomeric cementitious structures using self-healing mechanical adhesives interfaces.” Materials & Design. https://doi.org/10.1016/j.matdes.2021.109691

Pal, A., **Restrepo, V.**, Goswami, D., and Martinez, R. V. (**2021**)."Exploiting Mechanical Instabilities in Soft Robotics: Control, Sensing, and Actuation." Advanced Materials. https://doi.org/10.1002/adma.202006939

Restrepo, V., Villarraga, J., and Pavón Palacio, J. (**2014**)."Stress Reduction in the Residual Limb of a Transfemoral Amputee Varying the Coefficient of Friction." Journal of Prosthetics and Orthotics. https://doi.org/10.1097/JPO.0000000000000044

Restrepo, V., Villarraga, J., and Pavón Palacio, J. (**2014**)."Determining the Most Representative Topographic Variables in Locally Manufactured Sockets for Patients with Transfemoral Amputation." Ingeniería y Competitividad. vol. 16, num. 1, 2014, pp. 221-228 https://www.redalyc.org/articulo.oa?id=291331195018